MAGNETIC RESONANCE ELASTOGRAPHY

MAGNETIC RESONANCE ELASTOGRAPHY

By Farukh Saeed, B. Eng.

A Thesis

Submitted to the school of Graduate Studies

in Partial Fulfillment of the Requirements

for the Degree

Master of Applied Science

McMaster University Master of Applied Science (2011) Hamilton, Ontario

TITLE: Magnetic Resonance Elastography **AUTHOR:** Farukh Saeed, B.Eng.

SUPERVISOR: Professor Gerald R. Moran. **NUMBER OF PAGES:** xix, 152.

Abstract

This thesis is composed of six chapters. First MRE is briefly introduced together with some relevant literature in Chapter one. The second chapter is about the principles and theory of magnetic resonance imaging, with the MRE theory, software and hardware addressed in Chapter 3. Chapters 4 and 5 describe the hardware design, software programming, experimental setup and elasticity reconstruction. Chapter 6 is a general discussion, introducing challenges and future directions.

A vibration actuator and coil was designed and constructed, then combined with the necessary hardware required to induce the motion in the actuator. A Gradient Echo pulse sequence was modified using the Siemens IDEA environment for MRE application. A phantom was made with concentrations of 1%, 2%, and 3% agar gel.

The phantom was scanned using the MRE sequence while inducing the propagating waves. Waves were selected to have frequencies of 125 Hz and 250 Hz. Magnitude and phase images acquired at these frequencies were used to construct the elasticity map using the MRE/Wave reconstruction software. Mean Shear Modulus measured in 1% gel cylinder is 10 kPa and standard deviation (SD) is 6 kPa. Mean elasticity value measured in 3% gel is 49 kPa and SD is 9 kPa. Mean value measured in the background which is 2% gel is 28 kPa and SD

is 6 kPa. The results obtained are comparable to the values calculated in literature.

Acknowledgement

I would like to thank first my supervisor, Dr. Gerald Moran for providing countless hours of support and guidance. He has been an invaluable mentor. I thank him for supervising me as a part time student. I continued my studies after a gap of 12 years and he helped me in catching up with all the new techniques and study resources.

Also I want to express my gratitude to Ron Burgess at London Health Sciences for his support in acquiring data, Tim Devito from Siemens MRI division for his support with the sequence programming and Kenrick at McMaster University for his help in hardware. I would like to thank my lab fellows: Kyle, Dost, Ian and Cassie.

I also appreciate the help and support of Mike Capuano Manager Biomedical Technology Hamilton Health Sciences where I am employed as Biomedical Technologist. I am thankful to the Graduate School of Biomedical Engineering for initiating this program and providing me the opportunity to become a graduate student. I acknowledge the administrative support of David Ryan and Laura Kobayashi from School of Biomedical Engineering.

Finally, I would like to extend very special thanks to my parents and wife for their continuous help and encouragement – to this point and beyond.

Table of Contents

Lists of Figures and Tables

List of all Abbreviations and Symbols

USE	=	Ultrasound Elastography.
MRE	=	Magnetic Resonance Elastography.
MRI	=	Magnetic Resonance Imaging.
RF	=	Radio Frequency.
RO	=	Read out.
PE	=	Phase Encode.
SS	=	Slice Select.
FOV	=	Field of View.
FID	=	Free induction decay.
GE	=	Gradient Echo.
SE	=	Spin Echo.
EPI	=	Echo Planar Imaging.
MEG	=	Motion Encoding Gradient.
FE	=	Flow Encoding.
LFE	=	Local frequency estimation.
AIDE	=	Algebric Inversion of differential Equation.
fMRI	=	Functional Magnetic resonance Imaging.
TTL	=	Transistor transistor logic.
IDEA	=	Integrated Development Environment for Applications.
POET	=	Protocol Offline Editing Tool.

Chapter 1

Introduction

1.1 Introduction and Motivation

Manual palpation is the centuries-old technique to measure breast tissue elasticity. Changes in tissue stiffness often relate to disease or the symptoms of disease such as cancer [1]. Even today palpation is the first tool used by the physician to detect symptoms of disease [2]. Similarly, self examination of the breast using palpation to detect cancer is highly recommended [3]. Palpation has its limitation however, as small and inaccessible lesions cannot be detected and there is no way to quantify the mechanical properties [4].

Mechanical testing of the human tissues has drawbacks and in most of cases, is not practical [5]. These methods include testing the specimens under physical load conditions. Usually these tests require cutting the specimens from larger tissues and from certain locations. Mechanical tests are destructive to tissues and they only give information about that small portion not the whole organ [6]. Different imaging modalities (Ultrasound, Computed Tomography, and Magnetic Resonance Imaging) are available to detect tissue characteristics but diagnostic imaging does not provide any information about the tissue elastic properties. Elastic modulus of various human tissues varies over four orders of magnitude and MRE measures Physical properties differently than the other modalities (Ultrasound, CT and MRI). Figure 1.1 shows the physical parameters measured by different imaging modalities. If we compare ultrasound with elastography, bulk modulus for soft tissues in ultrasound lies in smaller range compare to shear modulus in elastography which covers variety of soft tissues ([7] chapters 1.1).

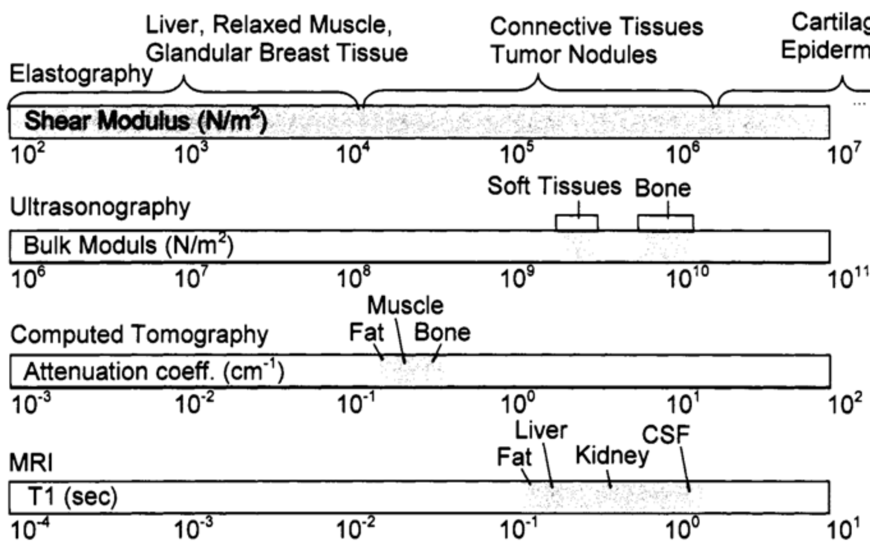

Figure 1.1: Dynamic range of shear modulus and properties measured by different imaging modalities. Source: ([7] Chapters 1.1).

The clinical importance of measuring the mechanical properties of tissues has been widely recognized [8-25] and various investigators have proposed methods like UltraSound Elastography (USE) and Magnetic Resonance Elastography (MRE) to approach the measurement [26-38].

Usually stress is applied to tissues and the resulting strain is observed or measured with the help of imaging modalities [39]. MRE is a technique that can directly visualize the propagating strain waves in tissues with the help of MRI [38]. A mechanical actuator is used to generate the waves of a known frequency.

The resulting image contains information about the particles displacement - typically of the order of microns. From this displacement information, the elastic properties of tissues can be determined [40].

Thus far the most common application of MRE is the detection and characterization of tumors [15, 16]. MRE is an emerging quantitative tool for measuring the viscoelastic properties of tissue in vivo and current research is ongoing to expand this technique into the clinical arena [8-25]. This activity has lead to the interest in exploring MR Elastography at this physical site, and to develop the software and hardware required to implement it.

1.2 Literature Review

Extensive research in the elastography field over the past twenty years has shown applications in tissue mimicking phantoms as well as biological tissues [41, 42]. Activity in the field utilizes a variety of techniques to validate the methods clinically [43]. Elastography in general can be divided into UltraSound Elastography (USE) and MR Elastography (MRE), each of which uses different methods of applying the stress [44].

Historically, Elastography began in the field of Ultrasound [45]. A Pulsed Doppler based system was developed to measure the mechanical properties of soft tissues [26]. This technique is further developed by Gao [27] and Skovoroda [28]. In USE, a shear wave is generated by the radiation force produced by an amplitude modulated beam of focused ultrasound. These waves are detected with Ultrasound and acquired data are used to calculate the elastic properties of tissues. A detailed assessment of the progress and challenges in the USE field has been discussed in a paper presented by Parker [29].

MR Elastography (MRE) is based on the phase contrast method developed for imaging blood flow and diffusion in MRI [30-32]. In the phase contrast method, changes in the phase of spins is measured after the application of flow encoding gradients and this change of phase represents the physical motion of the spins. This method will be described in more detail in chapter 3. The first MRE method was presented by Lewa [33, 34] where the MR phase changes were used to measure the viscoelastic properties. This method was later further developed by Muthapillai [35], Fowlkes [36] and Plewes [37].

The technique presented by Muthapillai [38] is a fully dynamic phase contrast method in which a cyclic motion is generated in the object that is synchronous with the gradients applied by the MR Scanner. Resultant MR images carry information regarding particle displacements due to this motion. By analyzing the phase differences between the oscillatory motion and the imaging gradients, it is possible to capture the transmission of shear waves in an object [38]. This too will be discussed in more detail in chapter 3.

Other methods involve static loading where the object is scanned before and after loading states. Loading is a static compression applied to the object. Data acquired during these two states is used to measure the mechanical properties of tissues. Dutt and his group [44] compared ultrasound and MR Elastography and showed that the resolution achieved in MR is higher compared to ultrasound.

Data collected by MRE is typically in the form of displacement data. Various approaches have been taken to convert this complex data into the elastic data representing the mechanical properties. Knutsson presented the local frequency estimation technique [46], implemented by Manduca [40] which combines local estimates of instantaneous frequency. A direct Inversion technique was developed by Oliphant [47, 48] which uses an algebraic inversion of differential equations of motion. Van Houten [49, 50] presented the Overlapping subzone technique which can be applied to 2D and 3D data. In this approach, the whole region is divided into small zones. First inversion is applied to small zones and then these zones are combined to obtain the whole solution. All above techniques will be discussed in detail in section 3.5. Various data post-processing techniques (Chapter 2.4.2 [7]) and filters [51, 52] are used to improve the data quality and further discussion will be available in section 3.5.2 and 3.53.

MRE has been successfully applied clinically in many areas: Abdomen [8-11], Brain [12-14], Breast [15-17], Cardiac [18], Hyaline Cartilage [19], Lungs [20], Muscles [21, 22], Prostate [23], Thyroid Glands [24] and heel fat pads [25]. Extensive work has been done and is still active in the field of imaging breast cancer [17].

At present two groups are dominating the field in MRE research. The first group is located at the Mayo Clinic and is headed by Dr R Ehman [53]. This group's primary focus is the clinical application of MRE in Liver [9]. They have also developed reconstruction software called MRE/Wave [51] based on the local frequency estimation technique. This thesis will use this software to reconstruct the elasticity maps. It is very user friendly and has the option of displaying the data during different stages. The second group is located in Germany and is headed by Dr I Sack [54]. Their main focus is reconstruction software, actuator construction and cardiac MRE applications [18].

There is a more specific literature list that was extremely useful for this project. The basic MRE concept and experimental setup is based on the paper by Muthupillai [35], which is very informative in terms of the vibration actuator and motion encoding gradients. Oida's [55] paper gives very useful information about elasticity; and the vibration actuator design is based on the concept presented in this paper. Trapezoidal motion encoding gradients in the MRE sequence were based on the information presented by Dunn [56], where it was concluded that trapezoidal MEG's are more efficient compared to sinusoidal MEG's. The reconstruction software MRE/Wave [51] was used in this analysis, and is based on frequency estimation techniques presented by Knutsson [46] and used by Manduca [40]. These two papers explain the theory behind the local frequency estimation technique.

1.3 Thesis Structure/Contributions

In the current chapter, elastography and MRE has been briefly introduced. A literature review is included which gives some information about the history of MRE and contributions made by different researchers in this field. An outline of the thesis and a brief description about each chapter is included.

Chapter 2 provides some background on magnetic resonance imaging and is divided into four parts. The first part gives information about the basic spin and MR phenomenon. The second part describes some approaches to obtain image contrast. The third part discusses the principles of MRI and gives information about different hardware components required. The final section of chapter 2 outlines the main pulse sequences used in MRI scanning.

In chapter 3 MR elastography is discussed in detail and is divided into six sections: 1) General elasticity theory; 2)MRE and the major components required; 3) Types of actuators required for MRE; 4)Required Pulse sequence modification for MRE; 5) Image Reconstruction; and 6) Clinical applications of MRE.

In chapter 4 materials and methods for this work are discussed. A brief description of the MRI system will be provided. Then the design of actuator and the pulse sequence programming and modifications required for MRE will be outlined. Finally the phantom and the overall experimental setup will be discussed

Chapter 5 describes the data acquisition and how to reconstruct elasticity maps. Details will be provided regarding: the parameters selected in the MRE Pulse sequence; the Image data and raw data acquired; and the free online software MRE/Wave used for reconstruction. Concluding this chapter will be a discussion of the elasticity values measured.

Chapter 6 is a general discussion, conclusion, and future directions section. The major contribution of this project is the development of an actuator and a modification of the Gradient Echo sequence used for MRE.

Chapter 2

Magnetic Resonance Imaging

2.1 Magnetic Resonance Imaging

Magnetic Resonance Imaging (MRI) is a technique in which images are produced using the properties of nuclear spin, and the associated magnetic moment of atomic nuclei, principally hydrogen in clinical applications. Images are obtained tomographically and can reveal internal physical and chemical properties of an object through measurement of returned radiofrequency (RF) signals. In addition, tomographic images can be generated along any direction without changing the orientation of the patient or mechanically adjusting the machine.

2.1.1 Spin and MR Phenomenon

The simplified Bohr model of the hydrogen atom has a nucleus consisting of a single proton with the electrons circling around it as shown in figure 2.1 ([57] Chapter 1).

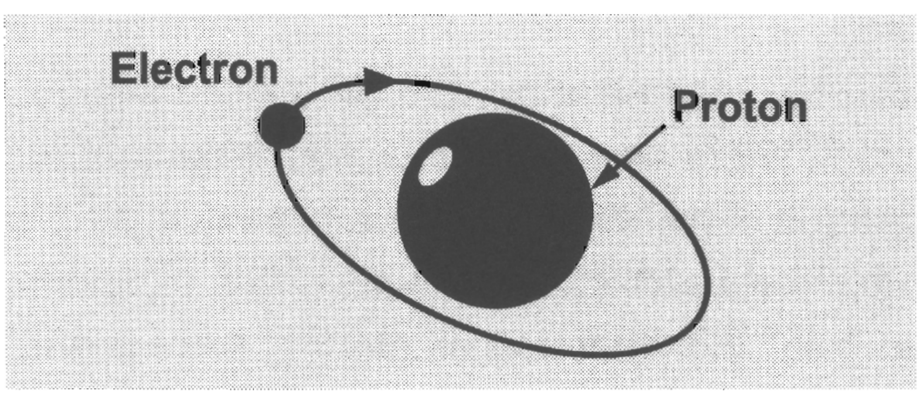

Figure 2.1: Electron circle around atomic shell. Source: [57].

The proton carries a positive charge and electron carries negative charge, thus the entire atom is electrically neutral. NMR is sensitive to the nuclear spin (**I**=1/2) of the proton. Due to the spin, the proton also has an angular momentum S = ħ**I** as shown in figure 2.2a, where ħ is Planck's constant. The proton also has a magnetic dipole moment μ, thus often semi classically it is described as behaving as a tiny magnet as shown in figure 2.2b.

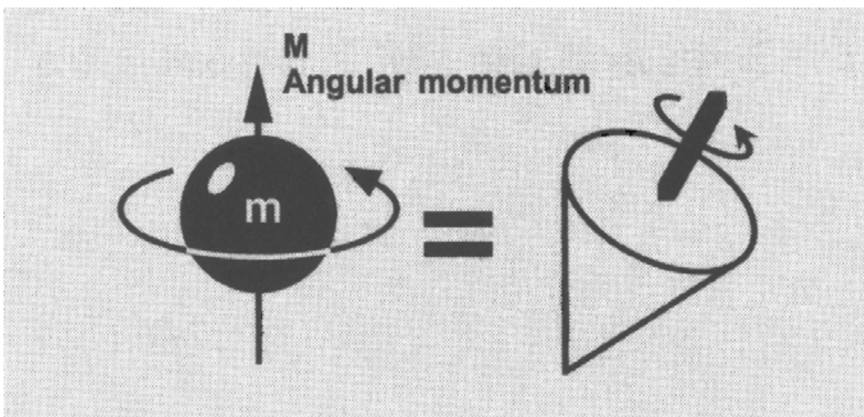

Figure 2.2a: Angular momentum of proton. Source: [57].

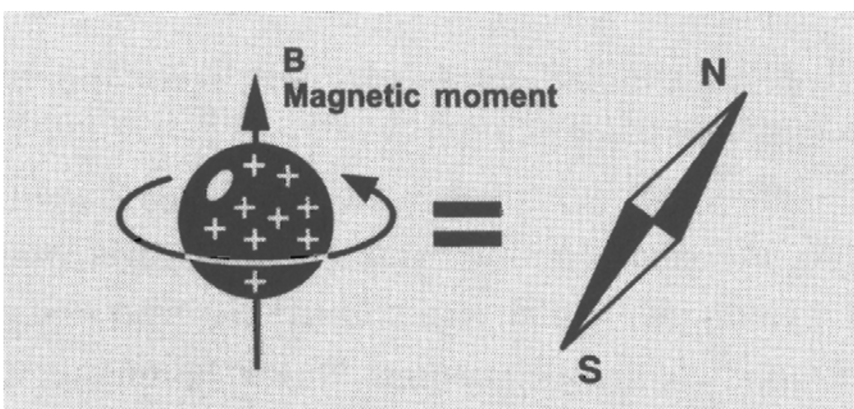

Figure 2.2b: Magnetic dipole moment equal to tiny magnet. Source: [57].

The magnetic moment is proportional to the nuclear spin, with the gyromagnetic ratio, γ, being the constant of proportionality. Thus μ = γS = γħI. When an external magnetic field B_0 is applied, the spins will align preferentially along the external magnetic field direction due to the torque μ x B_0. Spins experiencing this torque will react with a precessional motion as shown in figure 2.3.

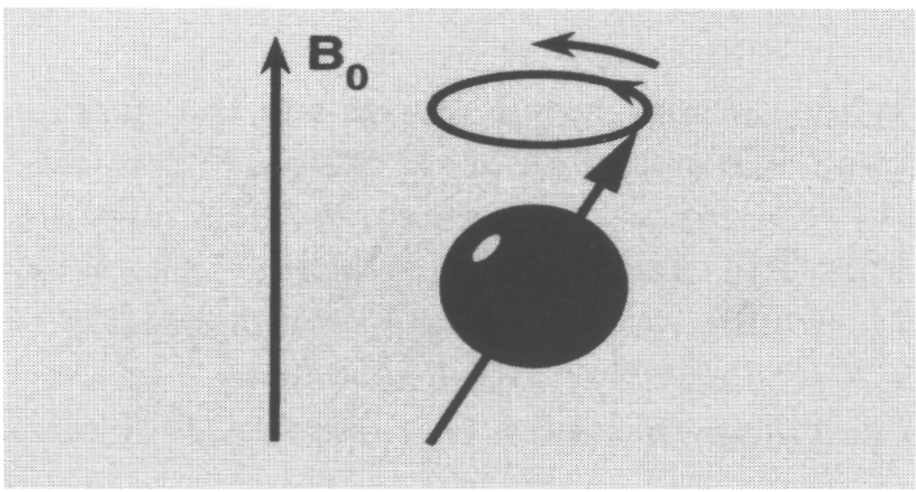

Figure 2.3: Precessional motion under external magnetic field Bo. Source: [57].

This precession has a characteristic frequency called the Larmor frequency which is proportional to the strength of the magnetic field. The Larmor frequency is a crucial concept to the MRI phenomenon. It is exactly proportional to the strength of the magnetic field B_0 and can be calculated using the Larmor equation:

$$\omega_0 = \gamma . B_0$$ Equation No: 2.1

Where,

ω_0 is Larmor frequency in megahertz [MHz]

γ is the gyromagnetic ratio; a constant. For protons it is 42.575 [MHz/T]

B_0 is the magnetic field strength [T]

The Larmor frequency for the protons is 63.9 MHz at 1.5T. Because of the large number of spins (of the order of Avagadro's number) in a sample, there is a net magnetization that develops in the z direction as depicted in figure 2.4. At any instant in time, the transverse component of this magnetization tends to cancel, however there is a net vector sum, Mz, of magnetic moments along z.

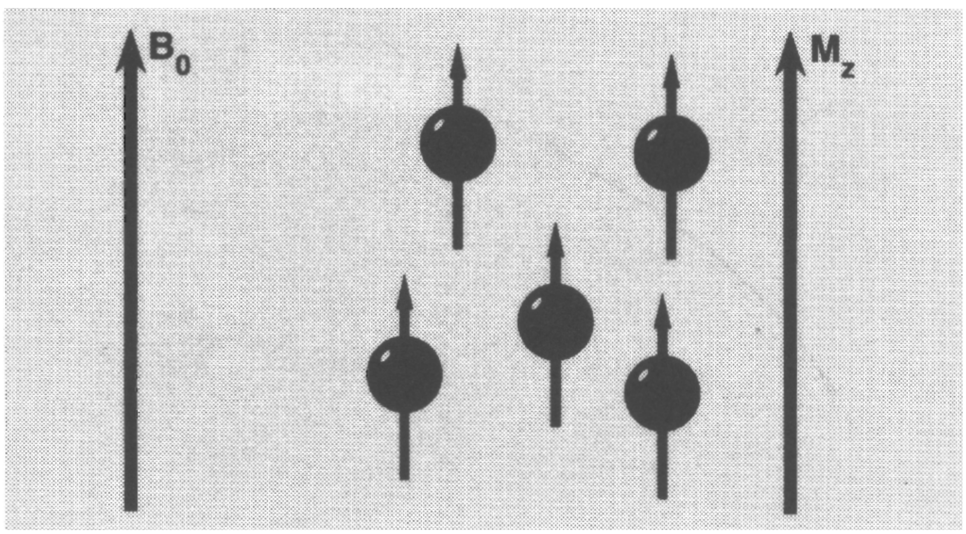

Figure 2.4: Addition of magnetic vectors of individual spins. Source: [57].

At this stage it is possible to transfer energy to the spins using an electromagnetic (RF) pulse with the same frequency as the Larmor frequency.

This energy causes the net magnetization vector to deflect away from the Z-direction. This situation is called the excited state for the spins (figure 2.5).

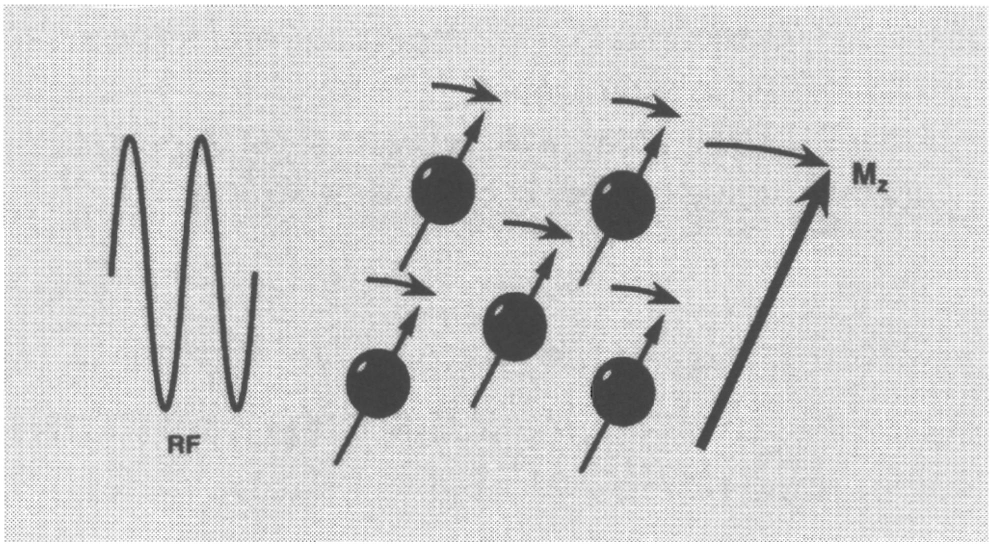

Figure 2.5: Excited state of spins after the application of RF pulse. Source: [57].

By applying an RF Pulse with right power and duration we can flip these spins and the entire magnetization Mz into the XY Plane resulting in transverse magnetization, Mxy. The transverse component of the magnetization then precesses in the XY plane because of the torque exerted by the main magnetic field. It is this precession of the magnetization that generates an induced voltage in the receive coil, that is the NMR / MRI signal as shown in figure 2.6. This signal will be weighted according to various factors such as the state of the tissue, the relaxation times of the tissues, and a variety of non-endogenous means of generating contrast.

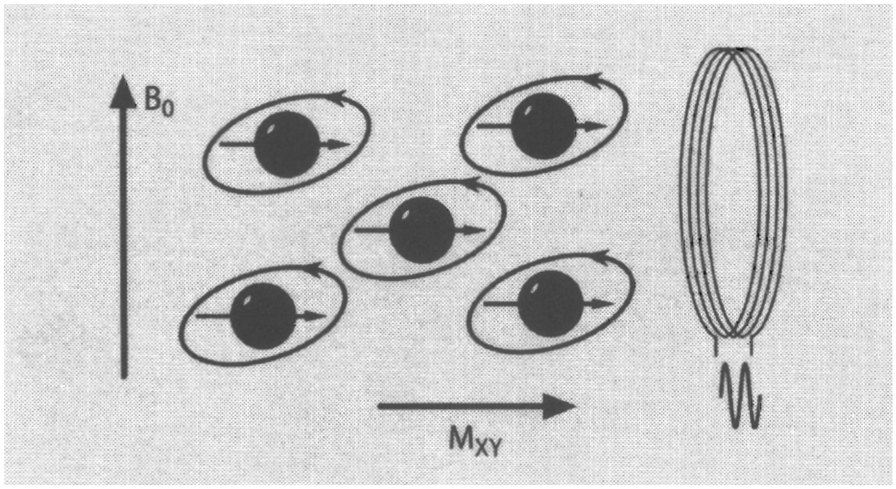

Figure 2.6: Generation of MR signal in receiver coil. Source: [57].

2.2 Image Contrast:

Contrast in an MRI image is observed primarily through the exploitation of the characteristic relaxation times of spins after the application of the initial RF pulse. Once excited by an RF pulse, spins return to their equilibrium state through a number of mechanisms. The proton relaxation properties are different in different tissues and that is what causes the intrinsic contrast between tissues and results in the clinical practicality of MRI.

2.2.1 Relaxation

When dealing with protons, there are two relaxation processes that occur on different timescales, T1 and T2. These two relaxation processes reduce the magnitude of the transverse magnetization (T2) and cause the spins to return to the equilibrium state (T1) ([57] Chapter 2).

T1 Relaxation:

Because of the action of T1 relaxation, the excited spins will return to the Z-direction along the main magnetic field as shown in figure 2.7.

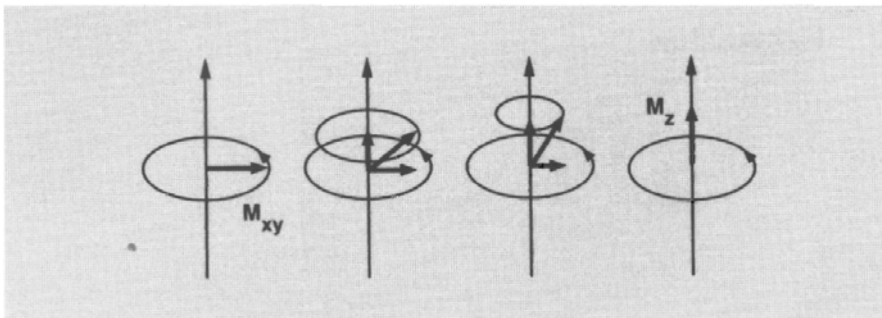

Figure 2.7: Return of excited spins in z-direction by releasing energy into surroundings.

Source: [57].

When 90 degree pulse is applied to sample M_0 , T1 is the time required for Mz to return to 63% of its equilibrium value (before the application of the RF Pulse), also called spin-lattice relaxation time or longitudinal relaxation time. During the T1 time protons exchange energy with lattice and there is an exponential re-growth of magnetization which can be written in terms of time as ([58] chapter 3.1):

$$M(\tau)=M_0(1-e^{(-\tau/T1)})$$ Equation No: 2.2

Where τ , is the time following the application of RF Pulse and M_0 is the value of magnetization before the application of RF Pulse. Figure 2.8 shows the T1 relaxation Curve at different multiples of T1.

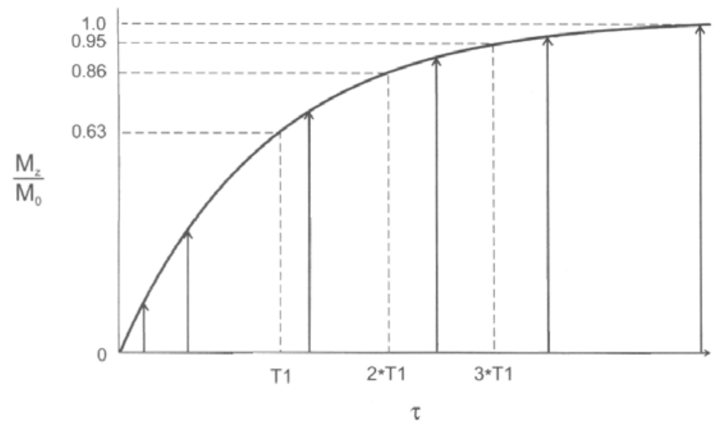

Figure 2.8: T1 relaxation curve. Source: [58].

T2 Relaxation:

T2 or Transverse relaxation is the loss of transverse magnetization which is due to the loss of phase coherence of spins as shown in figure 2.9. Since T2≤T1, T2 relaxation typically occurs on a faster timescale. In this case there is no emission of energy to the surroundings (the "lattice"), but rather there is an exchange of energy between spins.

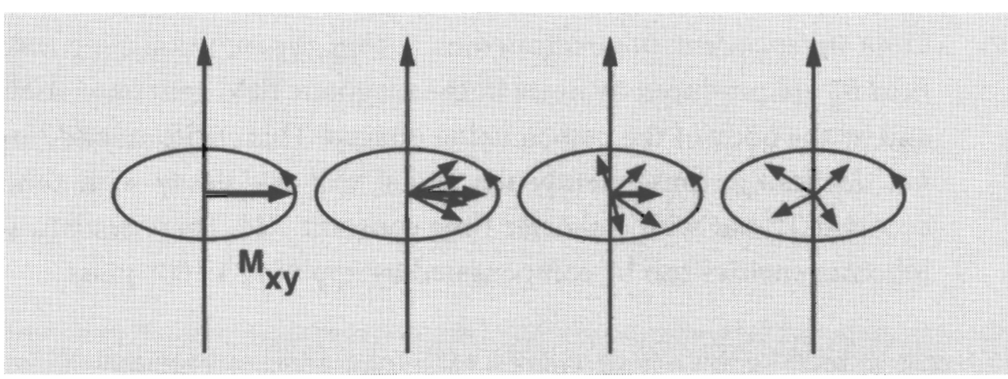

Figure 2.9: T2 relaxation. Source: [57].

T2 is the time required for the transverse component of M to decay to 37% of its initial value also called spin-spin relaxation time or transverse relaxation time as shown in figure 2.10 ([58] chapter 3.2).

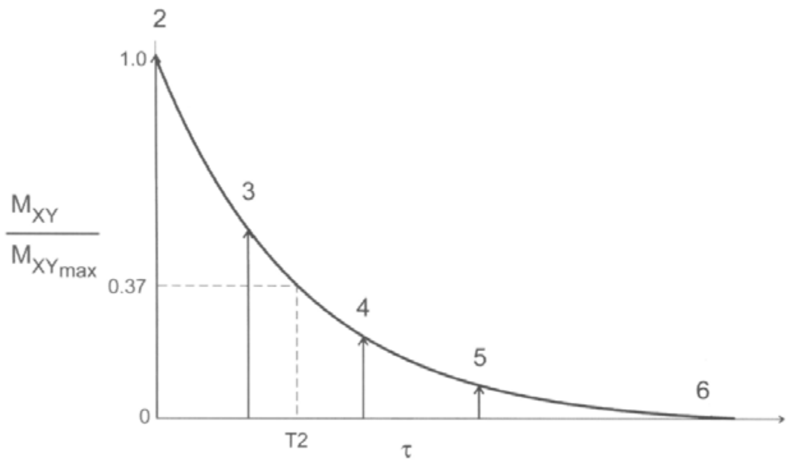

Figure 2.10: T2 relaxation curve. Source: [58].

The decay of the transverse magnetization component can be written as:

$$M_{xy}(t) = M_{xy_{\max}} e^{(-t/T2)}$$ Equation No: 2.3

Where $M_{xy_{\max}}$ is the transverse magnetization following the excitation pulse, and may or may not be equal to the equilibrium magnetization. Nonlinearities in the main magnetic field and patient body, as well as magnetic field gradients used in MRI, create a further decay in signal with a shorter time constant T2*.

2.2.2 Types of Image contrast:

There are three parameters that determine the brightness and contrast of most MRI Images. In T1 weighted imaging, contrast is mainly determined by the T1 relaxation time of tissues whereas in T2 weighted imaging, contrast is determined by the T2 time of tissues. Proton density weighted images show the number of excitable spins per unit volume and can be achieved by reducing the influence of T1 and T2.

In order to acquire an MR Image, a tissue slice needs to be excited and the resulting signal measured repeatedly. The repetition time (TR) is the time between the two successive excitations of same slice. The echo time (TE) is the time between the excitation and the measurement of the MR signal. By controlling the value of these parameters different contrasts can be achieved ([57] Chapter 3).

T1 weighted imaging can be accomplished by keeping the value of TR short (TR A = 500ms) as shown in figure 2.11. At longer TR (TR B = 2000ms) less T1 weighting is observed. Tissues with short T1 appear bright and with long T1 appear dark in the T1 weighted image.

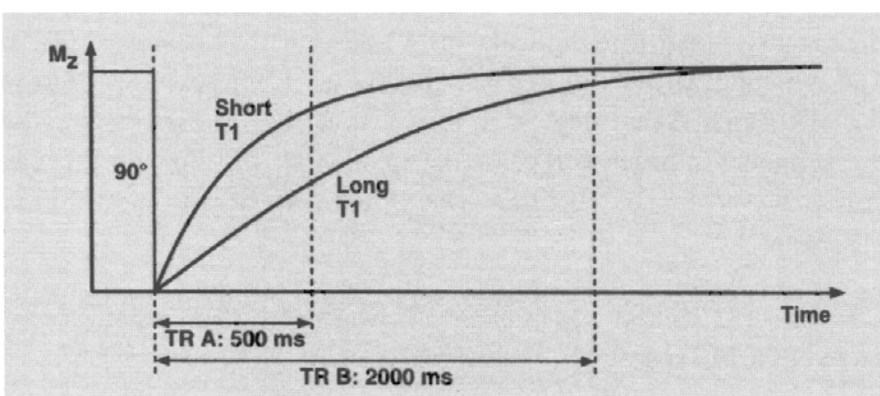

Figure 2.11: TR and T1 Contrast. Source: [57].

T2 weighting is accomplished by keeping the value of TE long (TE B = 80ms) as shown in figure 2.12. However by choosing a short TE (TE A = 20ms) there is less differential contrast between tissues with different T2s. Tissues with short T2 appear dark and tissues with long T2 appear bright in a T2 weighted image.

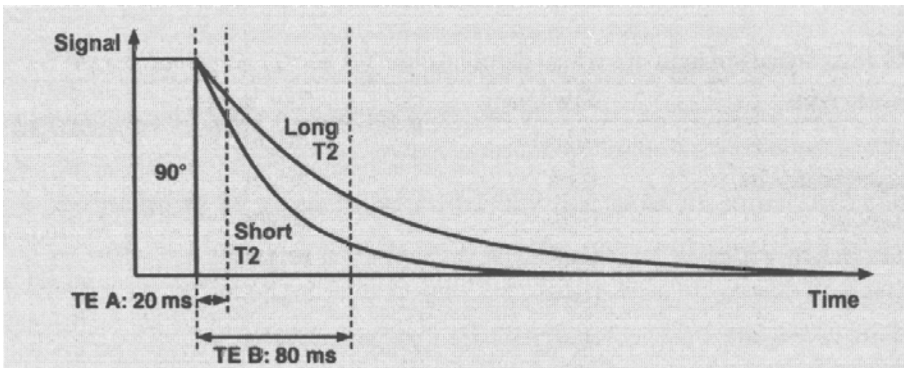

Figure 2.12: TE and T2 Contrast. Source: [57].

2.3 Principles of Magnetic Resonance Imaging:

In MRI, gradients are used to make the magnetic field spatially dependent. Three physical gradients are used in the x, y and z directions, Gx, Gy, and Gz. The gradient is usually a linear change in the magnetic field along z, with respect to one of the Cartesian coordinates, IE) Gx = dB(z)/dx, Gy = dB(z)/dy, etc. Their timing, duration and magnitude are controlled through the software depending on the acquisition parameters. Combinations of gradients, RF pulses, data sampling and the timing between each are used to acquire MRI images. The program which defines these factors is called a pulse sequence. In the presence of gradients equation 2.1 can be written as:

$$\omega_i = \gamma(B_0 + G \cdot r_i) \qquad \text{Equation No: 2.4}$$

Where ω_i is the frequency of a proton at position r_i and *G* is the gradient field amplitude and direction. The MRI Image consists of pixels representing the volume elements of tissues (or voxels). The pixel intensity is proportional to the number of protons in the voxel weighted by the tissue's T2 decay and T1 recovery ([58] chapter 4) as illustrated in figures 2.11 and 2.12.

2.3.1 Slice Selection:

In MRI it is most common to separate the 3D Volume into 2D slices. The gradient direction on the three axis x, y and z determines the slice orientation and the gradient amplitude together with the RF pulse characteristics determine slice thickness and position. The RF pulse can be made slice selective by controlling the centre frequency and bandwidth of frequencies present. The duration and shape of the pulse determine its frequency content. RF pulse excitation will be explained in more detail in section 2.3.5. The centre frequency of the RF pulse determines the location of excitation in the presence of slice selection gradient. Slice thickness is set by the gradient amplitude G_{SS} and the frequency bandwidth of the RF Pulse:

$$\Delta\omega = \gamma\Delta(G_{ss} * Thickness) \qquad \text{Equation No: 2.5}$$

Keeping $\Delta\omega$ same, the slice thickness can be changed by changing the amplitude of G_{SS}. Figure 2.13 shows that thinner slices require large G_{SS} as compared to larger slices for a given pulse bandwidth ([58] chapter 4.1).

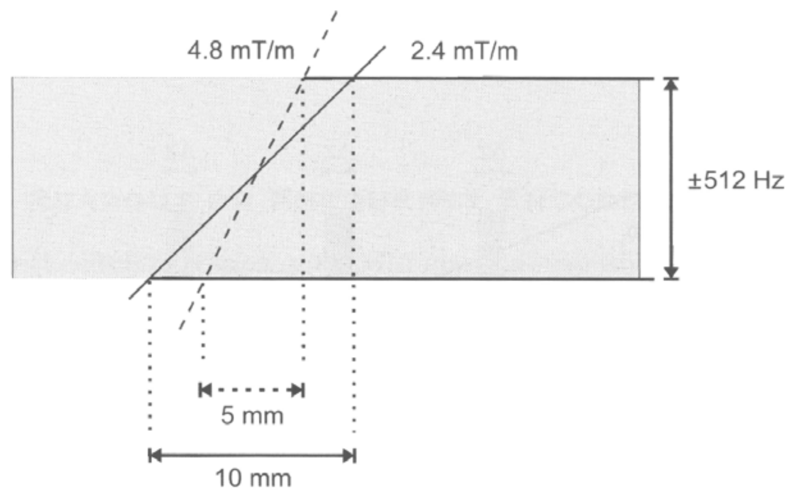

Figure 2.13: Slice thickness is determined by slice select gradient amplitude. Source: [58].

Once G_{SS} is determined, the centre frequency may be calculated using equation no 2.4 to resonate the desired location. Multi slice imaging uses the same G_{SS} but unique RF pulses for each slice. Each RF pulse has the same bandwidth but different central frequencies exciting the different slices as shown in figure 2.14.

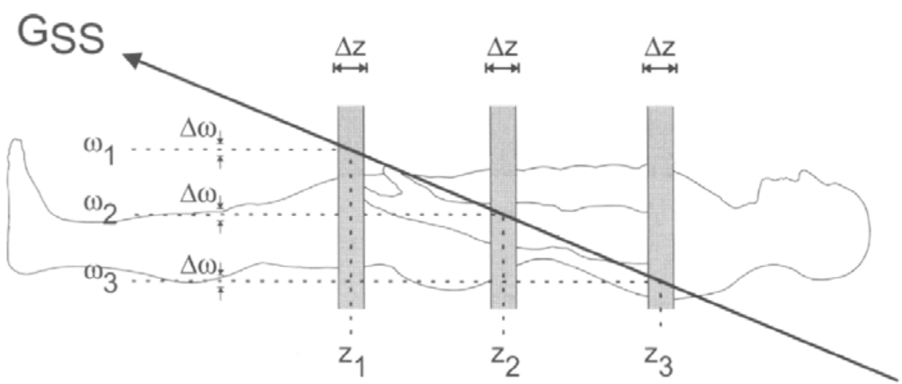

Figure 2.14: Different centre frequencies exciting different slices. Source: [58].

2.3.2 Frequency Encoding:

In MR Imaging the signal detection typically is done through a process called frequency encoding. In order to detect the MR signal a readout gradient G_{RO} is applied perpendicular to the slice direction. With the application of the readout gradient, protons begin to precess at different frequencies depending upon their position according to equation 2.4 – hence the name frequency encoding. The echo signal received by the coil caries the information about the frequency of precession. The magnitude of G_{RO} and the frequency gives information about the positions of the proton as illustrated in figure 2.15 and can be mapped onto its corresponding position in the image. It will be explained in further detail in section 2.3.6. ([58] Chapter 4.2).

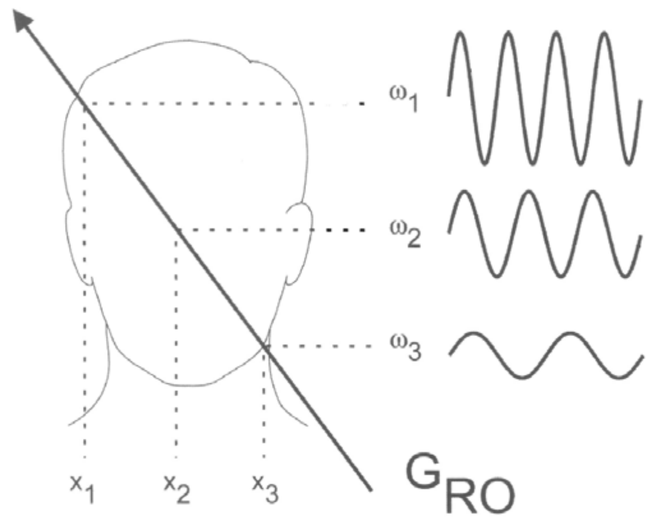

Figure 2.15: With the application of G_{RO} frequency of each proton changes according to its position. Source: [58].

The Magnitude of the read out gradient is determined by the Field Of View (FOV) in the read out direction and the Nyquist frequency. The Nyquist frequency ω_{NQ} is the maximum frequency that can be sampled correctly in the analog-to-digital conversion process. These frequencies are therefore bounded above and below the central frequency by the Nyquist frequency. Hence protons at both ends of readout direction are precessing at a maximum - the Nyquist frequency. Using frequencies above and below the nyquist limit can create artifacts in the image. Using equation 2.4 readout frequencies in the image are given by:

$$\Delta\omega_{RO} = 2 * \omega_{NQ} = \gamma\Delta(G_{RO} * FOV_{RO}) \qquad \text{Equation No: 2.6}$$

From equation 2.6, decreasing the magnitude of read out gradient G_{RO} increases the read out field of view at constant Nyquist frequency and is shown in figure 2.16.

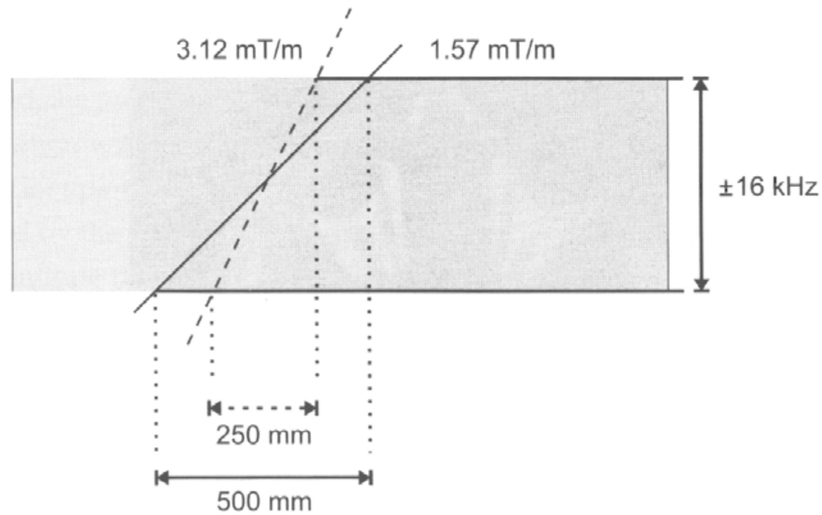

Figure 2.16: Readout gradient magnitude changes field of view in readout direction. Source [58].

The spatial resolution in the readout direction δ_{RO} is expressed in mm/pixel and is equal to the FOV_{RO} divided by the number of sample points in the read out direction N_{RO}. This process however only determines one direction within the 2D slice.

2.3.3 Phase Encoding:

The third direction is encoded with a process called phase encoding, however it should be noted that both frequency and phase encoding are closely related, and both are types of phase encoding. The phase encoding gradient G_{PE} is perpendicular to G_{SS} and G_{RO} and is applied repeatedly at different strengths to locate the sources of MR signals along the phase encoding-encoding axis.

When the phase encode gradient G_{PE} is applied, the precessional frequency will increase or decrease following equation 2.4. When G_{PE} is turned off, the protons return to precessing at the Larmor frequency, however the proton phase is shifted compared to its previous state. This phase shift depends upon the location of the protons and the magnitude and duration of G_{PE}. Protons located at the edge of the *FOV* experience a maximum phase shift as shown in figure 2.17. Protons at location y_2 experience no change in frequency during the application of G_{PE} so when it is removed, there is no change in phase. However protons at y_3 precess faster during the phase encode period so these protons are advanced in phase when G_{PE} is switched off, and protons at location y_1 lag in phase when G_{PE} is switched off ([58] Chapter 4.3).

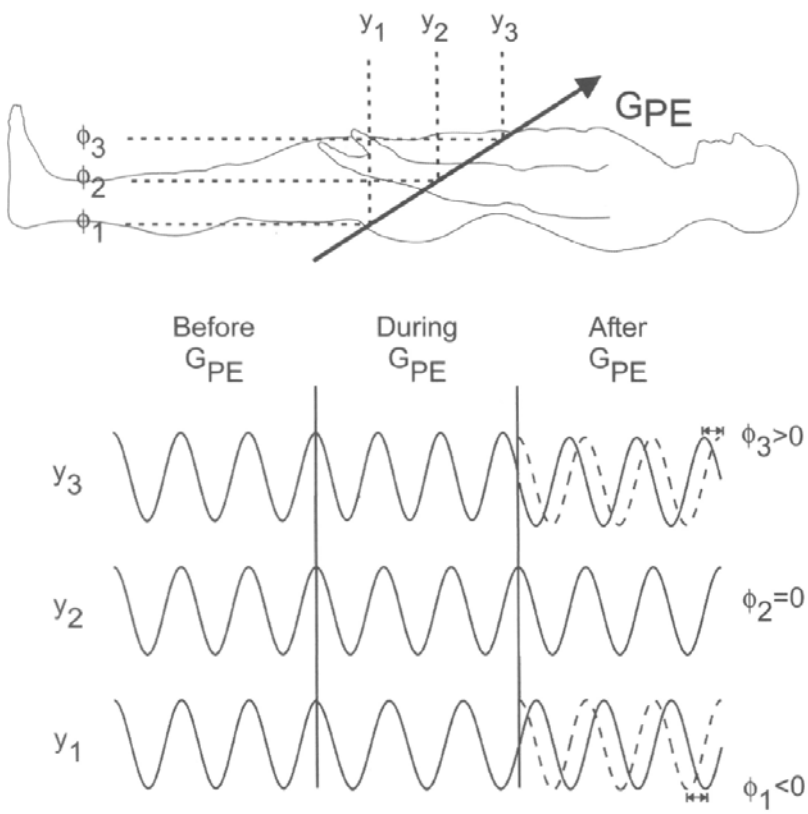

Figure 2.17: When G_{PE} is applied proton decreases or increases its precessional frequency depending on its position. Source: [58].

The spatial resolutions in the phase encode direction (mm/pixel) δ_{PE} is equal to the FOV_{PE} divided by the number of phase encoding steps in the acquisition matrix, N_{PE}. It should be noted as well that the FOV in the phase encode direction is not required to be the same as in the frequency encode direction. The ratio of the FOV_{RO} to the FOV_{PE} is called the aspect ratio. An aspect ratio of 1.0 means the voxel size is the same in both directions.

2.3.4 Sequence looping:

In MR applications many slices are measured to cover a large volume of tissue. Different approaches are used to acquire the data efficiently, reducing noise and decreasing scan times. MRI scanning uses repetitive executions, made possible by using loops in the MRI sequence ([58] chapter 4.4).

Traditionally one line of data is acquired for each slice during each TR time period and then the second line for each slice is acquired in next TR as shown in figure 2.18a. In another approach complete information for one slice is acquired before going to the next one as shown in figure 2.18b. The scheme in figure 2.18a is called multislice imaging, and is most often used.

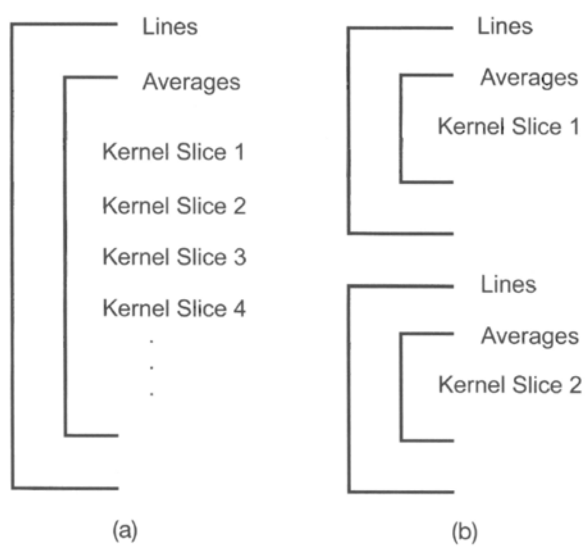

Figure 2.18: Two dimensional slice loop structures. Source: [58].

2.3.5 Radio Frequency excitation:

It was discussed above that an RF pulse is required to tilt the spin magnetization. In order to excite a slice of the sample, an RF pulse of a particular bandwidth must be applied in the presence of the magnetic field gradients. This bandwidth is achieved by shaping the pulse. The duration and shape of the pulse determines the range of frequencies on both sides of centre frequency. The phase and magnitude of the pulse determines the effective orientation and amount of rotation for the protons under consideration. RF pulses are classified on the basis of their shape called a pulse envelope. Non-selective pulses are of short duration and fixed amplitude and are often referred to as hard pulses. Frequency selective, or soft, pulses have longer duration allowing for narrow frequency bandwidth and their amplitude is not constant for all the frequencies within the broadcast. Soft pulses are used often in MRI sequences, as it is possible to excite narrow regions (slices) of tissues ([58] chapter 5.1).

In order to excite the whole slice, uniform amplitude and phase excitation is required throughout the slice. For that purpose, a sinc function is commonly used which includes all the required frequencies at the same phase with an amplitude modulation, for example as shown by the solid line in figure 2.19.

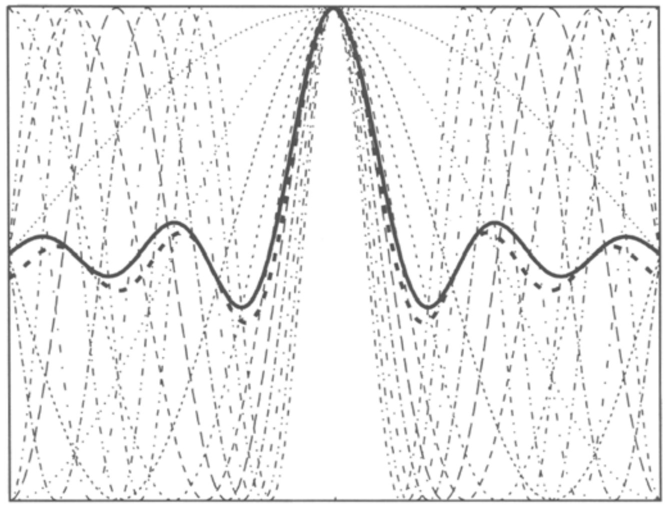

Figure 2.19: Sinc function. Source: [58].

2.3.6 Raw data and Image data:

The received echo signal (FID) is digitized and stored in a complex format. This raw data is kept in the form of a matrix where the horizontal direction is the read out direction (time axis of FID) and vertical direction is the phase encodes direction (Phase modulation). The size of the matrix depends upon the number of readout points N_{RO} and phase encoding steps N_{PE}. Figure 2.20 (a) shows the real data and 2.20(b) shows imaginary data of the image shown in figure 2.21. Each row is measured at a particular phase encode gradient level which corresponds to N_{PE} ([58] chapter 5.2).

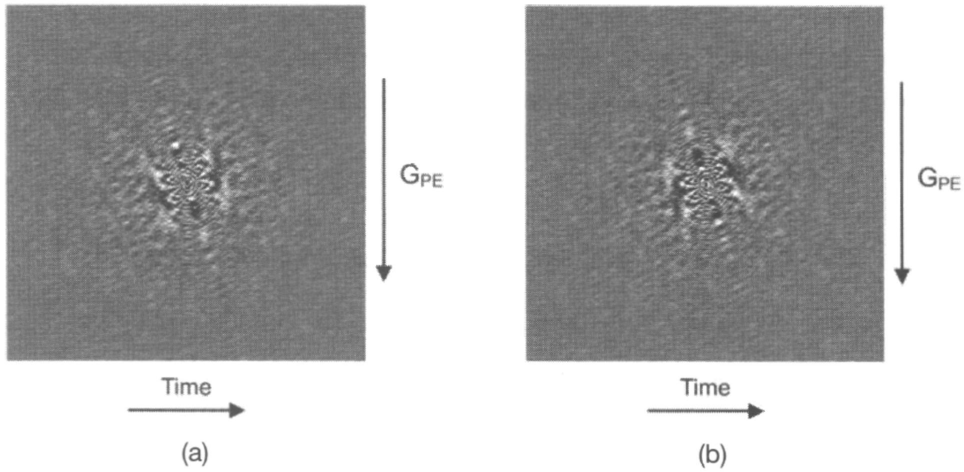

Figure 2.20: (a) Real raw data and (b) Imaginary raw data. Source: [58].

A 2D Fourier transform is applied to convert the raw data matrix into an Image matrix. The image matrix is a complex frequency and phase map of proton signal intensity weighted by the relaxation values of tissues. Values of the phase and frequency represent a particular location or pixel. Most often in MRI applications it is the magnitude of this complex data set that is used to generate the image, however in some applications, a phase image is required. Figure 2.21(a) shows a magnitude image and figure 2.21(b) shows the phase image of the real and imaginary data in figure 2.20.

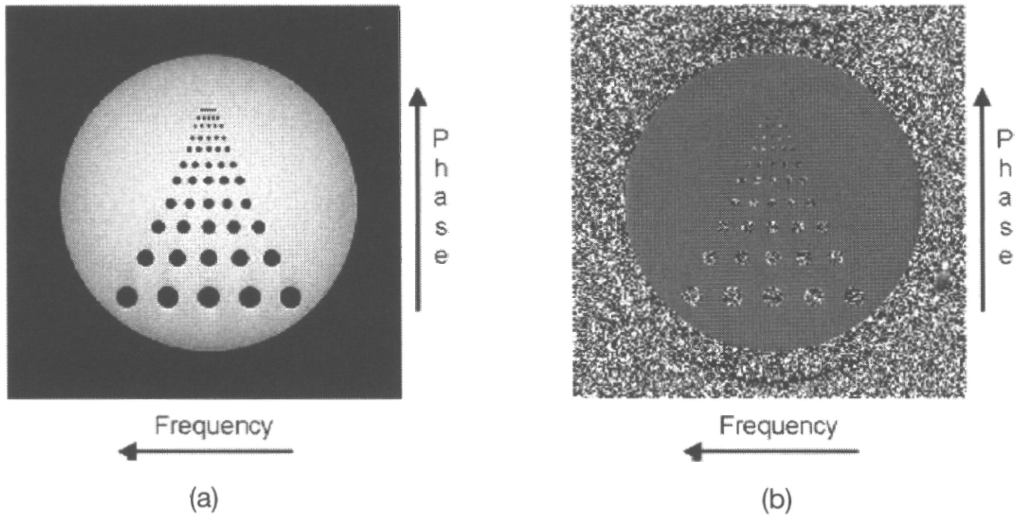

Figure 2.21: (a) Magnitude Image and (b) Phase Image. Source: [58].

2.3.7 K Space:

The raw data matrix shown in Figure 2.20 is considered in MRI to be representative of an inverse space (similar to lattice space in solid state physics) called K-space. In K-space the raw data is arranged as it is received and it holds the information about the location of that signal intensity in the image. In 2D imaging K-space is a two dimensional grid of points, k_x is proportional to the readout time and k_y is proportional to the phase encode gradient amplitude. This grid of points is illustrated in figure 2.22 ([59] Chapter 5.7.1). Each data point (k_x, k_y) represents the influence of the readout and phase encoding gradient areas (Gradient duration * Gradient amplitude) on the echo. According the sequence parameters, k_x, and k_y can be defined by (58, Section 5.3):

$$k_x = \gamma G_{RO} t_{RO}$$ Equation No: 2.7

$$k_y = \gamma G_{PE} t_{PE}$$ Equation No: 2.8

Where t_{RO} and t_{PE} are the times for which the respective gradients are active.

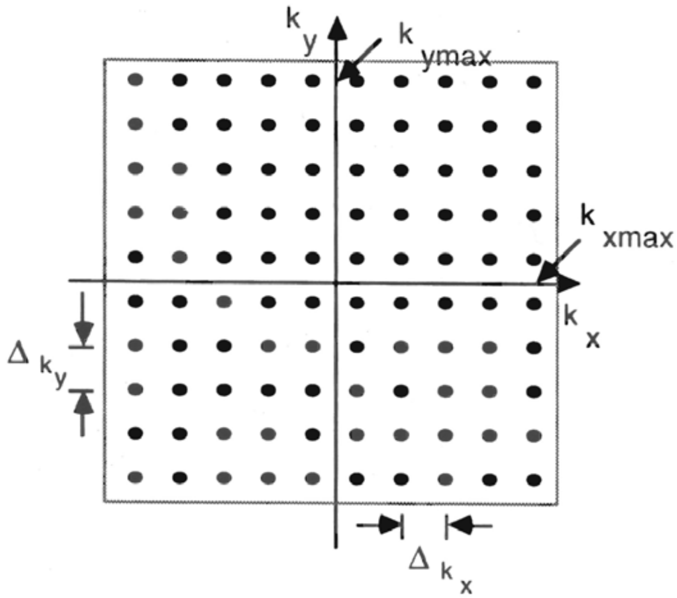

Figure 2.22: Sampling in K-Space. Source: [59].

Each data point in K-space contributes to the frequency, phase and amplitude of all locations within slice. However the maximum signal is located in the central part of k-space as these lines are acquired with low G_{PE} and is mainly responsible for the image contrast as shown in figure 2.23 (a, b). The outer portions have low amplitudes as they are acquired with high positive or negative amplitude G_{PE} and provide edge definitions as shown in figure 2.23 (c, d).

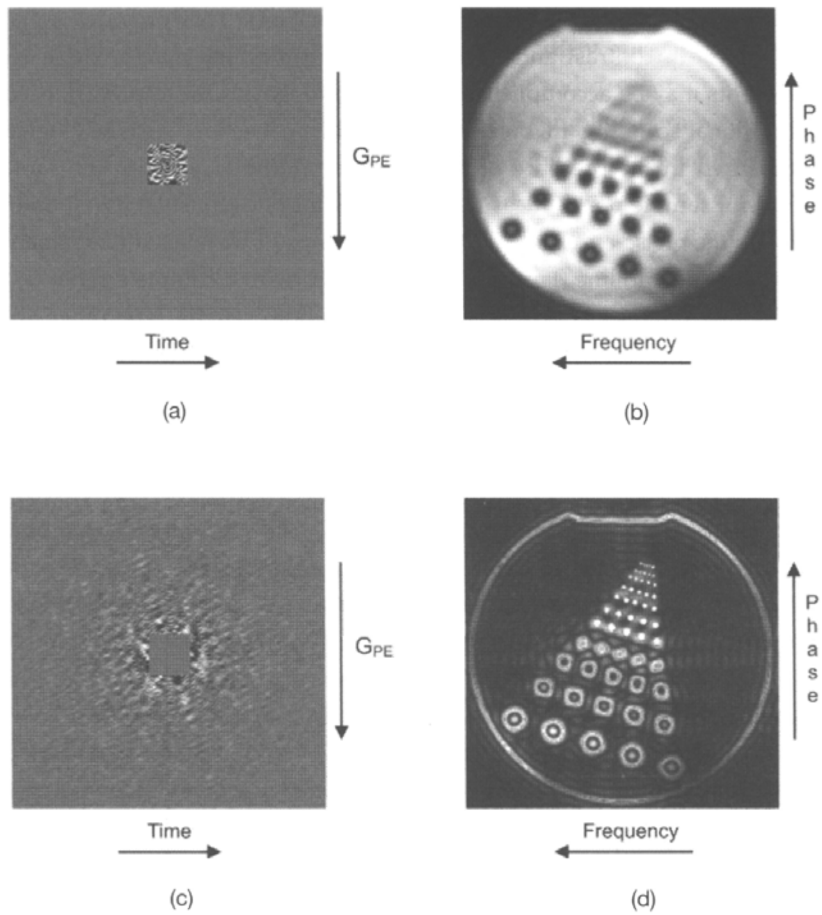

Figure 2.23: (a) Centre part of raw data in k-space. (b) Image reconstructed from raw data in (a). (c) Surrounding raw data leaving the centre part shown in (a). (d) Image reconstructed from raw data in (c). Source: [58].

k Values are measured in mm^{-1}. Changes in k in each direction $(\Delta k_x$ or $\Delta k_y)$, also called the sampling period is related to the field of view in that direction. Increasing the FOV decreases the sampling period in that direction keeping the gradient amplitude constant. For artifact free images, the raw data space should be sampled continuously with a constant Δk_x and Δk_y. This gives equal weight to contrast and edge definition in the final image.

Raw data in 3D scanning is a 3D volume defined with 3D coordinates (k_x, k_y, k_z). Change in k_z control the measurement in the slice direction. The centre of the K volume contributes most to the contrast and edges of the volume contribute edge definition in the final images.

Data in k-space can be placed in any order and this filling order is referred to as the k-space trajectory. Different MRI sequences use different types of trajectories. In fact many varieties of pulse sequences represent different approaches at sampling K-space. The simplest method is sequential filling in which the raw data matrix is filled with one k_x line at a time for one value of k_y starting from most negative G_{PE} and ending with most positive G_{PE} varying the G_{PE} in linear fashion.

2.4 Pulse Sequences and timing diagram:

A pulse sequence is the combination of RF and gradient pulses in order to generate an MR Image. All these pulses, gradients and their timings are controlled by the sequence code written in software. Some of the pulse sequence parameters are set by the operator such as TR, TE and FOV however their combination and high and low limits for different parameters are controlled by software code. Different vendors have different pulse sequences available with different names. To compare these sequences a timing diagram is used. A timing diagram is the schematic representation of different hardware components working during the sequence execution. Usually five lines are used to represent the timing diagram for the RF, Slice gradient, Readout gradient, Phase encode gradient and ADC (Analog to digital) converter timing. Elapsed time is from left to right.

As an example the timing diagram of a Gradient Echo with its corresponding sequential k-space filling is shown in figure 2.24 ([60] Chapter 7). Only four lines are shown representing the RF pulse, Phase encode gradient, frequency encode gradient and ADC. In K-space vertical axis is the phase encoding direction and the horizontal is the readout or frequency encodes direction. During the first TR at label A, the negative amplitude phase encoding gradient moves the data location to label B in k-space and with the application of the negative amplitude readout gradient moves to label C in K-space. At this point the opposite readout gradient is applied and data is sampled (points 1-8) stopping at the label D in K-space. The next RF pulse resets the spin phases and starts the process at label A again. The next data sample points (9-16) are collected in a similar fashion using appropriate gradients.

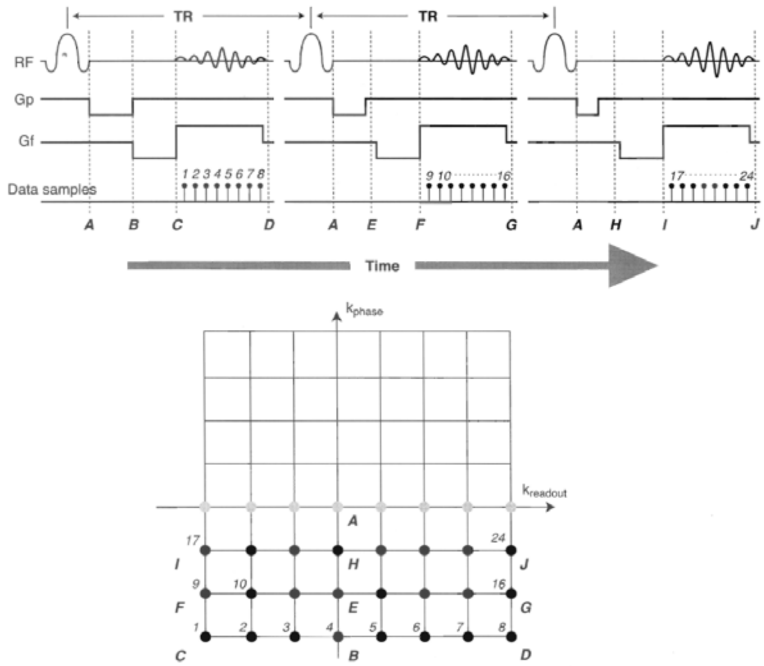

Figure 2.24: Timing diagrams of RF Pulse, Phase encode gradient, frequency encode gradient and ADC for GE sequence. Sample points in 2D K-Space for GE sequence. Source: [60].

2.4.1 Spin Echo (SE) Sequences:

The spin Echo is the most commonly used pulse sequence. It uses two RF pulses a 90 degree pulse and a 180 degree refocusing pulse that together generate a spin echo. A refocusing pulse is required for every received echo. An opposite polarity gradient is applied in the readout and slice direction to refocus protons at the same time as the spin echo. A spoiler gradient pulse is applied to dephase any residual magnetic field.

Two main types of spin echo sequences are used - single echo and multi-echo sequences, however more advanced spin echo sequences are also available. In single echo sequences, using a multislice loop structure, a single pair of excitation and refocusing pulses are applied per slice loop. Each echo is measured at the selected TE but with different amplitudes of phase encode gradient G_{PE} as shown in figure 2.25. Any changes in raw data amplitude from echo to echo is due to the change in the amplitude of phase encode gradient ([58] chapter 6.1).

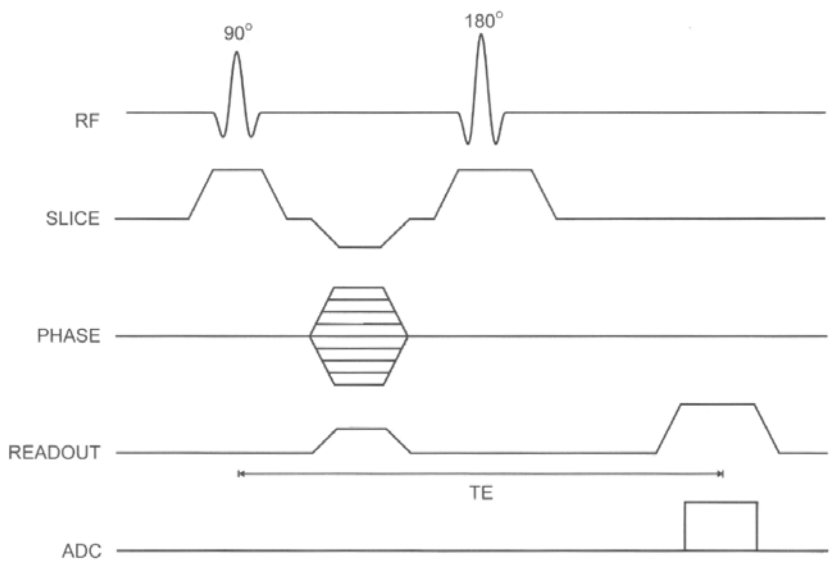

Figure 2.25: Spin Echo sequence timing diagram. Source: [58].

The multi-echo sequence has the option of applying multiple 180 degree refocusing pulses following the 90 degree excitation pulse. Each refocusing pulse produces an echo at different TE defined by the user as shown in figure 2.26. A single G_{PE} is used for each measurement and so the difference in raw data for each TE is due to the different levels of G_{PE}. However the difference in signal intensity from TE1 to TE2 is due to T2 relaxation.

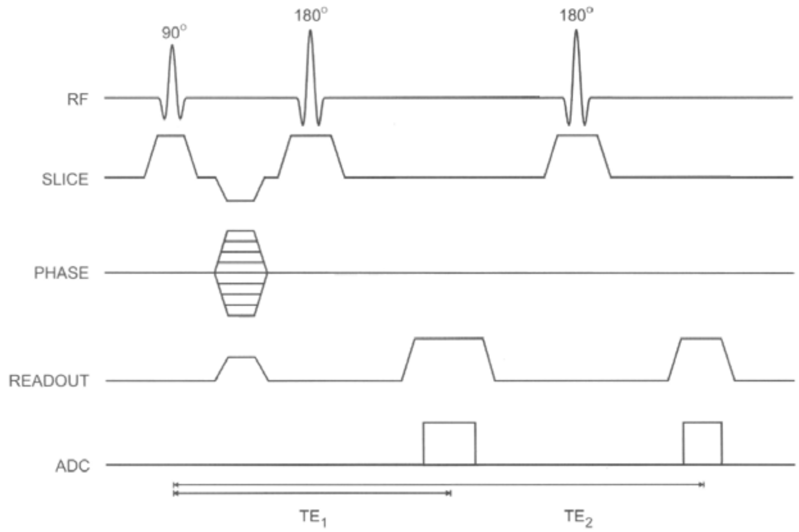

Figure 2.26: Multi Echo spin echo sequence timing diagram. Source: [58].

2.4.2 Gradient Echo (GE) Sequences:

In this type of sequence there is no 180 degree pulse required to generate an echo. The echo signal is generated by the use of gradient reversal. By applying a second gradient with same amplitude and duration but opposite polarity, the gradient induced dephasing is reversed and produces an echo called a gradient echo. The absence of the 180 degree RF pulses reduces the sequence kernel time and less RF power is applied to the patient. There is usually less signal in a gradient echo image compared to spin echo sequences, as the B_0 inhomogeneity and magnetic susceptibility contribute to signal decay. As well, the image quality of GE is more sensitive to metal implants and anatomy under scanning.

The simplest gradient echo is the spoiled gradient echo sequence which uses the spoiler or crusher pulses after signal detection to dephase transverse magnetization. So only the longitudinal magnetization contributes during the next excitation. Another approach varies the phase of RF excitation pulse to dephase transverse magnetization called RF spoiling. Figure 2.27 shows the spoiled gradient echo sequence where the polarity of the readout gradient is opposite to the readout pulse applied during signal detection. Spoiling is done at the end of the loop and at the slice and readout axes ([58] Chapter 6.2).

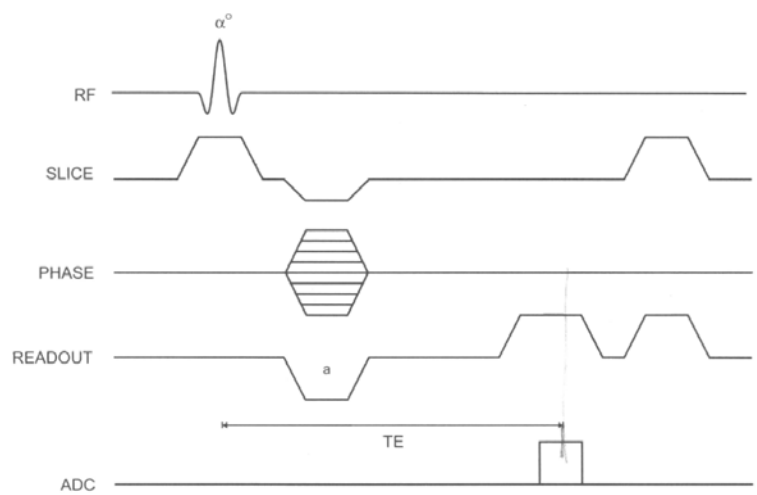

Figure 2.27: Spoiled Gradient echo sequence timing diagram. Source: [58].

2.4.3 Echo Planar Imaging Sequences (EPI):

In this technique several lines of k-space are sampled from one RF excitation. EPI can be SE or GE based and provides a very fast method of scanning. Signal is sampled continuously following the initial excitation. Series of gradient reversals are applied in the readout direction. Each cycle produces a gradient echo where the second half of each cycle is rephased by the first half of the next one. Two phase encoding techniques are used. First one is continuous phase encoding where the phase encode gradient is applied continuously and each echo is acquired with different phase and k-space is sampled in a continuous fashion. Second is a blipped phase encoding technique in which small amplitude gradient pulses are applied prior to the sampling period as shown in figure 2.28. Phase encoding for each echo is the same as no phase encoding pulse is applied during signal detection and raw data is acquired in a rectilinear fashion ([58] Chapter 6.3).

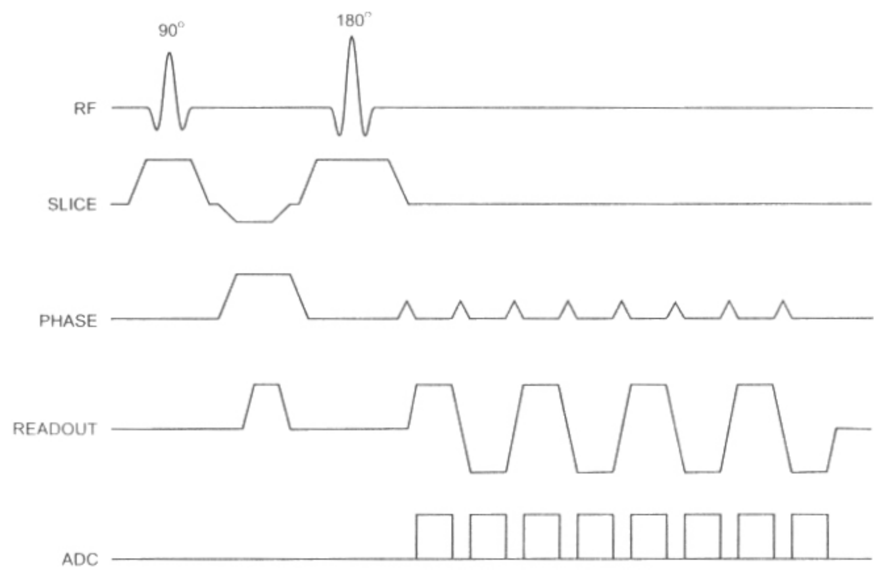

Figure 2.28: Echo Planar Imaging with blipped phase encoding. Source: [58].

Two types of EPI sequences available are single shot and multishot. Single shot acquires all phase encoding steps after the single excitation. Fast switching gradient amplifiers are required for single shot imaging. In multi-shot EPI, multiple acquisitions are interleaved using several excitations to cover all of k-space. Each acquisition is acquired at a different TE so the image TE is called an effective TE. EPI is susceptible to ghosting and geometric distortion artifacts due to the rapidly switching readout gradients.

2.4.4 Inversion recovery sequences:

An inversion recovery is a spin echo sequence with the addition of one 180 degree RF pulse before excitation. The 180 degree pulse inverts the proton magnetization within the slice giving enhanced T1 sensitivity at the time of 90 degree RF pulse excitation. The inversion time TI is user selectable parameter and controls the T1 excitation. A standard Spin Echo inversion recovery sequence timing diagram is shown in figure 2.29. Inversion recovery sequences require long TR as to allow for T1 relaxation between successive excitations ([58] Chapter 6.4).

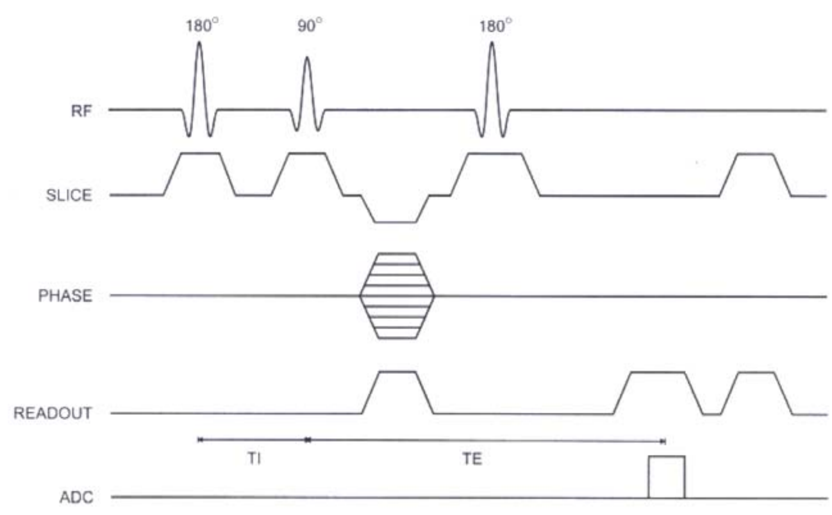

Figure 2.29: Standard Inversion Recovery Sequence where TI is inversion time. Source: [58].

Inversion pulses are also used for suppressing certain tissue signals with a suitable choice of inversion time TI. If TI is chosen so that the tissue of interest has no longitudinal component at the time of excitation, then that tissue has no contribution to the final image. The most common applications of inversion recovery sequences are the suppression of cerebrospinal fluid (CSF) and fat.

Chapter 3

Magnetic Resonance Elastography

3.1 Elasticity:

The stiffness of any material is something that is easily understood through our sense of touch. In some cases, the stiffness or elasticity of a tissue has a clinical value if the measurements can be made quantitatively and objectively and will be discussed in detail in section 3.6. In the human body, hard bones and soft tissues can be distinguished on the basis of stiffness. In a similar fashion, cancerous lesions have different elastic properties than healthy tissue [15, 16]. These stiffness properties fall under the category of the elasticity of the material. Hooke's law describes the material elasticity by using a spring model as [55]:

$$F = kx \qquad \text{Equation No: 3.1}$$

Where *F* is an applied force, *x* is the extension of the spring and *k* is the spring constant. Actual Hooke's law use negative sign in expression which makes *F* as the restoring force exerted by material. Consider an elastic Cube of height L as shown in Figure 3.1. When this cube is compressed with a normal force F_n per unit area (stress) from the top surface, there is a decrease in the height d. The normal strain S_n in the cube is equal to d/L. If the strain is small, then the following relationship follows from Hooke's law.

$$F_n = E \cdot S_n \qquad \text{Equation No: 3.2}$$

where E is called Young's modulus and represents the material stiffness.

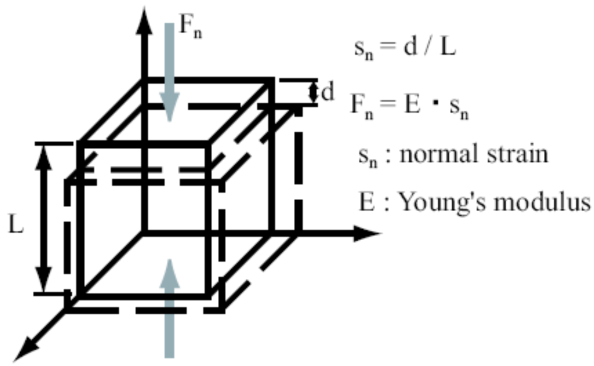

Figure 3.1: Relationship between young's modulus and Normal Strain. Source:[55].

If the force is applied parallel to top surface of the cube as a shearing force, the upper portion of the cube displaces by distance d as shown in Figure 3.2. The shear strain S_s is equal to d/H. The corresponding relationship between shear stress and shear strain is:

$$F_s = G \cdot S_s \qquad \text{Equation No: 3.3}$$

where G is called the shear modulus.

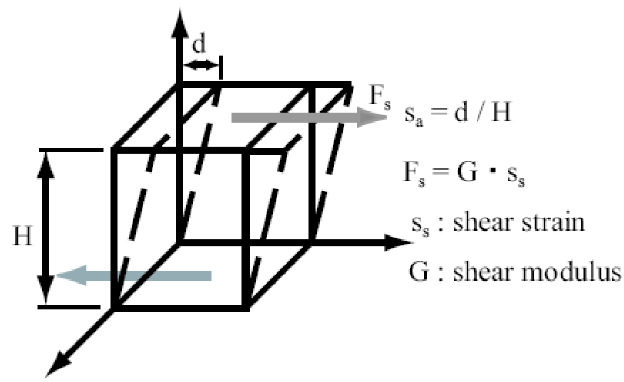

Figure 3.2: Relationship between shear Modulus and shear strain. Source:[55].

There are two elastic constants which describe the properties of a material. One is Bulk Modulus K which measures the substances resistance to uniform compression and the second is Poisson's ratio σ which is the ratio of the stretching of a material in one direction to the contraction of the material in the other direction. The Bulk modulus K and Poisson's ratio can be calculated from the Young's modulus and shear modulus as:

$$K = \frac{EG}{9G - 3E}$$ Equation No: 3.4

$$\sigma = \frac{E - 2G}{2G}$$ Equation no: 3.5

3.2 Magnetic Resonance Elastography:

Magnetic Resonance Elastography (MRE) is a technique that uses Magnetic Resonance Imaging to measure the elastic properties of different Tissues.

Research in measuring the elasticity of tissues first started in the field of ultrasound Imaging [61, 62, 29] and is still ongoing. Ultrasound images are acquired with and without compression and are correlated to measure the displacement at each location. A detailed history and review of Ultrasound elasticity is available elsewhere [63]. The sensitivity and resolution achieved with MRE can not be achieved with Ultrasound elastography [44].

The MRE technique induces motion in the region of interest using a vibration actuator. This motion is synchronized with motion sensitizing gradients (MSG) introduced in the MR sequence in a specific direction. A vibration actuator creates shear or compression waves in the object at the same frequency as the MSG. Any cyclic motion in the presence of the MSG generates a phase shift in the signal from which it is possible to calculate the displacement at each voxel and directly image the acoustic waves within the object.

One example MRE technique is proposed by Muthupillai and collaborators [35, 64] using shear waves in the range of 50-1000Hz as a probe. This frequency range is suitable as there will be less attenuation as compared to higher frequencies. Also the wavelength in the tissues is in the useful range of millimeters to tens of millimeters. Imaging the shear modulus promises to provide contrast as it varies widely in bodily tissues. Higher frequencies are not suitable as a probe because the wave propagation depends on the bulk modulus which varies little in soft tissues. Lower frequencies are also not suitable because they have too long a wavelength.

The MRE technique can be illustrated by considering the phase of a nuclear spin isochromat (group of spins resonating at the same MRI frequency) moving in the presence of magnet field gradient as given by [38]:

$$\phi(\tau) = \gamma \int_0^{\tau} \vec{G}r(t) \bullet \vec{r}(t) dt \qquad \text{Equation No: 3.6}$$

Where $\vec{G}r(t)$ is the time dependent magnetic field gradient, $\vec{r}(t)$ is the position vector of the moving isochromat and γ is the gyromagnetic ratio. In the case of a propagating harmonic acoustic strain wave spins undergo a simple harmonic motion about their mean position. For this reason consider the magnetic field gradient vector $\vec{G}r(t)$ as a set of basis functions to estimate the harmonic components of $\vec{r}(t)$. If the Gradient function can be truncated in time by an apodizing function $w(t)$, then equation 3.6 can be written as:

$$\phi(\tau) = \gamma \int_0^{\tau} \left[\vec{G}r(t).w(t) \right] \bullet \vec{r}(t) dt \qquad \text{Equation No: 3.7}$$

Where, $w(t) = \begin{cases} 1, 0 < t < \tau \\ 0, Otherwise \end{cases}$

This equation can be rewritten using a Fourier transform as:

$$\phi(\tau) = \gamma \int_{0}^{\tau} [\int_{-\infty}^{+\infty} \vec{\Gamma} r(f) \exp(j2\pi f t) df . w(t)] \bullet \vec{r}(t) dt$$

Equation No: 3.8

Where $\vec{\Gamma} r$ is the Fourier transform of $\vec{G}r(t)$. Equation 3.8 can be rewritten as:

$$\phi(\tau) = \gamma \int_{-\infty}^{+\infty} \vec{\Gamma} r(f) \bullet [\int_{o}^{\tau} w(t).\vec{r}(t) \exp(j2\pi f t).dt] df$$

Equation No: 3.9

This equation can then be written in terms of a convolution operation:

$$\phi(\tau) = \gamma \int_{-\infty}^{+\infty} \vec{\Gamma} r(f) \bullet \left[W(-f) \otimes \vec{R}(-f) \right] df$$ Equation No: 3.10

Where $W(f)$ and $\vec{R}(f)$ are the Fourier transforms of $w(t)$ and $\vec{r}(t)$ and $\otimes$ is the convolution operator. This equation shows that the gradient function can be considered to be a filter that measures a component of motion. In the case of propagating strain waves, the position vector is a pure sinusoid and can be given as:

$$\vec{r}(t) = \vec{r}_{\circ} + \xi_{\circ} \exp(j(\vec{k}.\vec{r} - \omega t + \alpha))$$ Equation No: 3.11

Where $\vec{r}_{\circ}$ is the mean position of the isochromat, ω is the angular frequency of the mechanical excitation causing the strain wave, α is the initial phase, $\vec{k}$ is the wave number and $\xi_{\circ}$ is the displacement. The magnitude of the gradient switching synchronously with the position vector is given by:

$$\left|\vec{G}r(t)\right| = \left\{+|G|; t \in [n\mathrm{T}, (2n+1)\mathrm{T}/2]\right.$$
$$\left|\vec{G}r(t)\right| = \left\{-|G|; t \in [(2n+1)\mathrm{T}/2, (n+1)\mathrm{T}/2]\right.$$

Equation No: 3.12

Where n = 0, 1, 2 ....N-1, the period of the oscillation is $T = 2\pi/\omega$, G is the gradient strength in Gauss/cm and || is the magnitude operation. The value of time duration τ of gradient function in equation 3.7 is chosen so that $\tau = NT$ in order that the dot product of the position vector and the gradient vector is zero. Also assuming that ramp times are negligible, and then the phase shift in the received signal is given by:

$$\phi(\vec{r},\alpha) = \gamma \int_{0}^{\tau=NT<TE} \vec{G}r(t) \bullet \xi_{\circ} \exp(j(\vec{k}\cdot\vec{r} - \omega t + \alpha))dt$$

Equation No: 3.13

Solving the integral for 0 to τ in equation no 3.13 and resultant equation is written below:

$$\phi(\vec{r},\alpha) = \frac{2\gamma NT(\vec{G} \bullet \xi_{\circ})}{\pi} \sin(\vec{k} \bullet \vec{r} + \alpha)$$

Equation No: 3.14

Equation 3.14 shows that the phase shift is proportional to the scalar product of the gradient vector and displacement vector and the period and number of gradient cycles. The above equation also shows that the measured phase shift depends on the initial phase between the gradient waveform and mechanical excitation. Choosing rather a sinusoidal gradient instead of the switching gradients equation 3.12 would yield the gradient described in equation 3.15:

$$\vec{G}r(t) = \begin{cases} G_\circ \cos(\omega t);\, t \in [0, NT] \\ 0 \; Otherwise \end{cases} \qquad \text{Equation No: 3.15}$$

Combining this equation with the phase shift yields:

$$\phi(\vec{r}, \alpha) = \frac{\gamma NT(\vec{G}_\circ \bullet \vec{\xi}_\circ)}{2} \cos(\vec{k} \bullet \vec{r} + \alpha) \qquad \text{Equation No: 3.16}$$

Which shows that spins with motion along the gradient vector, exactly in phase or out of phase with the magnetic oscillation, produce a maximum phase shift, and spins with a component of motion at 90 degrees to the gradient vector have no net phase shift. Usually two measurements are acquired by reversing the polarity of the motion encoding gradients between measurements. These two phase image measurements are subtracted to obtain a difference image which reflects the phase shift caused by propagating mechanical waves. Accumulating the phase shift over several cycles of motion gives a high sensitivity to small amplitudes [41, 42].

The speed of shear wave propagation υ in a simple isotropic material is related to the shear modulus μ and density ρ by the following relation:

$$\mu = \upsilon^2 \rho \qquad \text{Equation No: 3.17}$$

The speed of the shear waves can be calculated from this expression:

$$\upsilon = f\lambda \qquad \text{Equation No: 3.18}$$

Where the wavelength λ can be measured in an image showing propagating waves and frequency f is the frequency of applied motion. So the shear modulus can be estimated using equation 3.17 and 3.18. This calculation is very much simplified as the density of most soft tissues is approximately the same as water [65].

One MRE acquisition captures only one directional component of displacement however using motional encoding on all three axes can give the 3D displacement. There are three major components used in MRE. First is the vibration actuator used to induce cyclic motion in the object. The second is the modified pulse sequence with motion encoding gradients synchronized with the cyclic motion. The third part is the reconstruction software used to convert the phase information acquired with MRI into elasticity maps. These three components will be discussed in detail below.

3.3 Vibration Actuator:

In MRE, a vibration actuator is used to create continuous vibrations in the tissue being imaged. Different types of devices are used depending upon the tissue type and the location. It is also important to consider the frequency of vibration, since the velocity of the wave propagation and the attenuation in the body depend upon the frequency and amplitude. In fatty tissues, higher frequency waves are attenuated more compared to lower frequencies. The displacement required is in the range of several tens of micrometers to accurately acquire the elasticity distribution. Information about the frequency required for different applications will be discussed in section 3.6.

The vibration actuator must be compatible with the MR environment. All the electronic circuitry should either be outside the scanning room or at least 1-2 meters away from the magnet and properly shielded. Further testing on these devices can be done using five aspects: (1) Artifact tests, (2) SNR reduction measurement, (3) Geometrical distortion test, (4) Magnetically induced force and torque test and (5) Thermal test. Available devices can be categorized into three types [66]:

3.3.1: Type 1 Remote Actuation:

Vibration is transmitted from the actuation system located far from the scanner. Talwalker [67] presented a system where 60 Hz speaker vibration is transmitted to the patient via pneumatic tube as shown in Figure 3.3. A passive driver is placed on the patient’s body over liver.

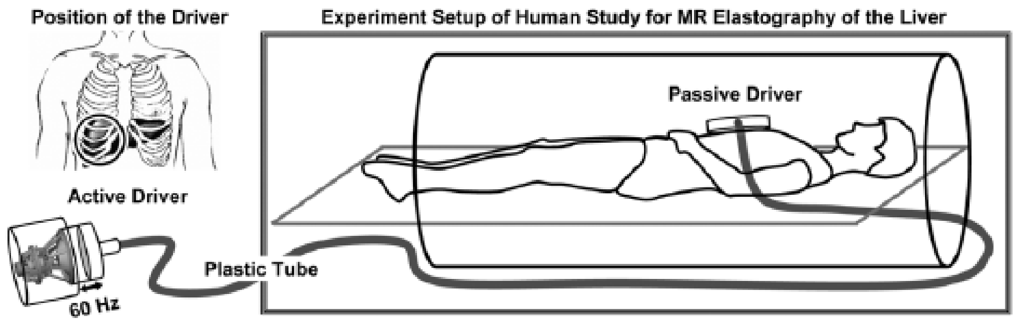

Figure 3.3: Shear Waves application for Liver MR Elastography. Source: [67].

Sack [13] presented a system where speaker vibration is transmitted to a head rocker through a 2.8m rigid carbon fiber rod as shown in figure 3.4. The head rocker is a round compartment that sits on a roller for ease of movement. The carbon fiber rod eliminates the phase lag problem in pneumatic systems. Phase lag is the delay in motion due to the mechanical and pneumatic limitations.

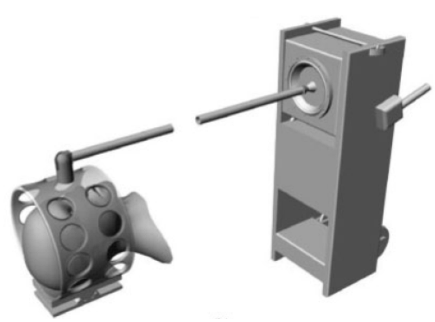

Figure 3.4: Head rocker unit and remote vibration generator for shear wave excitation of human brain. Source: [13].

Lewa [68] used a commercial vibration generator (vibrator 4810 Bruel-kjaer, Narum, Germany) with a long Plexiglas rod to vibrate a phantom. The vibration generator contains a permanent magnet so it has to be far from the MR magnet as shown in Figure 3.5.

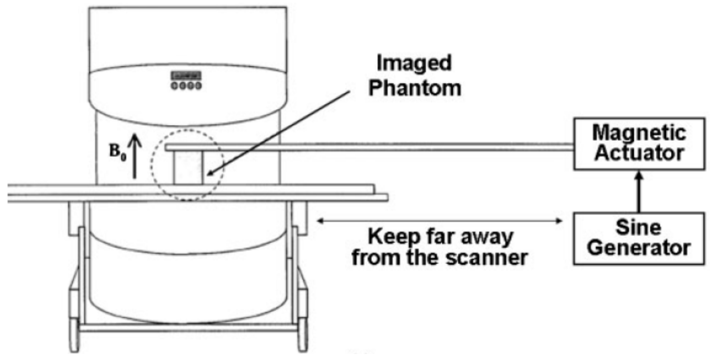

Figure 3.5: Commercial vibrator with long plexiglas rod. Source: [68].

Bishop [69] used an ultrasonic motor USR60 (Shinsei Corporation Inc) which is compatible with the MRI environment. It is still recommended to keep this motor 0.5 m away from the magnet isocentre. A cam shaft is used to convert the rotary motion of 1-2 Hz into linear motion as shown in figure 3.6 used for compression studies. Based on the same principle Plewes [70] proposed a vibrator for breast elastography shown in figure 3.7. This figure shows that the vibrator is attached to the side of the commercial phased-array breast coil. An ultrasonic motor rotates the driveshaft. The moving plate is connected to the driveshaft and displacement of the plate is shown by the dotted line.

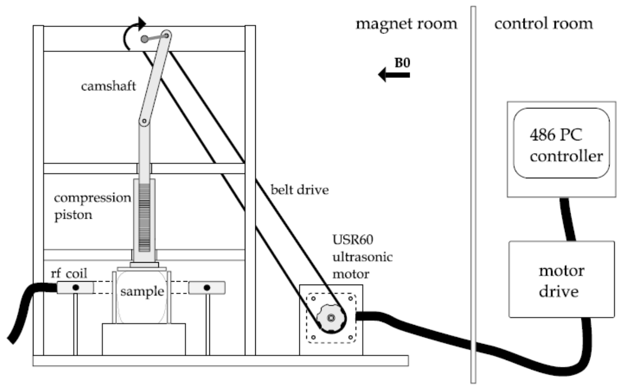

Figure 3.6: Ultrasonic motor used for compression studies. Source: [69].

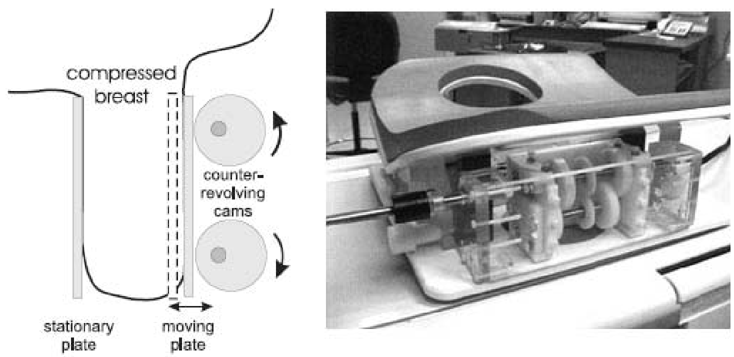

Figure 3.7: Compression device for elastography with commercial phased array breast coil. Source: [70].

3.3.2: Type II: Electromagnetic coil in the magnetic field

In this method, an electromagnetic coil is placed in the main magnetic field. When a sine wave is passed through the coil, the coil starts to vibrate due to the alternating magnetic field created in the coil interacting with the main magnetic field. This coil [55] is usually mounted on one side of a lever and a moving arm is fixed on the other side. The lever is pivoted in the middle so that it can rotate as shown in Figure 3.8. A waveform generator and amplifier are used to generate the sine wave in the coil. This idea was first presented by Muthupillai et al [35, 38].

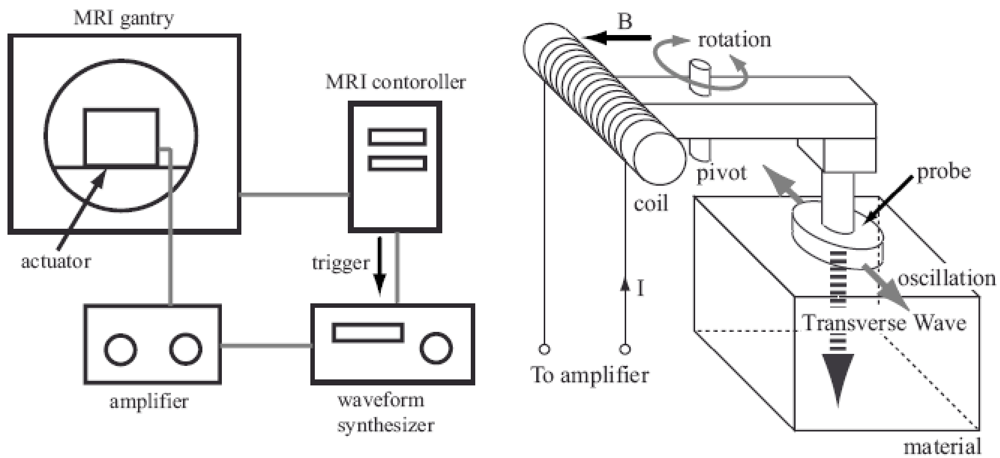

Figure 3.8: Block diagram of MRE acquisition and actuator**.** Source: [55].

A variation of this approach will be used in this thesis. In order to get a clear picture of wave propagation in some tissues like muscles it is necessary to induce the motion in different spatial directions. Usually electromagnetic actuators induce motion only in one direction. In order to generate motion in different directions, Braun [71] designed an electromagnetic actuator which is capable of generating variably oriented shear waves and is shown in figure 3.9. A redirection plate is used between the excitation plate and the coil. Inserting the excitation plate at different holes in the redirection plate makes it possible to induce motion in different directions.

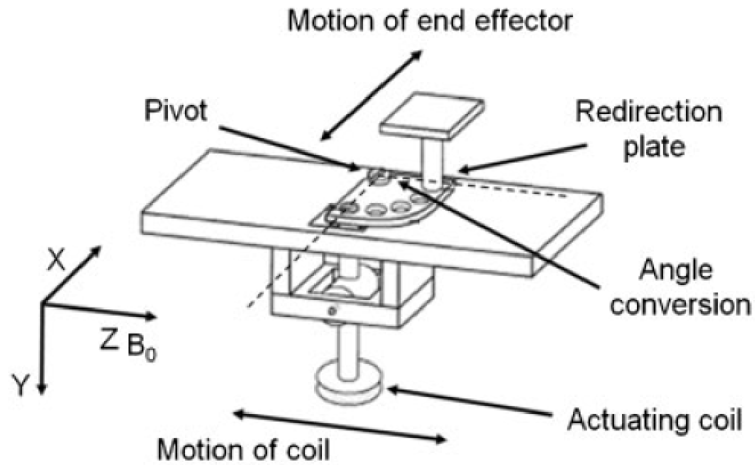

Figure 3.9: Redirection actuator. Source: [71].

Electromagnet drivers are generally inexpensive and simple in terms of design and implementation. But they are not flexible for use in different types of applications. The vibration amplitude is dependent on the number of turns and the current induced in coil. The current in the coil can also create an artifact in regions that are proximal to the coil.

3.3.3: Type III: Devices near vibrating region:

In this type of actuator, piezoelectric materials are employed near the vibrating region. Piezoelectric materials are capable of converting electrical energy into mechanical motion and vice versa. Piezoelectric composites are made of MR compatible materials – copper, silver and ceramics. A piezoelectric crystal changes shape when an electric potential is applied [72], and this motion can be used to create precise vibrations.

Doyley [73] developed an MRE driver using a piezoelectric actuator. A sinusoidal voltage of 100 Hz is applied from a signal generator and a maximum displacement of 40μm was achieved with this design. The design used a pure plastic casing as shown in figure 3.10, to make it fully MR compatible.

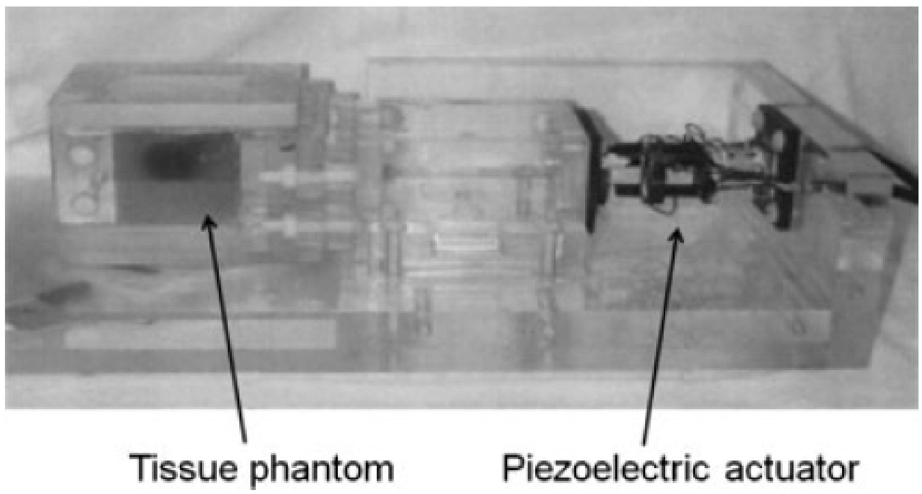

Figure 3.10: MR compatible piezoelectric actuator. Source: [73].

By increasing the number of elements in the piezoelectric stack, higher displacements can be achieved. The maximum elongation of the stack is directly proportional to the length of the material. Uffmann [74] developed a device shown in figure 3.11a for MRE applications which can generate a peak-to-peak amplitude of up to 1mm. The piezoelectric stack is 247mm long and 18.5mm in diameter. A lever is used to amplify the mechanical motion. A computer aided design plan of the device is shown in figure 3.11b. The body of the device is made from aluminum and some smaller parts are made from titanium, brass and copper-beryllium which are all non-magnetic materials. The piezoelectric stack expands with the application of high voltage and a helical spring provides the restoring force to push the stack back to its resting position.

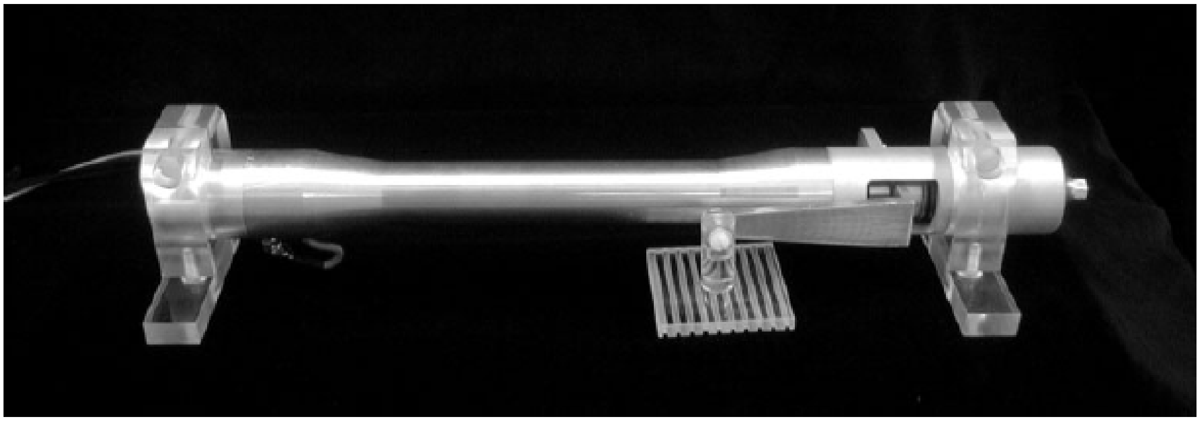

(a)

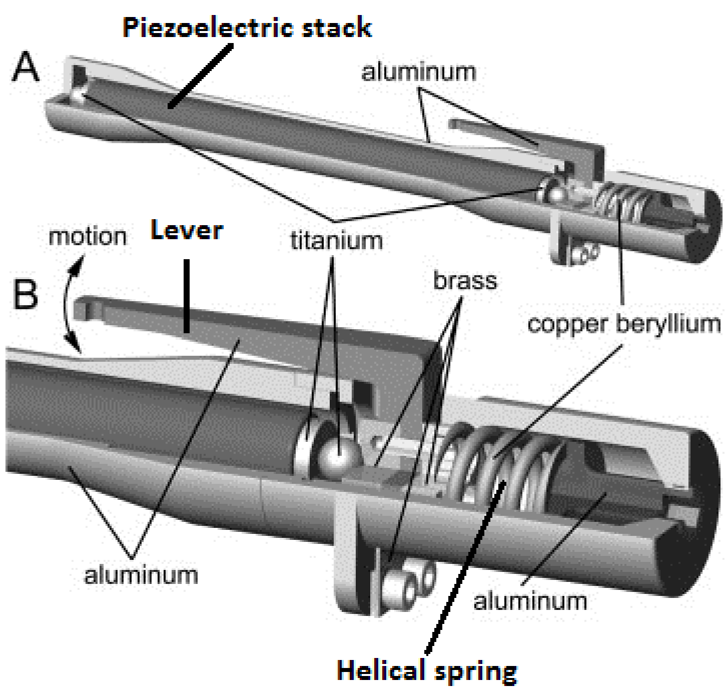

(b)

Figure 3.11: (a) Plexiglas actuator. (b) CAD Plan of actuator. Source: [74].

Instead of using a "Piezostack," Chan [75] used a commercially available piezoelectric bending element (D220-A4-503YB: Piezo Systems Inc. [76]). Figure 3.12 shows a needle connected to the bending element vertically. The bending element consists of two layers of piezoelectric material. With the application of voltage one layer contracts and other expands creating a displacement of 200μm at the tip of the needle.

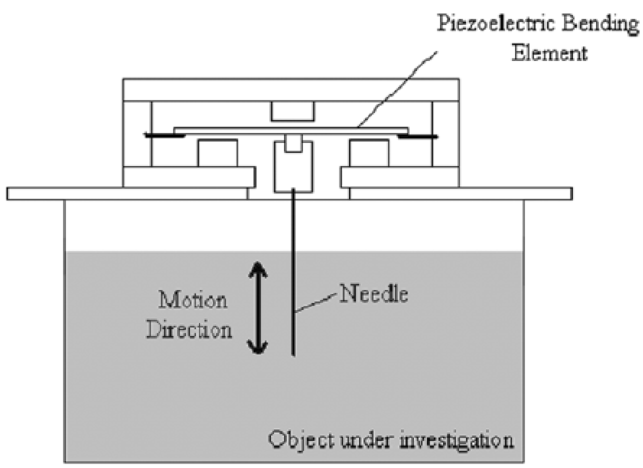

Figure 3.12: Bending element producing longitudinal motion. Source: [75].

Piezoelectric bending elements are capable of producing very accurate and stable vibrations. But they are expensive and required special high voltage amplifiers.

Ultrasound transducers are also used in MRE to generate radiation forces inside the body [77]. This radiation force is localized and highly directional. These transducers were not discussed in detail.

3.3.4: Summary:

Different types of actuators were discussed depending on their technique and functional location however their design also depends to certain extent on the area of clinical application. Actuators with excitation coil and piezoelectric elements are easy to use and show better performance in terms of their response and displacements.

To accurately assess the elasticity of a region, the actuator should be capable of transmitting the waves to the whole region of interest with significant amplitude. Different solutions were presented in this regard and one of the best solutions is to use multiple drivers. Zheng et al [78] used twin drivers attached to the same rod and concluded that the twin drivers are capable of detecting small inclusions better than a single driver. The twin driver elasticity map clearly shows the small inclusions which are not present in the single driver elasticity map. Further improvement is achieved by Yogesh [79] by inventing a phased-array acoustic driver system in which eight drivers are used with their own excitation coils. Independent signals are provided to eight coils through eight channels of an analog output board, feeding synchronous sine waves. This driver is capable of inducing uniform waves and thus elastograms are more uniform and artifact free. Yin et al [80] compared transverse and longitudinal drivers in different imaging planes and proved that longitudinal drivers are better in certain applications like Brain, Liver, thigh muscles and heel fat pads. Longitudinal drivers provide better penetration and hardware design flexibility. The wave patterns generated by these excitations are illustrated in figure 3.13.

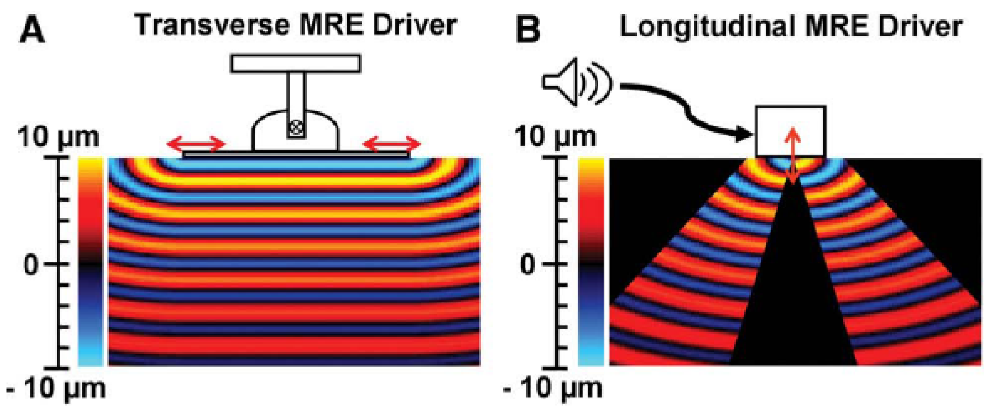

Figure: 3.13: Comparison of transverse and longitudinal MRE drivers. (A) Planar shear wave is generated with transverse driver. (B) Cone like hemispherical shear wave field is generated with longitudinal driver. Source: [80].

3.4: MRE Sequence:

For MRE, motion encoding gradients (MEGs) must be added into the MRI sequence in order to obtain information about the traveling waves. MEGs are a kind of Flow-Encoding (FE) gradient whose purpose is to measure the flow velocity. This concept was introduced by Moran [30] in 1982. MEGs can be added to any one of the three logical axes (readout, phase encoding and slice selection) and only provides motion or flow information with respect to that axis.

P. Van Dijk [32] describes that the phase shift for uniformly moving spins is different than that for stationary spins. For a given location, the phase shift is proportional to the gradient amplitude and timing. Figure 3.14 shows a unipolar gradient after the application of a 90 degree RF pulse.

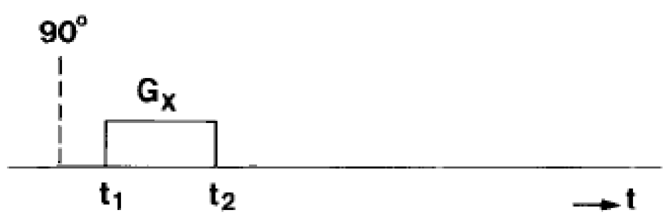

Figure 3.14: Unipolar gradient after 90 degree RF Pulse. Source: [32].

For stationary spins $(x = x_\circ)$ phase shift at $t = t_2$ is:

$$\phi_s = \gamma G_x x_\circ (t_2 - t_1)$$ Equation No: 3.19

For moving Spins $(x = x_\circ + v_x \cdot t)$:

$$\phi_m = \gamma G_x x_\circ (t_2 - t_1) + \frac{1}{2} \gamma G_x x_x v_x (t_2^2 - t_1^2)$$ Equation No: 3.20

Where γ is the gyromagnetic ratio, G_x is the gradient field in the x direction, $x_\circ$ is the x coordinate of the spin at the moment of the 90 degree RF excitation and v_x is the velocity of the spins.

In the case of a Spin Echo sequence, a 180 degree pulse is added which forms an echo by spin rephasing ([81], section 14.3). This echo is measured in the presence of another gradient G_x as shown in figure 3.15.

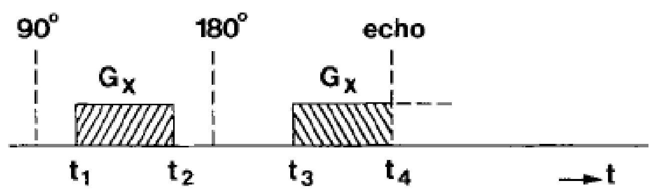

Figure 3.15: Second Unipolar gradient added after 180 degree RF Pulse. Source: [32].

The same G_x Gradient applied after the 180 degree RF pulse produces a negative phase shift. If the area under these gradients is the same, then the net phase of the stationary spins is zero.

IE) For stationary spins the phase shift at $t = t_4$,

$$\phi_s = 0 \qquad \text{Equation No: 3.21}$$

And for moving Spins

$$\phi_m = \frac{1}{2}\gamma G_x x_x v_x (t_2^2 - t_1^2 - t_4^2 + t_3^2) \qquad \text{Equation No: 3.22}$$

This extra phase shift is responsible for creating the phase image, which gives us information about the moving spins. Phase information can be retrieved from the real and imaginary values present in the image information. Sequences using this technique are called phase contrast sequences.

The most common FE Gradient is the bipolar gradient, which comprises two lobes of equal and opposite polarity as shown in figure 3.16. Because the net area under the bipolar gradient is zero, it produces no phase accumulation for stationary spins but produces phase accumulation for the moving spins in the direction of the gradient (section 2.2 [7]).

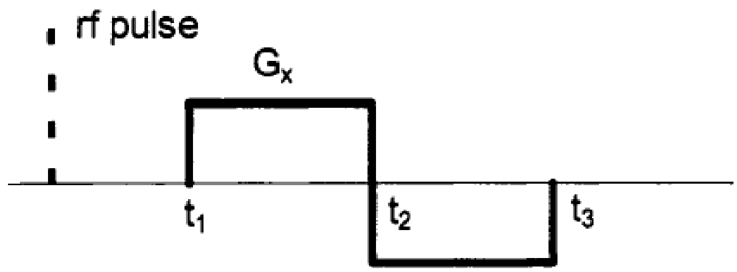

Figure 3.16: Bipolar Gradient. Source: [7].

For a bipolar gradient, equation 3.22 can be written as:

$$\phi_m = \frac{1}{2}\gamma G_x x_x v_x (2t_2^2 - t_1^2 - t_3^2)$$ Equation No: 3.23

For MRE, synchronized motion sensitizing gradients are used. The gradient waveform consists of a train of bipolar gradients. A single bipolar gradient produces a minimum phase accumulation but the net effect of the entire train is easily measurable (Section 9.2 [81]). The train is synchronized with the oscillation of a mechanical actuator with an option of introducing an adjustable delay between the motion and MEG to measure the wave at different phases which will help in reconstruction of elasticity map. Mainly Spin Echo (SE) and Gradient Echo (GE) sequences are used for MRE studies. There are some differences in the application of MEG in SE and GE, which will be discussed below.

3.4.1 Spin Echo Sequence for MRE:

In a SE sequence, MEGs are added before and after the 180-degree pulse as shown in figure 3.17. In this figure, a typical MR pulse sequence is depicted with the appropriate changes needed for MRE. A pulse sequence diagram depicts the amplitude of gradients and RF pulses on the ordinate versus time on the abscissa. Since the phase of the nuclear spins is flipped by the 180-degree pulse, the second set of MEGs is polarity reversed. This second set of MEGs with reversed polarity adds to the net phase accumulation due to the motion. The SE produces only one phase image with very little phase background. Moran [31] explained that applying a MEG after a 180 degree RF pulse has the same effect as taking another set of measurement with the reverse MEG polarity, in the case of GE, and forming a phase difference map from these two sets.

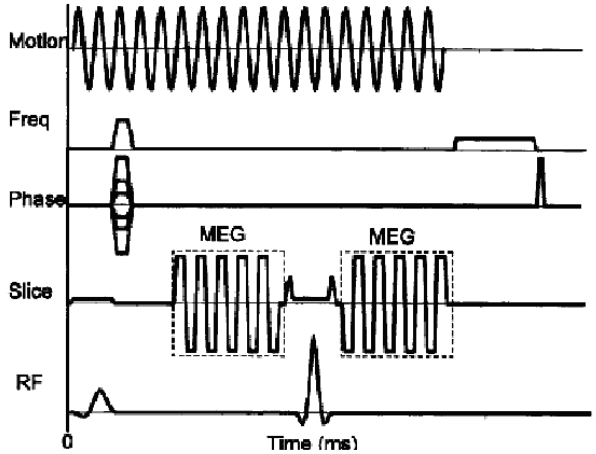

Figure 3.17: Pulse sequence diagram for SE Elastography. Source: [7].

Hamhaber [82] used a SE in the comparison of shear wave MRE and mechanical compression tests. Figure 3.18 shows the pulse sequence diagram where motion-encoding gradients are added before and after the 180-degree pulse with an option of applying them to different axis as required. Where α is the delay between motion and MEG.

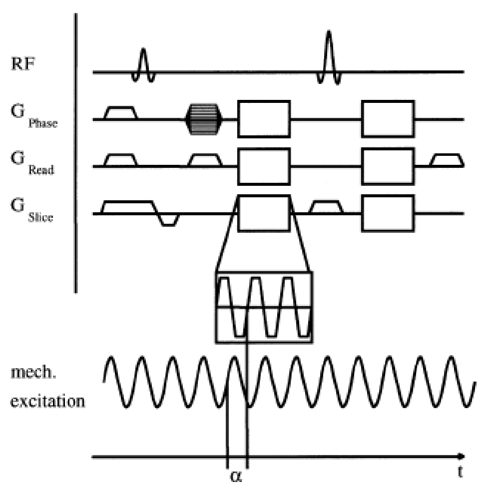

Figure 3.18: MRE SE Pulse Sequence Diagram. Source: [82].

3.4.2 Gradient Echo Sequence for MRE:

In the case of GE two sets of repetition times are needed one with a positive polarity MEG and the other with a negative polarity MEG (Section 13.5 and15.2, [81]). Taking the difference between the positive and negative polarity phase image creates a phase difference map. This method is used to remove any unwanted contributions to the phase due to system imperfections.

These system imperfections are Bo inhomogeneities, gradient eddy currents, chemical shift and magnetic susceptibility variations. This unwanted phase contribution is more severe in GE sequences. Figure 3.19 shows a GE MRE pulse sequence timing diagram with a positive polarity MEG. A second sequence is repeated with the only difference being that the MEG starts with a negative polarity.

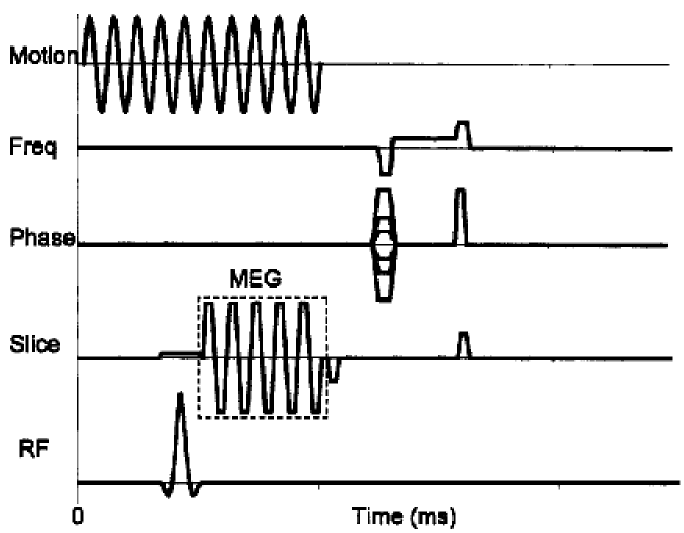

Figure 3.19: Pulse Sequence diagram for GE MRE with positive polarity MEG. Source: [7].

Muthupillai [38] used a modified GE sequence to study transverse acoustic strain waves. Repetition 1 and Repetition 2 were acquired for each measurement with opposite polarity MEGs (called Motion sensitizing gradients in paper). MEGs can be applied on any axis after the RF pulse as shown in figure 3.20. Synchronous trigger pulses were used to trigger the waveform generator for cyclic motion. α is the delay between the motion and the MEGs.

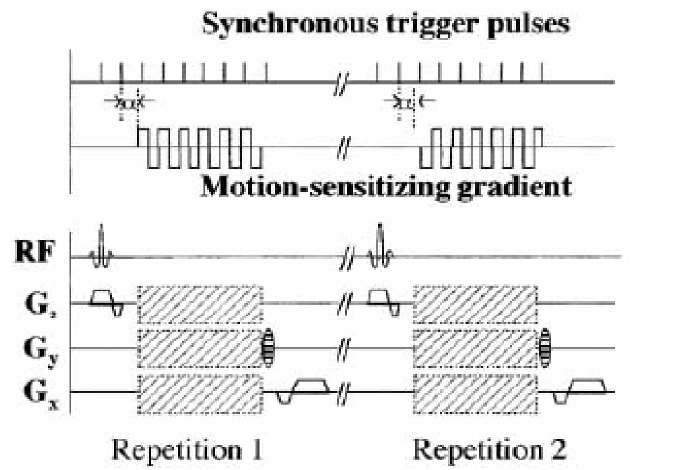

Figure 3.20: MRE GE Pulse sequence used by Muthupillai. Source: [38].

A major concern in MRE acquisitions is the scan time. With the introduction of MEGs in the sequence, the minimum time required for the sequence is already increased. Also it is advantageous to capture the motion at different phase offsets between motion and MEG (for example eight offsets) which helps in acquiring the motion information at different instances. Usually one motion cycle is divided into equal offsets and information acquired using these offsets gives information about the complete cycle of traveling waves in object. To get a clear picture of motion in all spatial directions, the sequence is repeated three times with a MEG applied on each axis. All these factors increase the scan time drastically. To address this issue Maderwald's group [83] presented a paper in 2006 using a multi-echo phase-contrast gradient-echo sequence. This sequence generates a number of echoes from a single RF excitation. The number of echoes can be selected (for example 1,2,4,8 and 16). The advantage of using this sequence is the reduction in time, fewer RF pulses and fewer blocks of MEGs. The disadvantage is that ghosting artifacts began to appear at higher numbers of echoes.

3.4.3 Shape of the Motion Encoding Gradients:

Motion encoding gradients are commonly a sinusoidal or trapezoidal shape. Dunn [56] ran a comparison study in 2005 and found that sinusoidal gradients are 21.5% less efficient than the trapezoidal gradients in encoding phase. The shape of gradients is shown in figure 3.21.

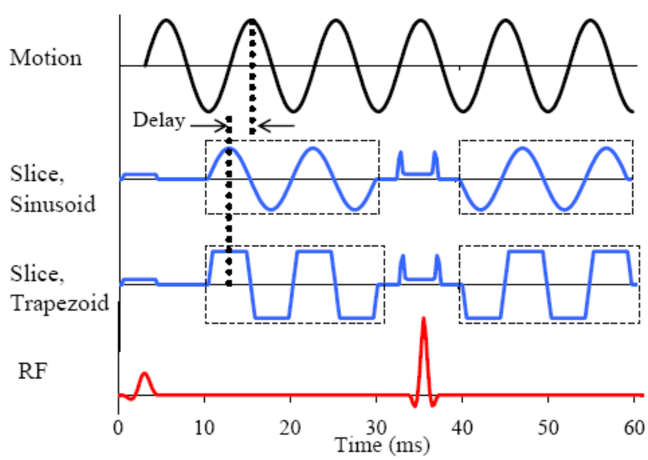

Figure 3.21: Spin Echo Pulse Sequence Comparing Sinusoidal and trapezoidal MEG on Z slice axis. Source: [56].

3.4.4 3D Gradient Echo Sequence for MRE:

Weaver et al: [84] presented in 2001 a 3D Gradient Echo sequence for MRE. Volumetric MR phase images are acquired at different phase offsets. Then this information is converted into 3D displacement information. These results proved that the phase images acquired with a 3D GE sequence are of high quality and high quality elasticity maps can be acquired using 3D reconstruction techniques. Elasticity maps acquired are capable of estimating the elastic properties at MR voxel resolution.

3.5 MRE Reconstruction:

Raw data received in MRI after the Fourier reconstruction has both the magnitude and phase for each pixel in the complex image. Phase information is discarded when the standard image reconstruction is done. The phase information present in the raw data is used to measure the motion in the object being imaged. The unwanted contributions to the phase first need to be removed before correct motion information can be obtained.

3.5.1 Phase Difference Calculation:

As mentioned earlier, in case of a GE, two acquisitions are acquired with opposite bipolar gradients. A Phase difference map is obtained by calculating the phase difference between the two phase images on a pixel by pixel basis. The resulting map is a clear picture of the transmitted strain waves (Section13.5 [81]). Consider a single identical pixel in both images. The complex value of the pixel in the first image Z_1 is given as:

$$Z_1 = x_1 - iy_1 = \rho_1 e^{i\phi_1}$$ Equation No: 3.24

And in the second image:

$$Z_2 = x_2 - iy_2 = \rho_2 e^{i\phi_2}$$ Equation No: 3.25

The phase difference for the above pixel is given as:

$$\Delta\phi = \arctan\left(\frac{y_1}{x_1}\right) - \arctan\left(\frac{y_2}{x_2}\right) = \phi_1 - \phi_2$$ Equation No: 3.26

In order to save processing time, it is preferable to form the complex ratio and then extract the phase as:

$$\Delta\phi = \angle\left(\frac{Z_1}{Z_2}\right) \equiv \arg\left(\frac{Z_1}{Z_2}\right) = \angle(\rho_1\rho_2 e^{i(\phi_1-\phi_2)}) = \arctan\left(\frac{\mathrm{Im}\left(Z_1/Z_2\right)}{\mathrm{Re}\left(Z_1/Z_2\right)}\right)$$

Equation 3.27

The above equation can be simplified by replacing inverse of the complex number Z_2 with its complex conjugate, Z_2, as both have the same phase.

$$\Delta\phi = \angle\left(Z_1 Z_2^*\right) \equiv \arg\left(Z_1 Z_2^*\right) = \arctan\left(\frac{\mathrm{Im}\left(Z_1 Z_2^*\right)}{\mathrm{Re}\left(Z_1 Z_2^*\right)}\right)$$ Equation 3.28

To further reduce the artifacts it is beneficial to use the four-quadrant arctangent function, often called ATAN2 in programming languages (Fortran, Matlab). Equation 3.28 can be written as:

$$\Delta\phi = \arctan\left(\frac{\mathrm{Im}\left(Z_1 Z_2^*\right)}{\mathrm{Re}\left(Z_1 Z_2^*\right)}\right) = \mathrm{ATAN2}\left[\mathrm{Im}\left(Z_1 Z_2^*\right), \mathrm{Re}\left(Z_1 Z_2^*\right)\right]$$ Equation 3.29

The four-quadrant arctangent function checks the sign of two arguments before forming their ratio. If the numerator and denominator are both positive ATAN2 returns the value in the first quadrant and if both are negative returns value in third quadrant. Because of this, the dynamic range is extended from (-π/2, π/2) to (-π, π). This increased range further helps in reducing the phase wraps.

3.5.2 Phase Unwrapping:

The measured phase for a one dimensional signal vector can have values from 0 to 2π or –π to π. However if the vector is in motion rotating about a unit circle then the cumulative or total phase of the signal can exceed the above values after one complete rotation. So the total phase is not only the current phase but representative of its total duration from the initial position. If the signal completes more than one full rotation then the acquired signal is said to have "wrapped around" or has "phase wrap". The process of measuring the total accumulated phase is called phase unwrapping.

Figure 3.22 shows an example of phase wrap in a one dimensional signal (Chapter 2.4.2 [7]). Normal signal is in the range of – π to π. The solid line with circles in the left picture of figure 3.22 shows actual signal. At point A on time axis, the signal is greater than π so the value is wrapped back into the range represented by a negative value within the allowed range. Values outside the range of – π to π are wrapped and represented by dotted lines in the left picture of figure 3.22.

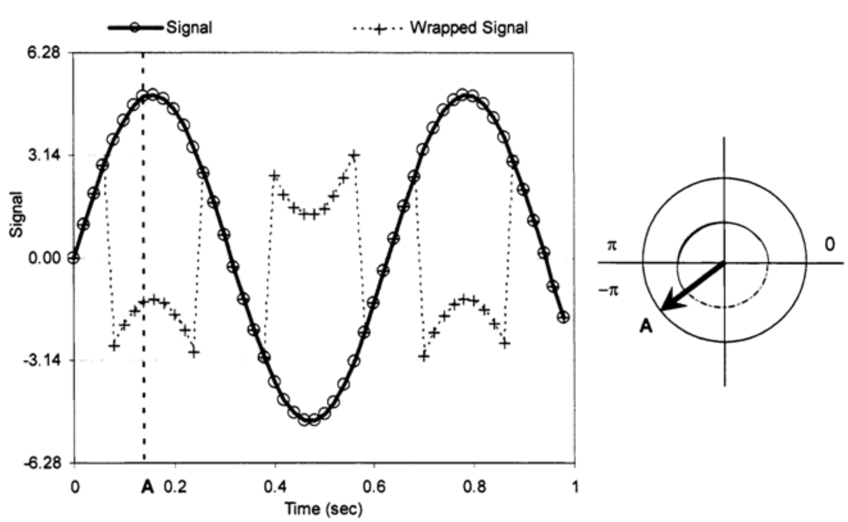

Figure 3.22: Left, Phase wrap of a one dimensional signal. Right, Circular representation of phase Source: [7].

As an alternative description in the case of a unit circle on the right in figure 3.22, the solid line shows the actual positive phase value greater than π. However the determined value is shown by the dotted line as we are working in the range of –π and π. So the 180 degree point in the unit circle where the phase changes abruptly from π to – π can be called phase transition points or phase wrap points. Many phase unwrapping algorithms have been developed to remove these phase transitions.

These algorithms [85] can be classified into three categories (1) Global algorithms, (2) Regional algorithms and (3) Path-following algorithms. Global algorithms are processed in terms of global functions. They are robust but very intense in terms of computation. Regional algorithms divide the image into regions and each region is processed individually. Then processed regions are phase shifted with respect to other regions to form larger regions until the whole image is unwrapped [86]. These algorithms provide a compromise between robustness and computation.

The path-following algorithms can be subdivided further into three categories (1) path-dependent methods [87], (2) residue-compensation methods [88], and (3) quality guided path methods [89]. Path-dependent methods detect position of edges or abrupt phase steps and use this information for phase correction. Residue-compensation methods search for residues in the image and generate branch cuts between positive and negative residues. Quality guided path algorithms unwrap the highest quality pixels with highest reliability values first and then proceed to the lower quality and lower reliability values to limit error propagation. A brief description of Itoh's method [90], Quality-Guided Path-Following algorithm ([91] Section 4.3) and Flynn's Minimum Discontinuity algorithm [92] ([91] Section 4.5) is written below by means of introduction.

3.5.2.1 Itoh's Method:

A concise algorithm was presented by Itoh in 1982 [90] for unwrapping phase measurements. Itoh described that the original phase values can be recovered by using a simple three step procedure of differentiating, wrapping and integrating. This is considered a basic technique for correcting the phase wrap transitions. Itoh describes a wrapping operator as Φ and differentiating operator as Δ. The wrapping operator Φ is defined as:

$$\Phi_l s(n) = s(n) + 2\pi k_l(n) \qquad (n = 0,1,\ldots\ldots\ldots,N), \qquad \text{Equation No: 3.30}$$

Where $s(n)$ is a sequence of complex numbers, l is a label and $k_l(n)$ is a sequence of integers which satisfies

$$-\pi \le \Phi_l s(n) < \pi \qquad (n = 0,1,\ldots\ldots\ldots..N) \qquad \text{Equation No: 3.31}$$

The differentiating operator Δ is defined by:

$$\Delta s(n) = s(n) - s(n-1) \qquad (n = 1,2,\ldots\ldots\ldots,N) \qquad \text{Equation No: 3.32}$$

From the definition of the wrapping operator Φ it can be shown that:

$$\sum_{n=1}^{m} \Phi_2 \Delta \Phi_1 s(n) = \sum_{n=1}^{m} \left[\Delta s(n) + 2\pi\left[\Delta k_1(n) + k_2(n)\right]\right] \qquad \text{Equation No: 3.33}$$

If $-\pi \le \Delta s(n) < \pi$, then $k_2(n)$ satisfies the equation

$$\Delta k_1(n) + k_2(n) = 0 \qquad \text{Equation No: 3.34}$$

Therefore for the given measured phase wrapped sequence $\Phi_1 s(n)$, unwrapped sequence can be recovered from this equation:

$$s(m) = s(0) + \sum_{n=1}^{m} \Phi_2 \Delta \Phi_1 s(n) \qquad \text{Equation No: 3.35}$$

Equation No 3.35 shows that the unwrapped signal *s (m)* can be recovered from the wrapped measured signal $\Phi_1 s(n)$ by simply taking the difference Δ, wrapping result (Φ_2) and finding the cumulative sum. This method works well so long as the condition $-\pi \leq \Delta s(n) < \pi$ is satisfied. But unfortunately in the presence of noise it is difficult to satisfy this condition. Itoh's method can be applied in 2D by applying the method to the rows and then columns or first columns and then rows. Itoh's algorithm forms the basis for other more sophisticated methods available in the literature which perform well with noisy data.

3.5.2.2 Quality-Guided Path-Following Algorithm:

In this algorithm, unwrapping in the integration path uses a quality map to unwrap the highest quality pixels first ([91] Section 4.3). The quality map consists of values that define the quality or goodness of each phase value derived from the variance of phase derivatives, maximum phase gradients or the magnitude images.

To begin with, the pixel with the highest quality value is selected and its four neighbors are examined. These neighbors are unwrapped and stored in a list called an adjoining list. The algorithm proceeds iteratively as: list pixel with highest quality, remove this pixel from list, its four neighbors are unwrapped and also placed in list. The listed pixels are sorted and stored in the order of their quality values. If the neighboring pixel has already been sorted then it is not placed in the list a second time. This process of removing the highest quality pixel from the list, unwrapping its four neighbors and inserting them in the list continues until all pixels have been unwrapped.

In figure 3.23 unwrapped pixels are shown in red color in (A) and neighboring pixels stored in adjoin list are shown in green color in (B). If the pixel in the third row and second column is selected and unwrapped, then the adjoin list is updated as shown in figure 3.23 (C). This algorithm is available in MRE/Wave software [51].

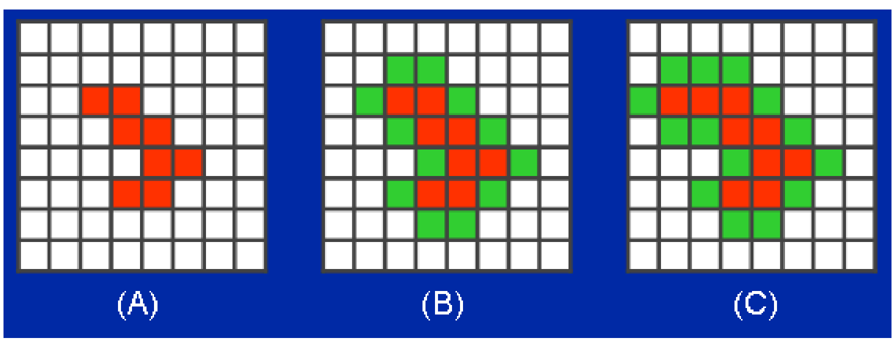

Figure 3.23: (A) Red color represent unwrapped pixel. (B) Adjoin list pixels represent in green color. (C) Third row and second column pixel in (B) is selected and unwrapped and adjoin list updated as shown. Source: [51].

3.5.2.3 Flynn's Minimum Discontinuity algorithm:

In Flynn's minimum discontinuity algorithm [92] phase wrap discontinuities create "fringe lines" that separate the image into regions separated by factors of 2π from each other. A Discontinuity is defined as pair of adjoining pixels when their magnitude difference is more than 2π. The Algorithm adds the appropriate multiple of 2π to the pixels enclosed in the region. The multiple added to a pixel depends on the number of fringe lines lay between pixel and reference pixel. This process is performed iteratively reducing discontinuities at each stage until no more loops are identified. At this stage data has been unwrapped and the resulting solution is a minimum discontinuity which means that remaining discontinuities are minimal ([91] Section 4.5). This algorithm is also available in MRE/Wave software [51].

3.5.3 Filtering MRE Data:

It is beneficial to filter the wave images to improve the inversion into shear modulus. Inversion techniques are sensitive to areas of low motion amplitudes produced due to the interference from reflections and refractions in an object. The local frequency estimation technique is even more prone to these types of problems [52].

In MRE/Wave software [51] six wave inversion filters are available to improve wave images. These filters are Gaussian (Low Pass, Band Pass and High Pass) and Butterworth (Low Pass, Band Pass and High Pass). Cut off frequencies are defined as waves per FOV referenced to the X axis.

Manduca at el [52] used the approach of spatio-temporal directional filtering to improve the inversion of MRE images. These filters are designed in frequency space to select the portions of the wave field propagating in a specific direction. These filters are a product of radial and spatially directional components and also oriented in time. First data is converted into 3D frequency space (two spatial directions and one temporal). The radial components are Butterworth band pass filters which are useful in removing high frequencies (noise) and low frequencies (bulk motion). The radial component is then multiplied with the spatial directional component and the result is applied to the temporal frequency plane. Best results can be achieved by applying the filter in the direction of the traveling wave. Directional filtering reduces the effects of interfering waves and produces smoother wave fields which are helpful in the inversion of MRE data to elasticity maps. Combining the shear modulus data, acquired by applying the directional filters in more than one direction yield additional improvement in the elasticity maps.

3.5.4 MRE Data Processing:

Different approaches can be used to invert the displacement (phase information) data to recover the elasticity values. These methods use some assumptions or simplifications and each of these methods have their own advantages and disadvantages.

3.5.4.1Equation of Motion:

Stress and strain are related to each other through a rank 4 tensor using thirty six independent quantities ([93] Section 8.3). In the case of an isotropic material, stress and strain are related by only a rank 2 tensor using two independent quantities called Lame constants, λ and μ, related to longitudinal and shear deformation. The relationship between stress and strain using tensor notation in an isotropic material is given by ([93] Section 8.5):

$$\sigma_{ij} = 2\mu e_{ij} + \lambda\delta_{ij}e_{nn}$$ Equation No: 3.36

Where e_{ij} is the second order symmetric strain tensor, σ_{ij} is the second order symmetric stress tensor and δ_{ij} is kronecker delta and is defined as [94]:

$$\delta_{ij} = \begin{cases} 1 if\ i = j \\ 0 if\ i \neq j \end{cases}$$ Equation No: 3.37

The strain tensor e_{ij} is defined in terms of the displacement tensor u_{ij} as [94][42]:

$$e_{ij} = (u_{i,j} + u_{j,i})/2$$ Equation No: 3.38

Where indices ‘,’ after represent differentiation. Substituting equation no 3.38 into equation no 3.36 results in:

$$\sigma_{ij} = 2\mu(u_{i,j} + u_{j,i})/2 + \lambda\delta_{ij}e_{nn}$$ Equation No: 3.39

$\lambda\delta_{ij}e_{nn}$ only exists when *i* = *j* otherwise its zero as value of kronecker delta is equal to 1 and $e_{nn} = u_{j,j}$.

$$\sigma_{ij} = \mu(u_{i,j} + u_{j,i}) + \lambda u_{j,j}$$ Equation No: 3.40

The translational equation of motion for a vibrating material is given as ([95] chapter 2 section C.1):

$$\sigma_{ij,j} = \rho\ddot{u}_i - F_i$$ Equation No: 3.41

Where ρ is the density, $\ddot{u}_i$ represent the second derivative of particle displacement with respect to time, and F_i is the body force vector associated with gravity and can be neglected as density is constant for small tissue displacement.

Vibration motion in terms of time harmonic displacement can be represented by a sine function [96] as in equation 3.42.

$$u_i = u_i \sin \omega t$$ Equation No: 3.42

Substituting Equation 3.40 and 3.42 into equation no 3.41. Equation for harmonic motion in isotropic medium is given as:

$$\left[\mu(u_{i,j} + u_{j,i}) + \lambda u_{j,j}\right]_{,i} = \rho \frac{\partial^2 u_i \sin \omega t}{\partial t^2}$$ Equation No: 3.43

$$\left[\lambda u_{j,j}\right]_{,i} + \left[\mu(u_{i,j} + u_{j,i})\right]_{,j} = -\rho \omega^2 u_i$$ Equation No: 3.44

Where ω is the angular frequency of mechanical motion. A knowledge of the displacement in all three directions is required to solve the above equation. If we assume that the medium is homogeneous, λ and μ are no longer a function of position, and then equation 3.44 becomes the algebraic matrix equation as written below:

$$\mu \nabla^2 u + (\lambda + \mu)\nabla(\nabla \cdot u) = -\rho \omega^2 u$$ Equation No: 3.45

Where ∇ is a vector differential operator. Longitudinal waves contribute less in the displacements so they are negligible and $\lambda(\nabla \cdot u) = 0$ which further simplifies equation 3.45 into a vector equation as:

$$\left[\nabla(\nabla \cdot u)\nabla^2 u\right]\mu = -\rho \omega^2 u$$ Equation No: 3.46

Assuming incompressibility $(\nabla \cdot u = 0)$ equation 3.46 then simplifies to a Helmholtz equation as:

$$\mu\nabla^2 u = -\rho\omega^2 u \qquad \text{Equation No: 3.47}$$

Where equation 3.47 measures μ with reference to a single sensitization direction.

3.5.4.2 Shear Modulus and mechanical frequency:

Lame constants are complex quantities where the imaginary part represents the attenuation for a viscoelastic medium. The damping term contains the time derivative of the strain ([95], Chapter 3 Section E). Rheological model are used to represent these values in terms of mechanical constants. In Figure 3.24 the Voigt model is shown where a spring and dashpot are placed parallel to each other to represent the viscoelastic medium [97].

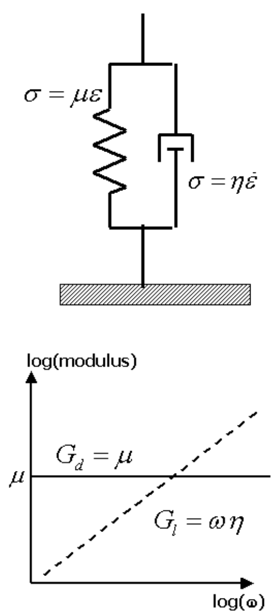

Figure 3.24: Voigt Model with spring and dashpot in parallel. Where G_d is the real part or dynamic modulus and G_l is the imaginary part or loss modulus. Source: [97].

So for harmonic motion: $\mu = \mu_r + i\mu_i = G_d + iG_l = c + i\omega\eta$. Where c is the spring constant or elastic stiffness and η is the dashpot constant or material viscosity. In the case of an isotropic, homogeneous, incompressible medium with no attenuation simple shear wave propagates with a spatial frequency f_{sp} the shear modulus is given as [42]:

$$\mu = \rho \frac{f_{mech}^2}{f_{sp}^2} = \rho v_s^2 \qquad \text{Equation No: 3.48}$$

Where f_{mech} is the mechanical driving frequency and v_s is the wave speed (phase velocity). It is often [65] assumed that $\rho = 1.0$ for soft tissues. In the case of attenuation, the wave speed and attenuation are functions of frequency. Catheline [98] computed the wave speed and attenuation using the Voigt model as written below:

$$v_s^2 = \frac{2(c^2 + \omega^2\eta^2)}{c + (c^2 + \omega^2\eta^2)^{1/2}} \qquad \text{Equation No: 3.49}$$

$$\alpha^2 = \frac{\omega^2}{2} \frac{(c^2 + \omega^2\eta^2)^{1/2} - c}{c^2 + \omega^2\eta^2} \qquad \text{Equation No: 3.50}$$

Where α is the attenuation by the factor $e^{-\alpha\kappa}$ in the direction of propagation κ. Attenuation can be expressed as attenuation per wavelength called the acoustic quality factor $Q = \frac{c}{\omega\eta}$ ([95], Chapter 3 page 92). The true shear modulus is the real part μ_r or *c,* so some techniques like LFE and phase gradient only measure wavelength and do not treat attenuation. Other techniques like AIDE calculate both μ_r and μ_i directly, and then can be used to calculate wave speed and attenuation using equations 3.49 and 3.50.

Different methods are available to calculate the shear modulus from displacement data and they are Local frequency estimation (LFE)[46][40], Phase gradient [99], Algebraic inversion of the differential equation (AIDE)[47], Variational method [100] and overlapping Subzone technique[49]. However I will be discussing only three mostly used.

3.5.4.3 Local Frequency(or Wavelength) Estimation:

Estimation of the local spatial frequency of the shear wave propagation pattern at each point in the image allows the calculation of the shear modulus across the image and from this information, elasticity maps can be generated. LFE estimates the local frequency of the shear wave propagation using algorithm introduced by Knutsson [46] and applied by Manduca [40].

The Knutsson algorithm estimates image frequencies by combining local estimates of instantaneous frequency over large numbers of logarithmic scales, derived from filters considered lognormal quadrature wavelets and product of radial and directional components. The radial component is a Gaussian on a logarithmic scale and of the form $R_i(\rho) = e^{-C_B \ln^2(\rho/\rho_i)}$, where C_B is the relative bandwidth and ρ_i is the central frequency. This above function is illustrated for six different central frequencies as shown in figure 3.25. The directional component has the form $D_k(\hat{u}) = (\hat{u}.n_k)^2$ if $(\hat{u}.n_k) > 0$ and $D_k(\hat{u}) = 0$ Otherwise, where n_k is the filter directing vector [101].

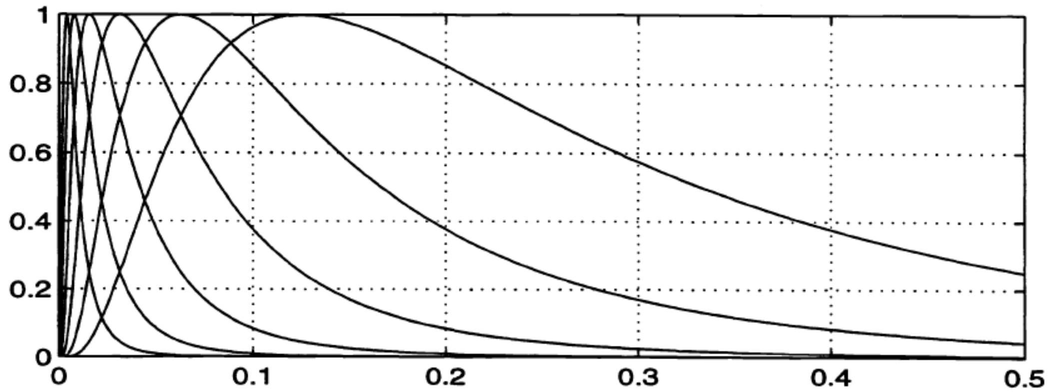

Figure 3.25: Filter profiles along the orientation direction for six fiters with central frequencies spaced an octave apart from 1/256 to 1/8.Bandwidth is $C_B = 1/(2\ln 2)$. Source:[101].

Summing the magnitudes of above two orthogonally oriented filters gives the estimate of signal strength that is local both spatially and in the frequency domain. Combining the output of two sets of above filters which differ only in central frequency produce a local frequency estimate. If filters have the appropriate bandwidth C_B relative to the ratio of two central frequencies then for the simple case local frequency estimate is the ratio of the two response times the geometric mean of the two central frequencies of two filters. If two central frequencies are spaced an octave apart then the correct bandwidth for each filter is $C_B = 1/(2\ln 2)$ as shown in figure 3.25.

The above estimate will work well only if the signal spectrum falls within the range of the filters. Otherwise estimates can be obtained using a bank of filters and performing weighted sums for different filter pairs where the weighting factor corresponds to the energy encountered by each filter. As an example, a test image with two regions of 4 and 8 cycles per image is shown in figure 3.26 (a) and local frequency estimate is shown in figure 3.26 (b). In figure 3.27, the top solid line is calculated with six filters spaced an octave apart and the top dashed line is calculated with 11 filters spaced half an octave apart. The bottom of figure 3.27 shows a vertical profile along the test image where the left half (Lower half of Image) has a frequency of 4 cycles and the right half (upper half of image) has frequency of 8 cycles across image.

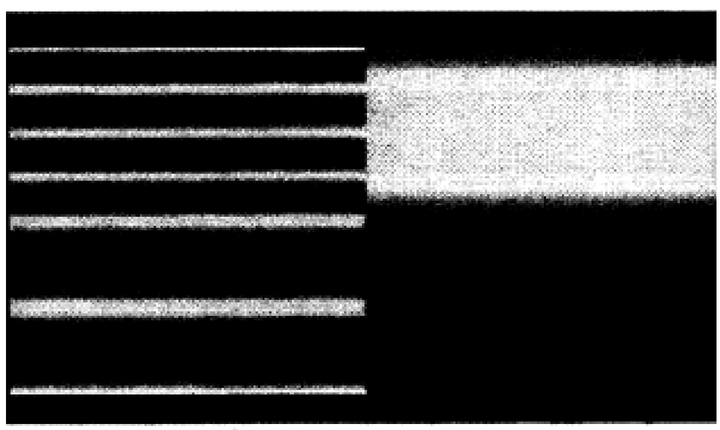

(a) (b)

Figure 3.26: (a) Test image with two regions of 4 and 8 cycles per image. (b) Local frequency estimate for Test Image. Source: [101].

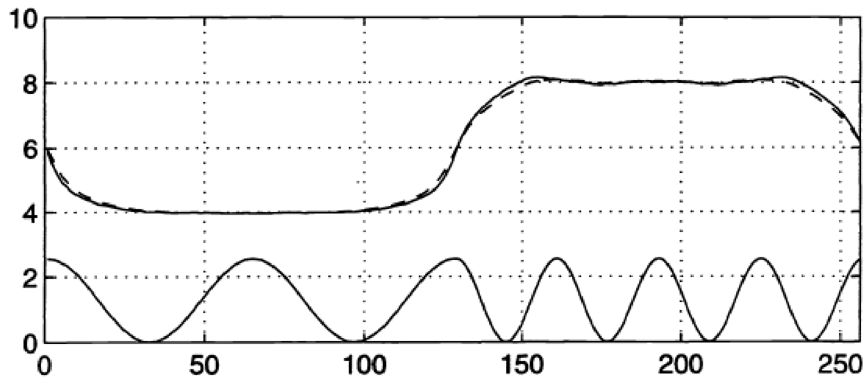

Figure 3.27: (a) Top solid line is calculated with six filters and dashed line is calculated with eleven filters. Bottom shows vertical profile along the test image. Source: [101].

From equation 3.48 $\mu = \frac{f_{mech}^2}{f_{sp}^2}$ with assumption that $\rho = 1.0$. LFE estimate μ from a single image displacement data acquired using single sensitization direction and single phase offsets. It can be extended to displacement data acquired from multiple phase offsets. The LFE is a robust and useful technique because of the sophisticated multi-scale data averaging. The disadvantage is the limited resolution at sharp boundaries however objects with different stiffness values can be clearly identified.

I will be using the MRE/Wave software [51] for reconstruction which is based on the LFE technique explained above. MRE/Wave will be discussed further in section 5.3.

3.5.4.4 Algebriac Inversion of the differential equation (AIDE):

This technique is developed by Oliphant [47] and is named algebraic inversion of the differential equation (AIDE). This technique involves the direct inversion of equation 3.45 to equation 3.47. These equations need to be solved for each pixel using data from local neighborhood to estimate local derivates. Full inversion of equation 3.45 estimates both μ and λ for an isotropic material and requires all components of motion. Including these components in equation 3.45 and rewriting it as:

$$A\begin{bmatrix}\lambda+\mu\\ \mu\end{bmatrix} = -\rho\omega^2\begin{bmatrix}u_1\\ u_2\\ u_3\end{bmatrix} \qquad \text{Equation No: 3.51}$$

Where $A = \begin{bmatrix}A_{11} & A_{12}\\ A_{21} & A_{22}\\ A_{31} & A_{32}\end{bmatrix} = \begin{bmatrix}u_{i,i1} & u_{1,ii}\\ u_{i,i2} & u_{2,ii}\\ u_{i,i3} & u_{3,ii}\end{bmatrix}$

Solving equation 3.51,

$$\begin{bmatrix}\lambda+\mu\\ \mu\end{bmatrix} = -\rho\omega^2(A^*A)^{-1}A^*\begin{bmatrix}u_1\\ u_2\\ u_3\end{bmatrix} \qquad \text{Equation No: 3.52}$$

Where A^* is conjugate transpose of matrix *A*. Assuming that the longitudinal pressure varies slowly so its derivative is negligible, then the inverted equation 3.52 is without the λ term. Also assuming an incompressible material provides incompressible AIDE or Helmholtz inversion which allows estimating the shear modulus from a single polarization of motion. The above equation is written as:

$$\mu = -\rho\omega^2 \frac{u_i}{\nabla^2 u_i}$$ Equation No: 3.53

Assuming $\rho = 1.0$ and that all the derivatives in the out of plane direction are negligible [48], the equation decouples and can be solved by 2D Helmholtz inversion from the out of plane shear motion component only.

3.5.4.5 Overlapping Subzone Technique:

Van Houten et al 1999 [49] presented a finite element based method to solve equation 3.44 which is still a differential equation. In this approach, a solution is iteratively refined on small overlapping subzones of the overall domain. The solution of this subzone is updated based on the difference between the forward calculation of displacement and the measured values. Once the update on this subzone is finished, the subzone with greatest residual error is determined and updated. In 2001 Van houten [50] applied this technique on 3D data and achieved promising results. However attenuation needs to be treated and calculation times in 3D are still an issue.

3.6 Clinical Applications of MRE:

Elastic properties of tissues provide information about their state of health. As mentioned in the introduction, the century's old technique of palpation is still used as a clinical tool for detecting cancer and other diseases in accessible regions of body. However small and inaccessible lesions are not possible to detect with palpation.

Palpation assesses the physical property called elastic modulus as it resists deformation. Magnetic Resonance elastography (MRE) calculates the elastic modulus of tissues and reconstructs elasticity maps. Different investigators have used this technique to image the elastic properties of biomaterials, engineered tissue constructs, tissue specimens and organs (mice and humans).

MRE has already been applied to brain, breast, muscles, thyroid, heart, lung, liver and spleen, and has proved particularly successful in diagnosing liver diseases. Different clinical areas have their own challenges, so the MRE method and reconstruction varies by clinical area. The excitation frequency also varies depending upon the tissues and their location. For example in abdomen frequencies between 40 and 200Hz are common[8], in brain 100Hz [12], in breast frequencies between 75 and 300Hz [15] are used, in the lung 150Hz [20], in muscles 90 to 150Hz [21], in prostate 65Hz [23] and in thyroid 80 to 100 Hz [24] are typically used. A brief description of clinical application of MRE in different areas is discussed below.

3.6.1 Abdomen

Meng [8] applied MRE to different organs of the abdomen (liver, kidney, spleen and pancreas) and found that MRE is very helpful in identifying abdominal diseases like hepatic fibrosis and portal hypertension. Early detection of liver fibrosis is very important for treatment of chronic hepatitis. Figure 3.28 shows the MRI 3-D image, the displacement data acquired in three encoding directions X, Y and Z and lastly the elastogram reconstructed from this data. The elastogram clearly shows elastic regions in different organs of abdomen.

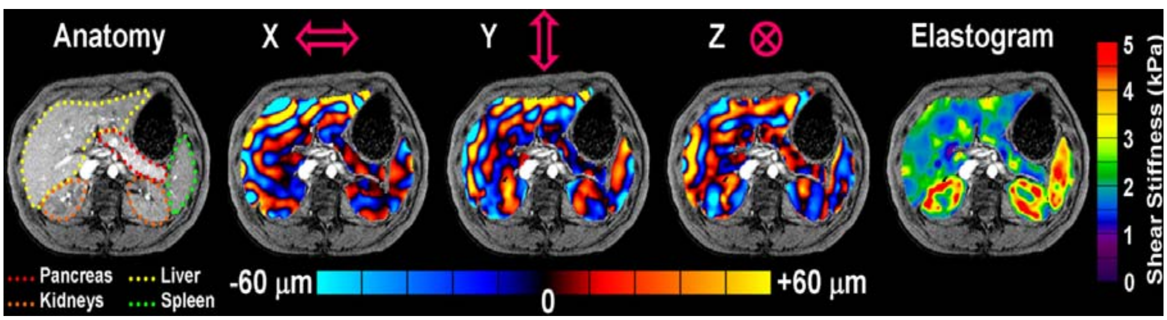

Figure 3.28: Slice from 3-D/3-axis abdominal MRE of healthy volunteer. Source: [8].

Talwalker [9] performed MRE on spleen and liver and found a correlation between the liver stiffness and spleen stiffness ($r^2 = 0.75$). This indicates that the mean spleen stiffness is higher in patients with liver fibrosis compared to healthy volunteers. It is helpful in predicting the presence of esophageal varices in patients diagnosed with advanced hepatic fibrosis.

Sack and his group used multi-frequency MRE [10] to assess the liver viscoelastic properties and showed that it can clearly differentiate between normal and cirrhotic liver.

Another group led by Sinkus presented a paper in 2008 [11] and compared MRE, Ultrasound Elastography and APRI (Aspartate aminotransferase to Platelets Ratio Index) for the measurement of liver fibrosis. APRI is performed on liver samples acquired during liver biopsy of 146 patients with liver fibrosis. MRE and Ultrasound elastrography measurements were performed on liver in these patients. Patients with high APRI value shows higher elasticity values and supports the liver fibrosis results obtained with APRI. MRE can be used as diagnostic tool for liver fibrosis.

3.6.2 Brain

Ehman and his group [12] in 2007 performed brain MRE on 25 healthy volunteers and showed that it is possible to measure the shear stiffness of intracranial tissues. Results indicate that cerebral white matter is significantly stiffer than white matter. In figure 3.29, (a) is the anatomical image, (b) shows wave propagation, (c) is the shear stiffness map and (d) is the shear map overlaid on anatomical image for two healthy volunteers.

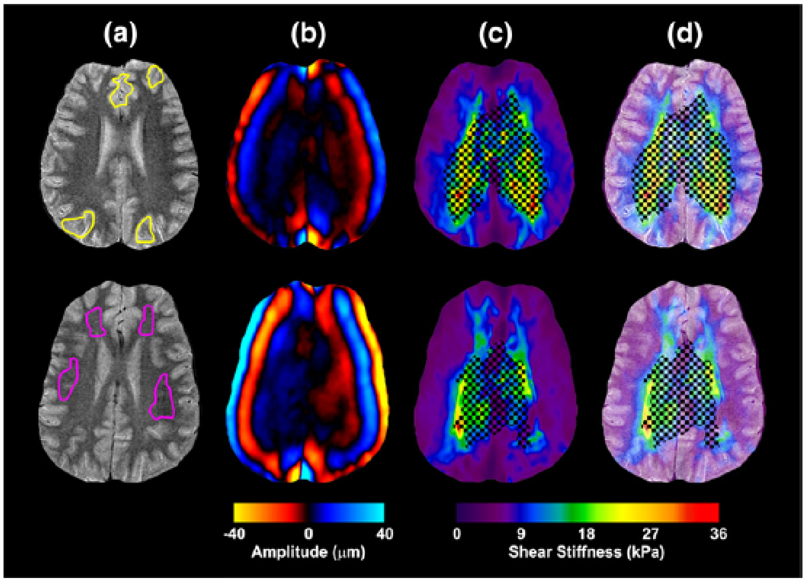

Figure 3.29: MRE results from two different volunteers. Source: [12].

Sack presented a paper [13] demonstrating that viscoelastic properties of the brain measured using MRE can be used to diagnose diffuse cerebral diseases such as dementia and Alzheimer's disease. This group also used MRE [14] to study the impact of age and gender on brain viscoelasticity and demonstrated that elastic properties change with age.

3.6.3 Breast

Studies have shown that MRE is a useful tool in diagnosing breast diseases such as cancer. Mcknight in 2002 [15] presented some preliminary breast MRE results. Figure 3.30 shows MRI of a 43 year old woman with invasive ductal breast carcinoma in the lateral breast on the left and the MRE elasticity map on the right. This image shows a high stiffness in the same region.

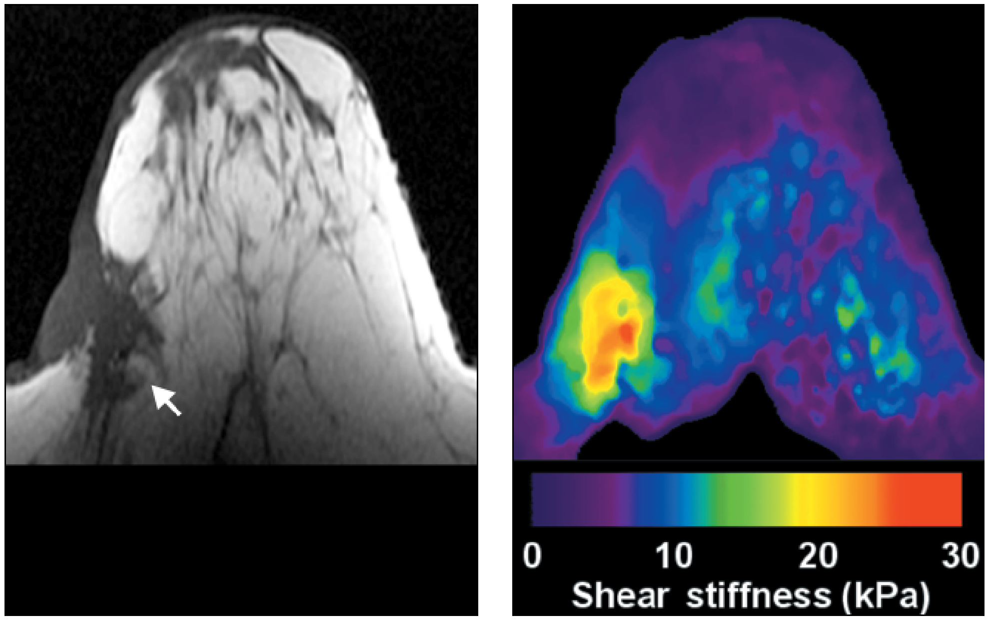

Figure 3.30: T1 weighted MR Image of breast and MRE elastogram of 43 year old women. Source: [15].

This study concluded that it is possible to measure the mechanical properties of normal breast tissues and breast malignancies.

In 2005 Sinkus and his group [16] showed that benign and malignant lesions can be separated on the basis of their shear modulus. In 2009 the same group [17] compared MRE with Contrast Enhanced MRI and showed that MRE supports the results of Contrast Enhanced MRI.

3.6.4 Cardiac

Thomas in 2008 [18] presented a paper where he shows that pressure-related heart functions can be determined by measuring the shear modulus variations in the LV wall. It is considered to be the first mechanical test of the heart functionality with MRE which could be helpful in diagnosing different heart diseases such as diastolic dysfunction.

3.6.5 Hyaline Cartilage

Hyaline cartilage is found in vertebrates and also in the fetal skeleton. Lopez in 2007 [19] performed high frequency(1000 to 10,000 Hz) MRE on hyaline cartilage with a Custom made actuator and Z-axis gradient coil. MRE was capable of calculating shear stiffness values for hyaline cartilage which was a few millimeters thick with a high stiffness. Figure 3.31 shows four phase offsets of the propagating waves in 5mm bovine hyaline cartilage at 5000 Hz. Images show that almost one quarter of the shear wave is propagating through the 5mm sample.

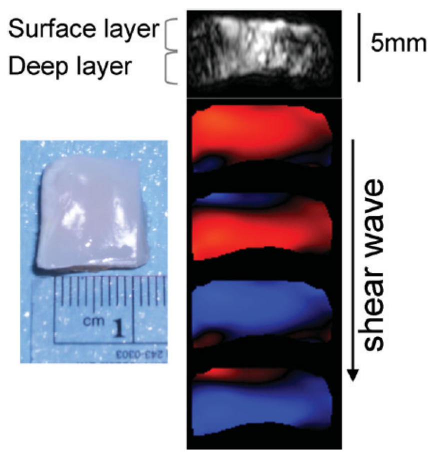

Figure 3.31: Wave images of bovine hyaline cartilage at 5000 Hz. Source: [19].

3.6.6 Lungs

Goss in 2006 [20] conducted a study to look into the technical feasibility of lung MRE. The driven longitudinal waves near lung converted into shear waves when they reached the lungs because of the mode conversion at the pleural surface. Figure 3.32 shows the magnitude image on right and the shear wave propagation on the left. The yellow line indicates the location of the driver. This study provides preliminary feasibility evidence for lung MRE.

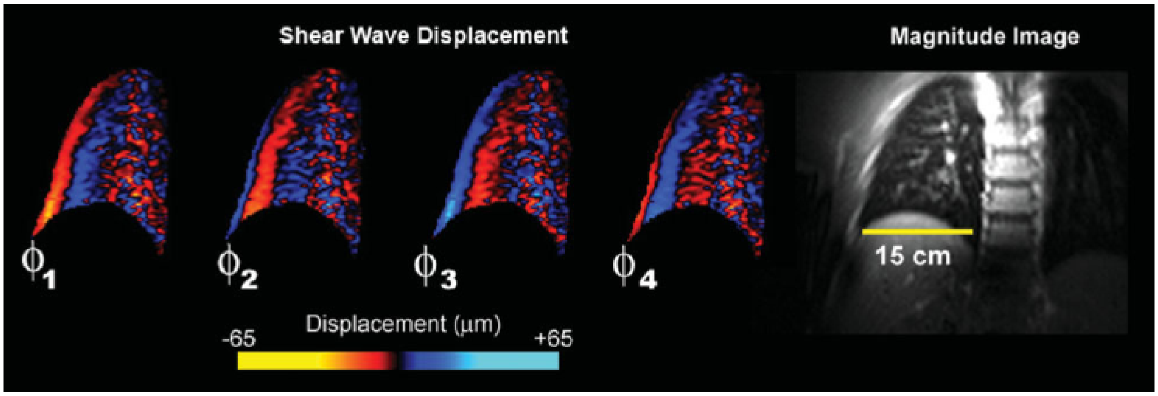

Figure 3.32: Coronal Phase contrast images from healthy volunteer. Source: [20].

3.6.7 Muscles

It is possible to study the elastic properties of muscles with MRE, however advanced inversion algorithms are required to consider the anisotropic behavior of muscles in two or three dimensions. Ringleb in 2007 [21] conducted an MRE study on healthy and pathological Skeletal muscles. They were able to differentiate between them on the basis of MRE results. Figure 3.33, (a) shows a magnitude image of the upper trapezius and (b) is the displacement image.

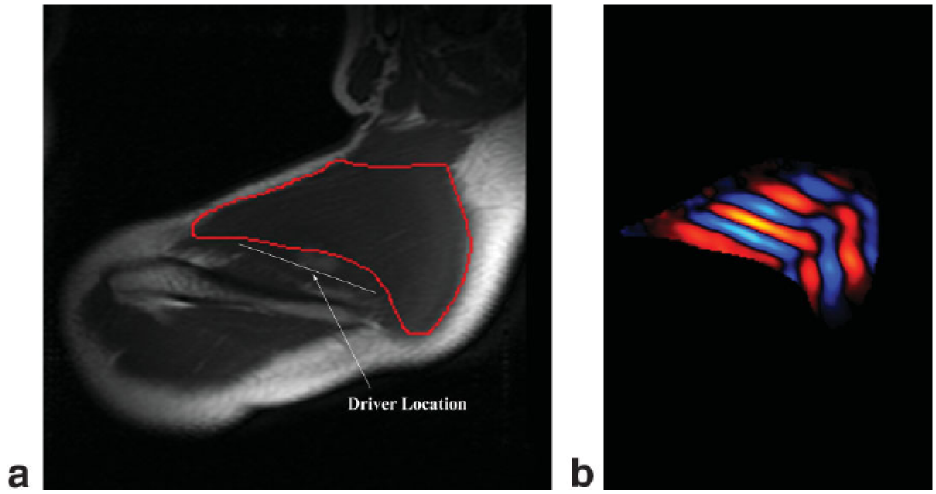

Figure 3.33: (a) Magnitude image of upper trapezius with driver location and (b) shows propagating strain waves. Source: [21].

Myofascial pain is caused by the Taut bands. Taut bands are contracted or shortened muscle fibers. Palpation is clinically the only way to detect their location as there is currently no laboratory or imaging technique available to detect the nature and location of these bands. Chen in 2008 [22] explored the possibility of detecting these bands using MRE and confirmed their existence in direct comparison with palpation.

3.6.8 Prostate

It is difficult to induce mechanical motion in prostate glands. However Kemper in 2004 [23] used a modified vibrator and achieved a sufficient penetration of mechanical waves into prostate glands. Results acquired with this study show that it is possible to measure the elastic parameters of prostate glands with MRE. Elasticity of the central portion of the gland is lower than the peripheral portion as shown in figure 3.34.

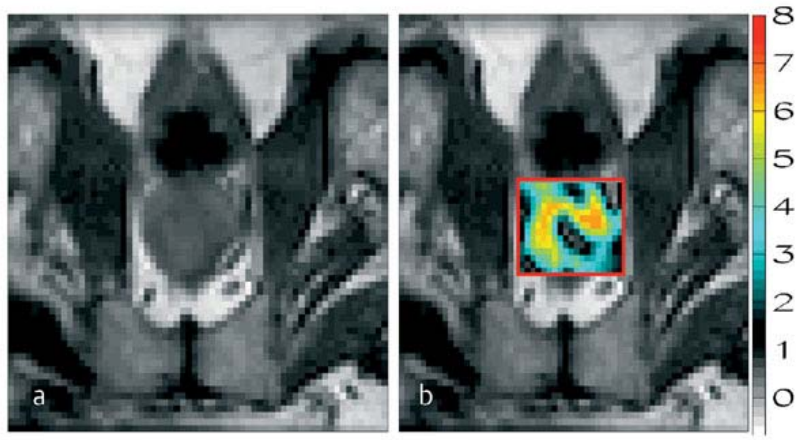

Figure 3.34: (a) Magnitude image depicting prostate gland and (b) Elasticity distribution (kPa) within prostate gland. Source: [23].

3.6.9 Thyroid Glands

MRE can be used to differentiate between normal and HT (Hashimoto's Thyroiditis) thyroid glands [24] but to prove the clinical utility requires further research. Figure 3.35 images (a) and (b) are the elasticity maps of normal gland and (c) and (d) are of HT gland, (e) and (f) are MRI images of normal and (g) and (h) are of HT gland.

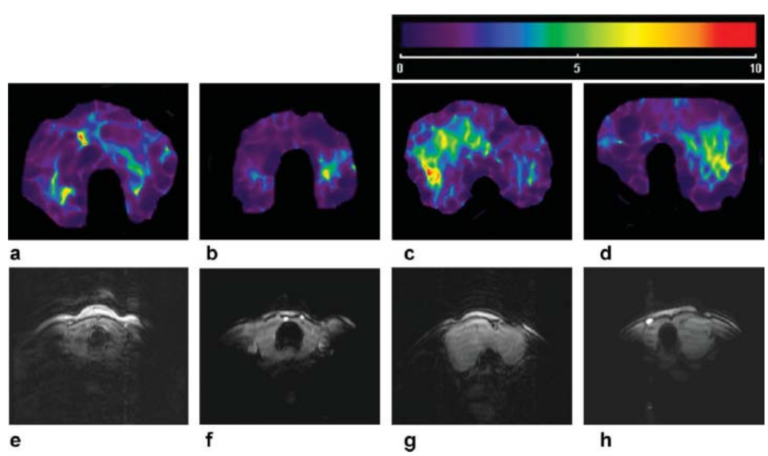

Figure 3.35: Elasticity map and magnitude image of healthy and HT Gland. Source: [24].

3.6.10 Heel fat Pads

Weaver in 2005 [25] performed MRE and calculated the shear modulus of the soft tissues in heel fat pads. Apparatus shown in figure 3.36 (a) is used to induce the vibrations in this small area. Shear modulus images with heel under high and low pressure is shown in figure 3.36 (b). Results show that MRE could play a significant role in studying the weight bearing functions of heel fat pads.

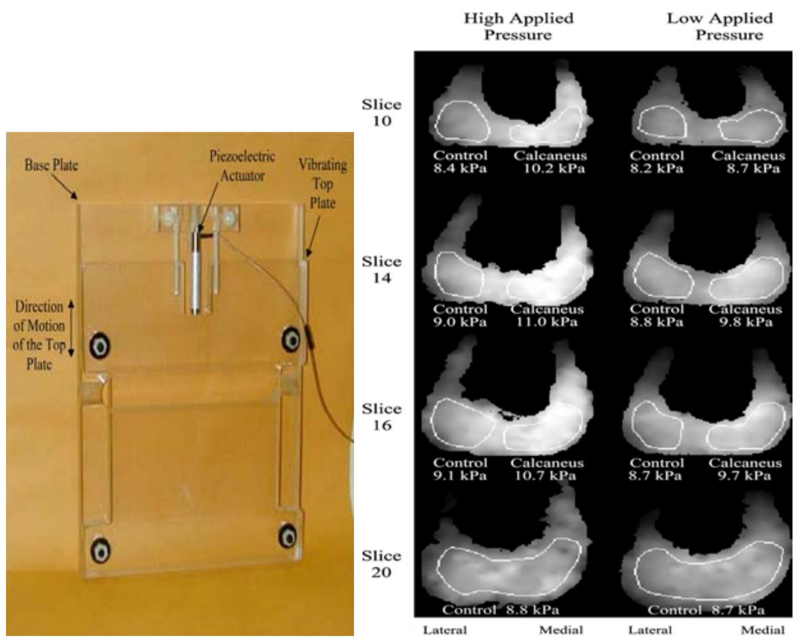

(a) (b)

Figure 3.36: (a) Apparatus used to vibrate the heel fat pads where top plate is vibrating with the help of actuator and (b) Shear modulus images of heel fat pad under high and low pressure. Source: [25].

In this chapter MRE theory has been discussed in detail. Brief detail about the vibration actuator, MRE sequence and reconstruction software is also included.

Clinical applications of MRE have also been discussed. In next chapter 4 hardware design and pulse sequence programming will be discussed.

Chapter 4

Materials and Method

4.1 MRI Scanner :

All experiments were performed on the Research Magnetic Resonance (MR) Scanner located at St. Joseph's Healthcare in London Ontario. This system is a Siemens (Erlangen, Germany) Magnetom Verio 3T, A Tim system. This MR has a maximum gradient strength of 45mT/m @ 200mT/m/s which is the strongest in the market [102]. Syngo is a Siemens cross modality user interface running on top of Windows and is capable of running different applications very efficiently. SyngoMR is the MR implementation of this software and is also called Numeris 4. The current version on the system is syngoMR VB17.

4.2 Vibration actuator:

As has already been mentioned, the vibration actuator is the device used to induce motion in the scanning region. Used in these experiments is a custom made Type II actuator which has the electromagnetic coil mounted on the actuator. The interaction between the actuator coil and the main magnetic field is used to generate the oscillatory motion.

4.2.1 Actuator Design:

The actuator was made from ¼ inch Plexiglas. Plexiglas is a MRI compatible material and strong enough to withstand the movement of the coil. Sheets were pre-cut in different sizes and joined together with trichloromethane. The base plate was 10 inches long and 5 inches wide as shown in figure 4.1. Four rubber bumpers were attached for better grip to surfaces.

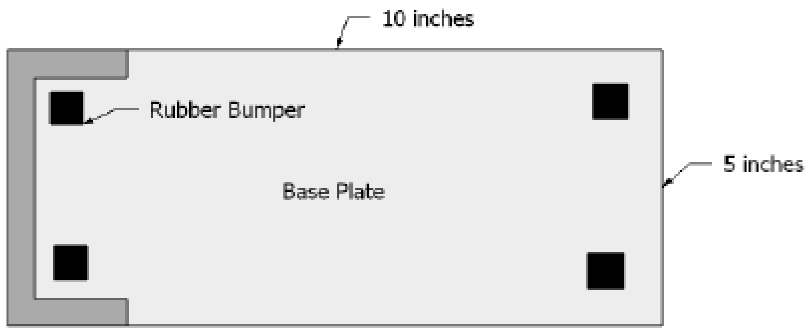

Figure 4.1: Base Plate for the actuator.

One plate was cut (6.5 inch long and 5 inches wide) to mount the lever on top. It was joined by two side plates (6.5 inch X 1.25 inch) to add vertical height for the moving lever as shown in figure 4.2.

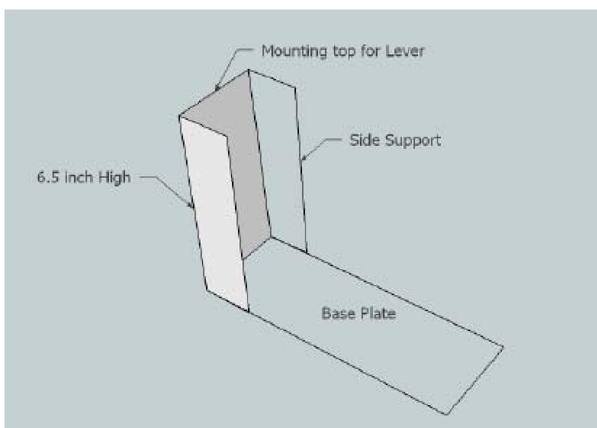

Figure 4.2: Vertical height for actuator.

The top was made of two plates joined together with two spacers on either side leaving a space in between for the moving lever. A hole in the middle of both plates held the lever and was the pivoting point for the lever as shown in figure 4.3. A pivoting pin held the lever in place.

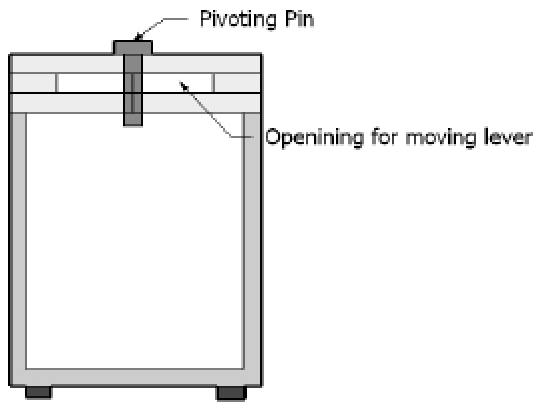

Figure 4.3: Lever holding mechanism for actuator.

The moving lever was 11 inches long and 1.5 inches wide, made from the same Plexiglas sheet. The electromagnetic coil was set on the opposite side of the lever from the 2 X 2 inch moving head as shown in figure 4.4.

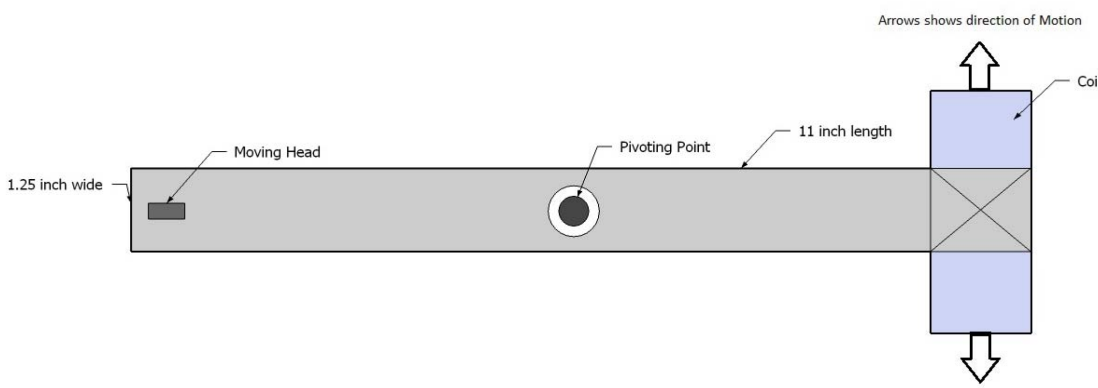

Figure 4.4: Moving Lever of actuator.

The electromagnetic coil was mounted on the empty side with cable ties, and an assembled view of the actuator is shown in figure 4.5.

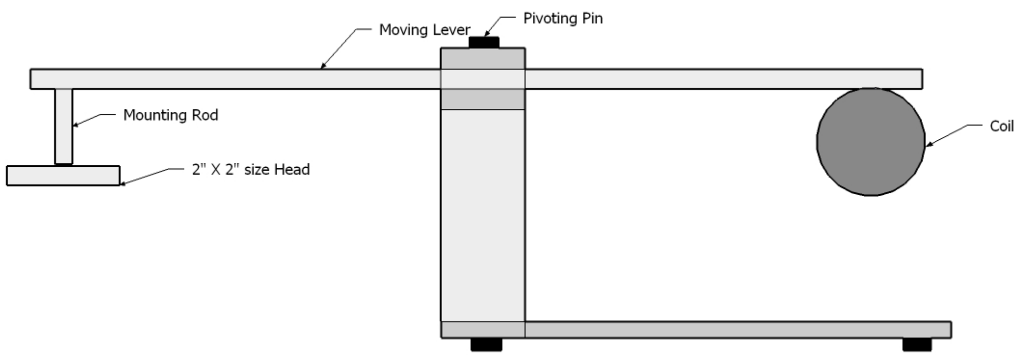

Figure 4.5: Actuator assembly.

4.2.2 Coil Design:

The core of the electromagnetic coil was made from 5 inch long hollow plastic pipe of external diameter 1.5 inches. Number 8079 copper wire [103] made by Belden Inc (Richmond Indianapolis) was used to wind the coil. The wire was rated AWG 26 with a polyester insulated coating. 250 turns were wound by hand onto the core with the ends exposed to connect the supply voltage. Insulating electrical tape was used to fasten the wires. Figure 4.6 shows the coil mounted on the actuator.

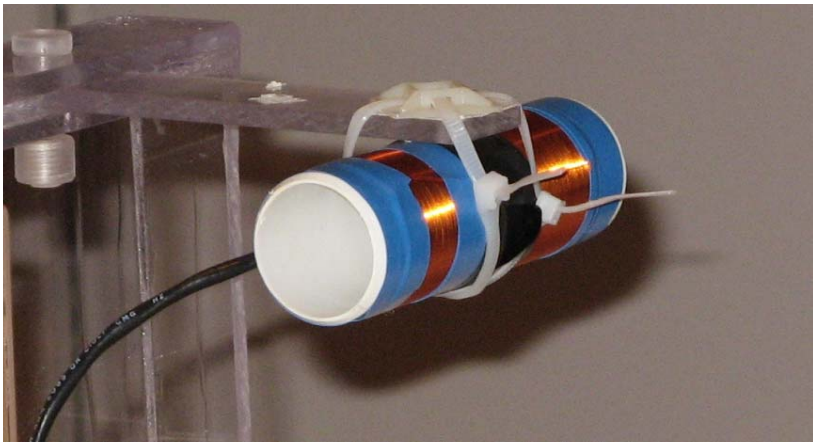

Figure 4.6: Electromagnetic coil mounted on the actuator Lever.

The magnetic field produced by this solenoid coil would be similar to that depicted in figure 4.7 and can be calculated [104] using Ampere's law from the equation below:

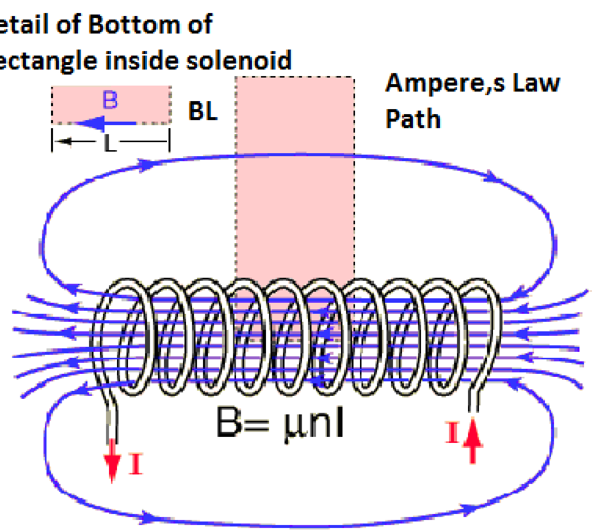

Figure 4.7: Source [104]

$$B = \mu n I$$ Equation no 4.1

Where,

- B is the Magnetic field produced in coil
- μ is the permeability = $k\mu_\circ$, k is equal to 1 for air and $\mu_\circ = 4\pi x 10^{-7}$ T/amp-m.
- n is the turn density = $\frac{N}{L}$, *N* is the total no of turns and *L* is the length of coil in meters
- I is the current in the coil.

Using equation no 4.1, the magnetic field produced by the coil at 100mA (used for 125 Hz frequency) would be 2.47G. A current of 200mA was used for the 250Hz frequency, which would result in a field of 4.94G. This magnetic field interacts with the main magnet magnetic field and creates the vibration within the lever arm. These vibrations are transferred to the phantom through the lever head. The magnetic dipole moment of a circular coil is given by equation no 4.2 and the torque on a circular coil in the presence of perpendicular magnetic field is given by equation no 4.3 [105].

$$\mu = NIA$$ Equation No 4.2

$$\tau = \mu X B$$ Equation No 4.3

Where,

- N is the number of turns.
- I is the current in the coil.
- A is the area of circular coil.
- B is the main magnetic field.

Using equation no 4.2 and 4.3 the torque exerted on the coil in the presence of a 3T main magnetic field would be .085N-m at 100mA and 0.17N-m at 200mA.

4.2.3 Signal Generator:

A 20 Mhz log-linear sweep generator model F-77 (Interstate Electronics, Anaheim CA USA) was used to induce the sine wave signal in the magnetic coil which in turn created a varying magnetic field. This study used a 250 Hz and 125

Hz sine wave signal with a voltage level of 15V peak-to-peak (p-p). A triggering signal was used from the MRI to start the signal generator in gated mode. The trigger signal was a Transistor-Transistor Logic (TTL) signal coming from the triggering device which will be discussed later.

Figure 4.8: Interstate F-77 signal generator.

4.2.4 Power Amplifier:

The actuator coil has an impedance of 5.2 Ohms whereas the signal generator output impedance is 50 Ohms. The maximum power from the generator can only be delivered if these two impedances are matched. A power amplifier was used for this purpose and also helped to control the current in the coil. The 900 series amplifier model: A-901A (TOA Corporation, Japan) as shown in figure 4.9 was used. The signal generator output is connected to the program input RCA (Radio

Corporation of America) connector at the back of amplifier as shown in figure 4.10 and the output power is controlled by the program power knob in the front.

Figure 4.9: 900 series power amplifier.

The coil was connected between the common and 8 Ohm connectors as shown in figure 4.10. Input and output voltage magnitude and phase were confirmed by an oscilloscope. A multi-meter was used to confirm the current delivered to the coil circuit.

Figure 4.10: Input and Output connectors of Power Amplifier.

4.2.5 Triggering device:

The Siemens fMRI trigger converter and optical cable shown in figure 4.11 were used to convert the optical signal from the MRI into TTL levels.

Figure 4.11: Siemens fMRI Trigger and Optical Cable

The optical cable was connected to the U4 connector on the LWL_INT board present in the computer cabinet of the MRI to the trigger converter. Standard coaxial cable was used to connect the output of the trigger converter to the signal generator TRIG-SYNC-IN. Proper jumper setting was required inside the Siemens fMRI trigger box to set the toggle mode which gives the high TTL signal as long as the optical signal is true (ON) and low TTL signal for the False (Off) optical signal. Trigger timing was controlled by the sequence depending on the number of the motion cycles needed for MRE.

4.3 Pulse Sequence programming:

A standard Gradient Echo sequence was modified to include MEGs on all three axes. These gradients must be synchronized with the motion. In this test only a single direction of motion was selected by only turning on MEGs on a single axis. The Siemens IDEA programming environment was used to make these changes.

4.3.1 IDEA Environment:

IDEA, or Integrated Development Environment for Applications, is a tool to develop and Test MRI pulse sequences and image reconstruction programs for Siemens MRI. Different tools for VB17 are available to develop and test the pulse sequences before loading them onto the scanner. The IDEA user interface is a shell like command window. The most commonly used tool is POET (Protocol Offline Editing Tool) which helps to review and track the protocol parameters and simulating sequence timing and event diagrams.

4.3.2 Modification of GE sequence:

The following are the changes required to convert the standard GE sequence into the MRE sequence.

1. The sequence was modified to allow input of the MRE parameters.
2. The MEG was programmed to occur after the application of the RF pulse in the Gray shaded area shown in the timing diagram of the GE sequence

(Figure 4.12). *It was important to ensure that the MEG did not overlap with any other gradients*.

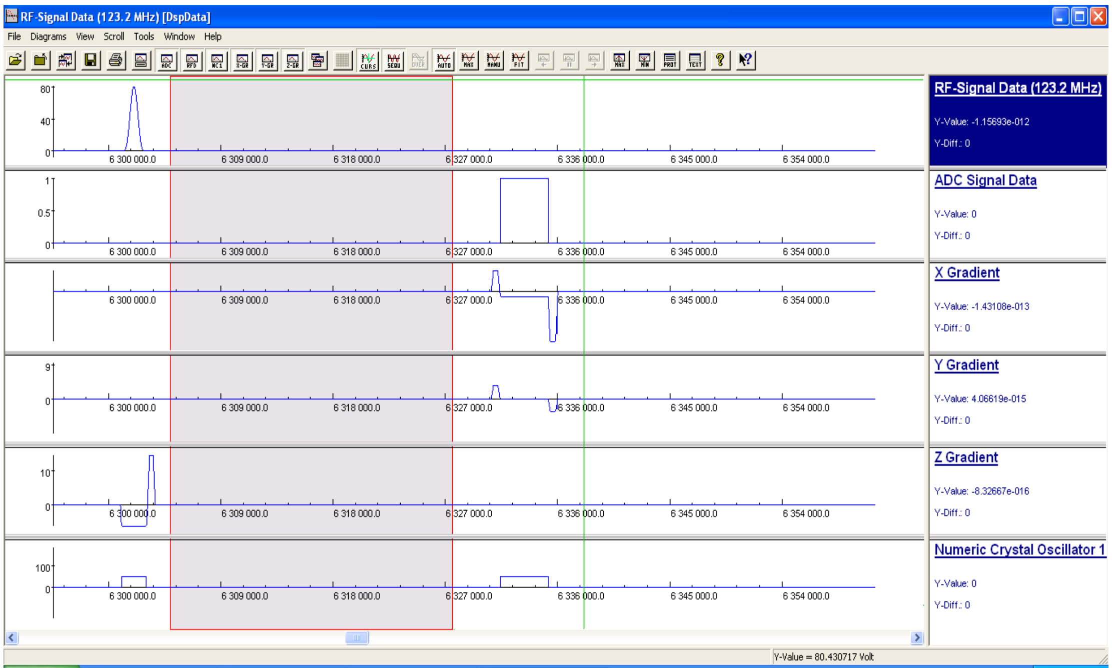

Figure: 4.12: Gradient Echo sequence timing diagram acquired using POET.

3. A trigger signal was generated in software that was active (ON) during the motion for the purpose of motion synchronization with the MEG.

4.3.3 Programming Procedure:

Changes made to the standard GE sequence are described below:

1. A special card was created in the sequence tab to include the parameters needed for MRE as shown in figure 4.13. The function of each parameter is explained below:

- “MEG” turns the motion encoding gradients on and off. Default is MEG ON.
- “MEG FREQUENCY” is to select the MEG frequency and there are four choices 250Hz, 200Hz, 125Hz and 100Hz.
- “MEG PHASE” selects the MEG Polarity. “Pos” selects the Positive polarity and “Neg” selects the negative polarity. Default is “Pos”.
- “MEG Cycles” selects the no of MEG cycles. Value ranges from 1-4. Default is 4 cycles.
- “pre-MEG STIM” are the no of motion cycles before MEG start. Options are 1 and 2. Default is 2 so there are two cycles of motion before the MEG starts.
- “MEG Delay” is the time delay in degrees between motion cycles and MEG Cycles. Values are 0, 45, 90 and 135. This parameter is used to create different offsets to capture motion at different intervals.
- “MEG Amplitude” is the amplitude of Motion encoding gradients in mT/m and can be varied from 0 to 10. Default value is 10.
- “RO MEG” is to turn on and off the MEG on read out axis. Default is “ON”.
- “PE MEG” is to turn on and off the MEG on Phase encode axis. Default is “OFF”.
- “SS MEG” is to turn on and off the MEG on slice select axis. Default is “OFF”.

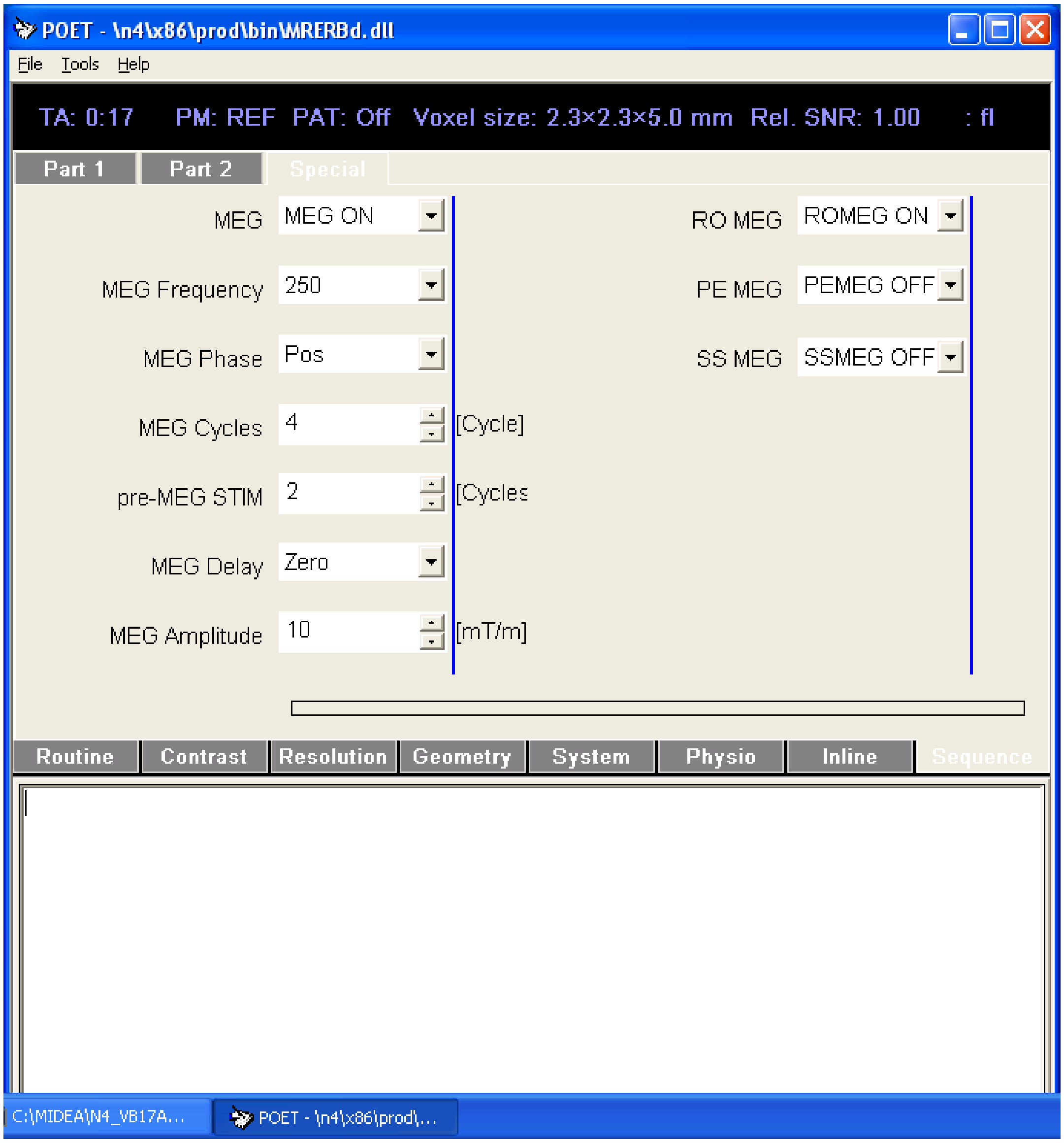

Figure 4.13: MRE parameters in sequence special card in POET.

2. The timing of the external trigger was defined by calculating the time from the MRE period and multiplying by the Total no of cycles (MEG Cycles + pre-MEG STIM).

3. The duration and amplitude of the Read out, Phase encode and slice select pulses were determined based on the MRE parameters selected in the sequence special card.
4. The start time of MEG was calculated depending on the parameters selected.
5. The pulses were added in the real time depending upon the no of cycles set in the parameters.
6. The program was modified so that the Value of TE and TR changes depending upon the frequency and no of cycles to accommodate the extra pulses without overlap.

Figure 4.14 shows the timing diagram of MRE sequence where four MEG pulses are added on all three axis that do not overlap any of the other existing pulses.

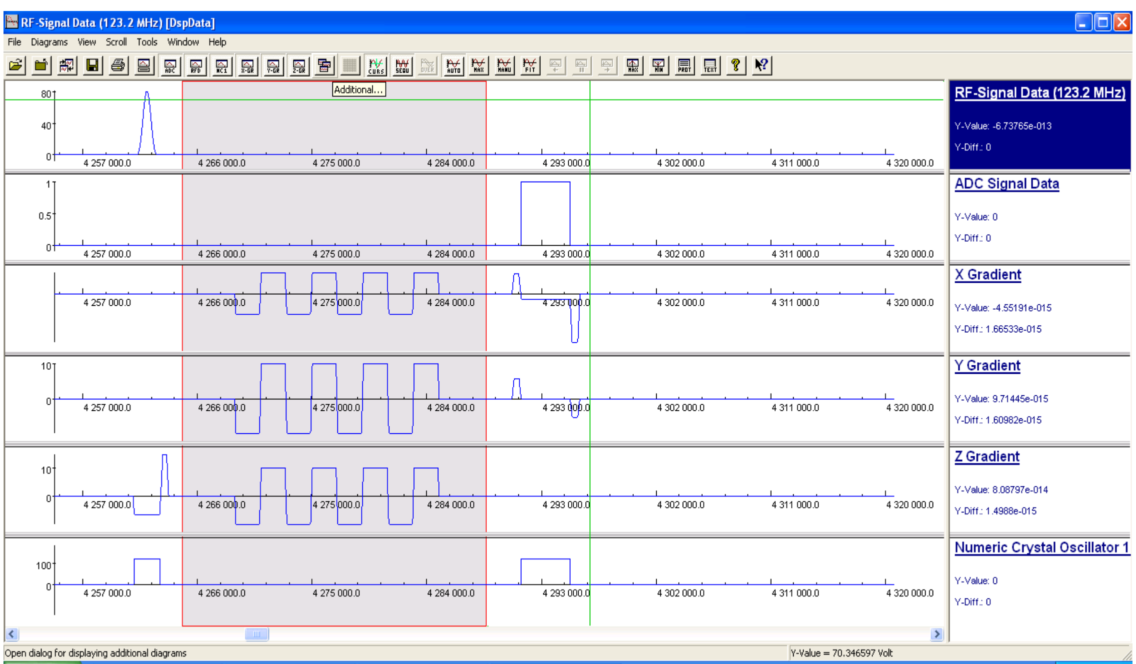

Figure 4.14: MRE Pulse sequence timing diagram captured using POET.

The event block in figure 4.15 shows the timing and duration for the entire gradient and RF pulse set.

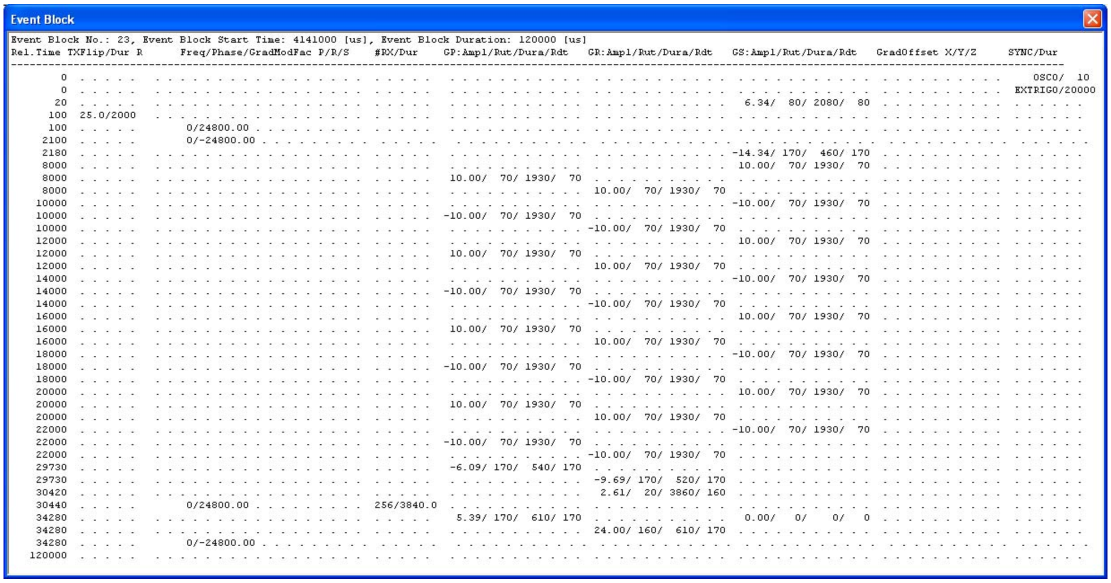

Event Block

Event Block No.: 23, Event Block Start Time: 4141000 [us], Event Block Duration: 120000 [us]

Rel.Time	TXFlip/Dur R	Freq/Phase/GradModFac P/R/S	#RX/Dur	GP:Ampl/Rut/Dura/Rdt	GR:Ampl/Rut/Dura/Rdt	GS:Ampl/Rut/Dura/Rdt	GradOffset X/Y/Z	SYNC/Dur
0								OSC0/ 10
0								EXTRIG0/20000
20						6.34/ 80/ 2080/ 80		
100	25.0/2000							
100		0/24800.00						
2100		0/-24800.00						
2180						-14.34/ 170/ 460/ 170		
8000						10.00/ 70/ 1930/ 70		
8000				10.00/ 70/ 1930/ 70				
8000					10.00/ 70/ 1930/ 70			
10000						-10.00/ 70/ 1930/ 70		
10000				-10.00/ 70/ 1930/ 70				
10000					-10.00/ 70/ 1930/ 70			
12000						10.00/ 70/ 1930/ 70		
12000				10.00/ 70/ 1930/ 70				
12000					10.00/ 70/ 1930/ 70			
14000						-10.00/ 70/ 1930/ 70		
14000				-10.00/ 70/ 1930/ 70				
14000					-10.00/ 70/ 1930/ 70			
16000						10.00/ 70/ 1930/ 70		
16000				10.00/ 70/ 1930/ 70				
16000					10.00/ 70/ 1930/ 70			
18000						-10.00/ 70/ 1930/ 70		
18000				-10.00/ 70/ 1930/ 70				
18000					-10.00/ 70/ 1930/ 70			
20000						10.00/ 70/ 1930/ 70		
20000				10.00/ 70/ 1930/ 70				
20000					10.00/ 70/ 1930/ 70			
22000						-10.00/ 70/ 1930/ 70		
22000				-10.00/ 70/ 1930/ 70				
22000					-10.00/ 70/ 1930/ 70			
29730				-6.09/ 170/ 540/ 170				
29730					-9.69/ 170/ 520/ 170			
30420					2.61/ 20/ 3860/ 160			
30440		0/24800.00	256/3840.0					
34280				5.39/ 170/ 610/ 170		0.00/ 0/ 0/ 0		
34280					24.00/ 160/ 610/ 170			
34280		0/-24800.00						
120000								

Figure 4.15: MRE Sequence Event Block diagram.

4.4 MRE Phantom:

The phantom was made from Agar gel. A 10cm X 10cm Plexiglas container was made to hold the gel. Purified granulated agar [106] (EMD Chemicals, Gibbstown USA) was dissolved in water to make gels of 1%, 2%, and 3% (Weight by Volume) with different elasticities. Two one inch diameter cylinders of 1% and 3% concentrations were made. The background of the phantom was made with 2% agar, and the cylinders were placed near the middle of the phantom as shown in figure 4.16. The actual stiffness of similar gels is 6KPa for 1%, 22KPa for 2% and 80KPa for 3%, as mentioned by Glaser [107].

Figure 4.16: 2% Agar Gel Phantom with cylindrical inserts of 1% and 3%.

4.5 Equipment Setup:

The phantom was placed under the moving head in such a way that the moving head touches the top part of gel as shown in figure 4.17. The entire assembly was placed on the patient couch of the MRI.

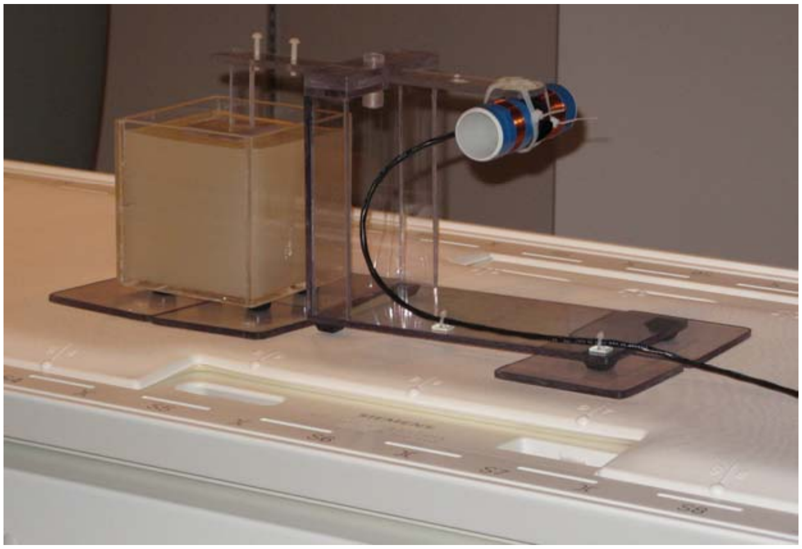

Figure: 4.17: Actuator and phantom setup on couch.

The actuator cables were passed through the waveguide MRI RF cage and connected to the common (COM) and 8 ohm terminal located on the back of power amplifier.

A block diagram of the equipment setup is shown in figure 4.18 and an actual picture is shown in figure 4.19. The Optical MRI trigger initiates the sine wave from the signal generator, starting with a positive pulse. This sine wave produces a varying magnetic field in the coil which interacts with the main magnetic field, oscillating the lever and hence the phantom.

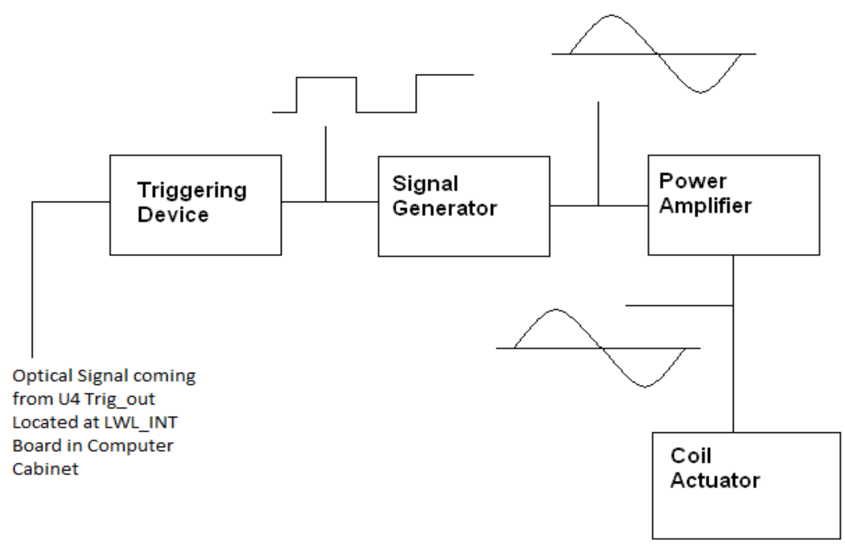

Figure 4.18: Block diagram of Equipment setup.

Figure 4.19: Signal Generator amplifier and trigger box setup.

As mentioned earlier, the 100mA current was used for the 125Hz frequency and 200mA was used with the 250Hz frequency. The current amplitudes were adjusted using the program knob located at front of power amplifier. The magnetic field produced in the coil and the force exerted in the magnet was estimated earlier. For confirmation, it was verified physically that the moving head was vibrating inside the magnet and that the moving head was in good contact with gel phantom.

The phantom was moved to the middle of the magnet, and sand bags were placed around the phantom and actuator to keep them stable during scanning as shown in figure 4.20.

Figure 4.20: View of setup inside magnet.

4.6 Experimental Procedure:

The step by step procedure used to acquire the images required for MRE reconstruction is written below:

- Sequence Parameters selected for scanning were: TR = 120ms, TE = 31.3ms, No of slices = 1, Slice thickness = 5mm, FOV = 20cm X 20cm, base resolution = 256 X 256, average is 1, Coil used was Spine coil and no filters selected.
- MRE parameters: frequency 250 Hz, MEG amplitude 10mT/m, MEG Cycles = 4 and pre-MEG STIM = 2. Mechanical waves were traveling in

RO direction so the data set is acquired with RO MEG ON and other two axes off.

- Option selected in the sequence selection tab to reconstruct both the magnitude and phase Images.
- Power amplifier adjusted so that 200mA current is present in the coil.
- Eight slices were acquired where four slices are with MEG PHASE = Pos and MEG Delay = 0, 45, 90 and 135 simultaneously and next four slices were with MEG PHASE = Neg and MEG Delay = 0, 45, 90 and 135 simultaneously. Table 4.1 shows the combination of MRE parameters used to acquire 8 images for one phantom.

Image Number	**Motion Encoding Gradient**	**MEG PHASE**	**MEG Delay**
1	RO MEG ON	Pos	0
2	RO MEG ON	Neg	0
3	RO MEG ON	Pos	45
4	RO MEG ON	Neg	45
5	RO MEG ON	Pos	90
6	RO MEG ON	Neg	90
7	RO MEG ON	Pos	135
8	RO MEG ON	Neg	135

Table 4.1: Combination of MRE Parameters.

- Phase difference image calculated using the subtraction tool available in MRI System by subtracting the two phase images (Positive and Negative MEG PHASE).
- Elasticity map was reconstructed using the four phase difference images calculated at four phase offsets 0, 45, 90 and 135 using MRE/Wave software [51].
- This same procedure was repeated for 125Hz with 100mA current in the coil.

4.7 Data Acquisition and Reconstruction:

The phase difference images are calculated by subtracting the negative polarity image from the positive polarity image, independently for each phase difference (0, 45, 90 and 135 degrees). The magnitude images are used only for masking the images.

It was indicated in section 3.5.4.3 that the MRE/wave software [51] for elasticity reconstruction developed by Ehman and his group will be used in this thesis. Different types of input data can be loaded in the software, and it is capable of reading in the standard DICOM images collected with MRI. Magnitude images were loaded for masking and four phase difference images were loaded for the elasticity reconstruction. Parameters needed to perform inversion are FOV, MEG frequency, Number of MEG and MEG amplitude. A Gauss Band Pass filter was used to reduce noise.

The image sets acquired at 250Hz and 125Hz were analyzed independently. The results, and in particular the reconstructions of elasticity maps will be presented in the next chapter. Within the MRE/Wave software, the mean and SD were calculated within a region of interest (ROI) for both cylinders within the phantom, and for the background material.

Chapter 5

Results and Discussion

5.1 Image Data and Raw Data:

The magnitude data used for masking is shown in figure 5.1. Phase difference images obtained using an applied 250Hz frequency of oscillation is presented in Figure 5.2.

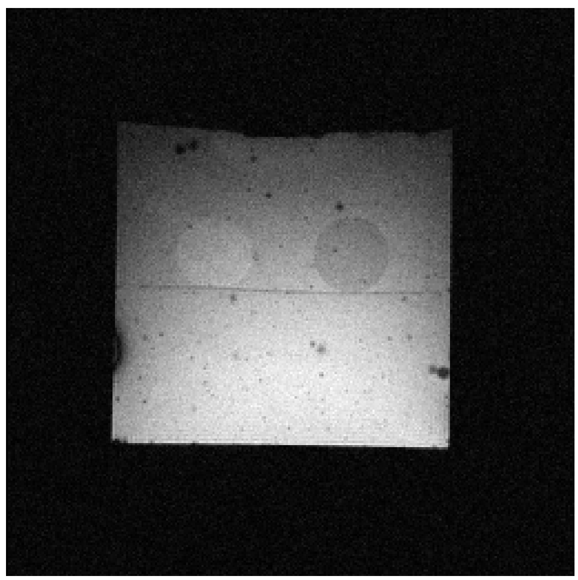

Figure 5.1: Magnitude Image of Phantom.

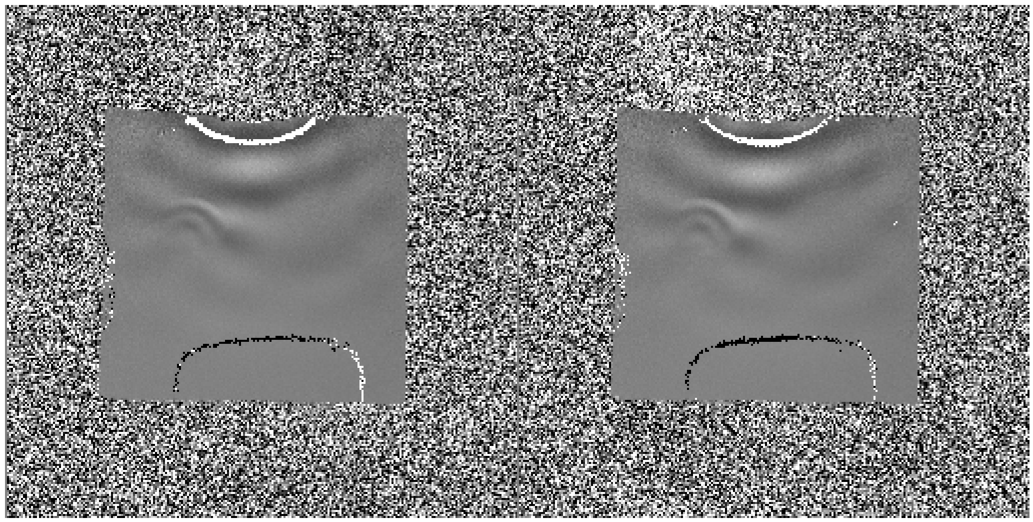

(a) (b)

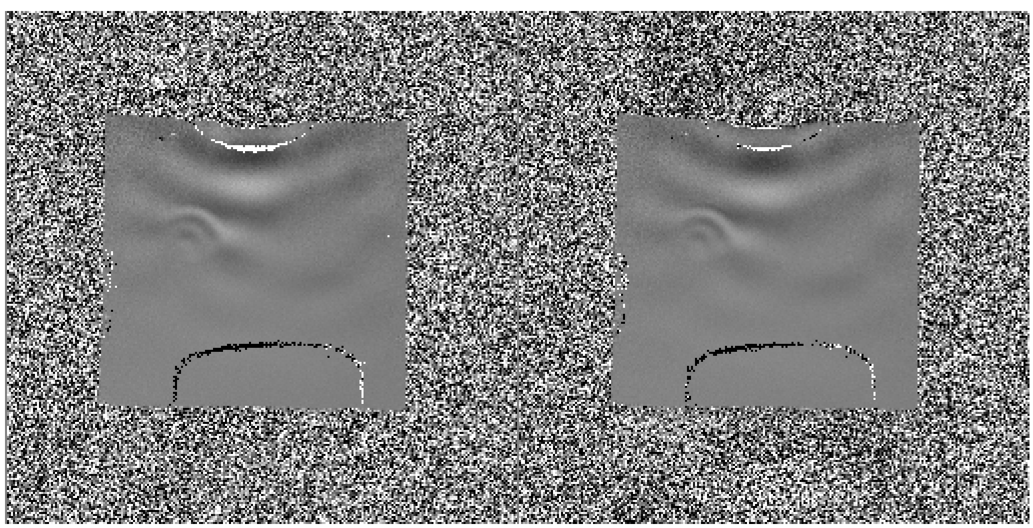

(c) (d)

Figure 5.2: 250 Hz Phase difference Image at 0 MEG Delay (a), 45 MEG Delay (b), 90 MEG Delay (c) and 135 MEG Delay (d).

Note that phase distortions can be observed near the top of the masked image because of the oscillation. A small disturbance can also be observed near the location of the cylinder on the left of the image.

The second data set, acquired with a frequency of 125 Hz and all other parameters and methodology identical, is composed of the four phase difference images shown in figure 5.3.

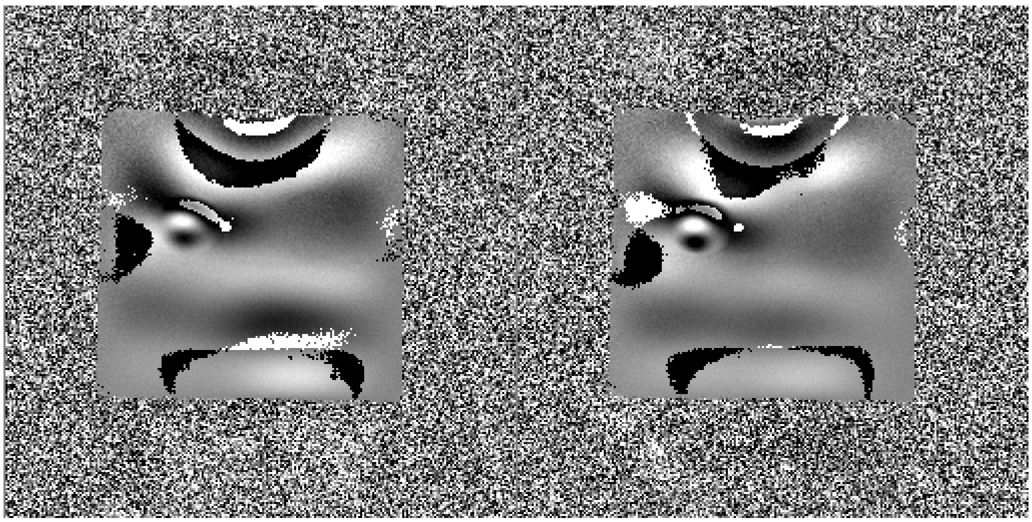

(a) (b)

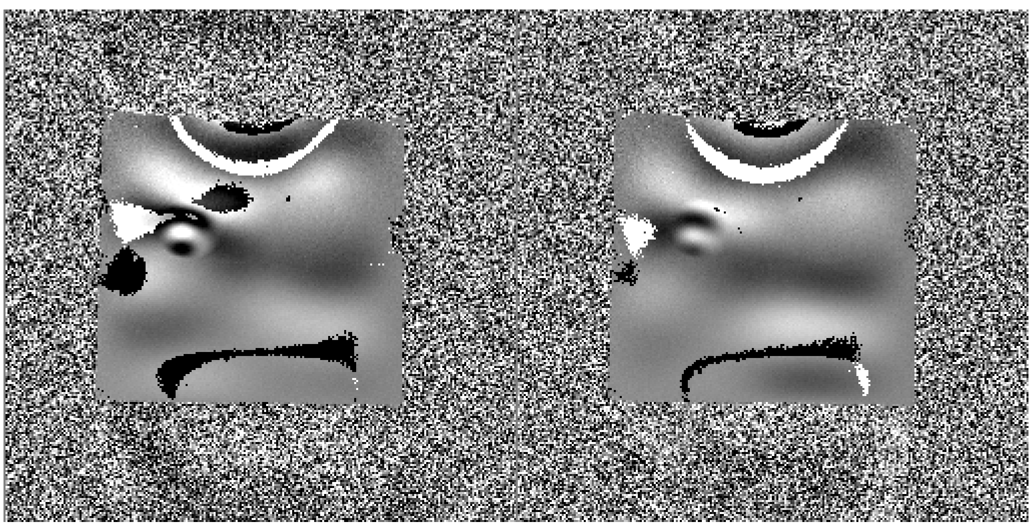

(c) (d)

Figure 5.3: 125 Hz Phase difference Image at 0 MEG Delay (a), 45 MEG Delay (b), 90 MEG Delay (c) and 135 MEG Delay (d).

Note that the wavelength of the phase wrapping appears to be less than the previous case, as expected from the decreased oscillatory frequency. There is still more of an effect visible in the left most cylinder, as compared to the right; however the number of phase wrappings has decreased from the previous case.

5.2 Elasticity reconstruction:

An amplitude displacement map for the 250Hz frequency case is shown in figure 5.4 which shows the particle displacement in microns. In figure 5.5, the interpolated wave propagation is shown. This plot represents the travelling wave in color using actual data points and known data points. Actual points are the displacements calculated from acquired data and known points are the values calculated using input parameters. Figure 5.5 shows that the wavelength of the travelling wave is shorter in the soft gel (left cylinder in figure) and longer in the more rigid gel cylinder (cylinder on right in figure).

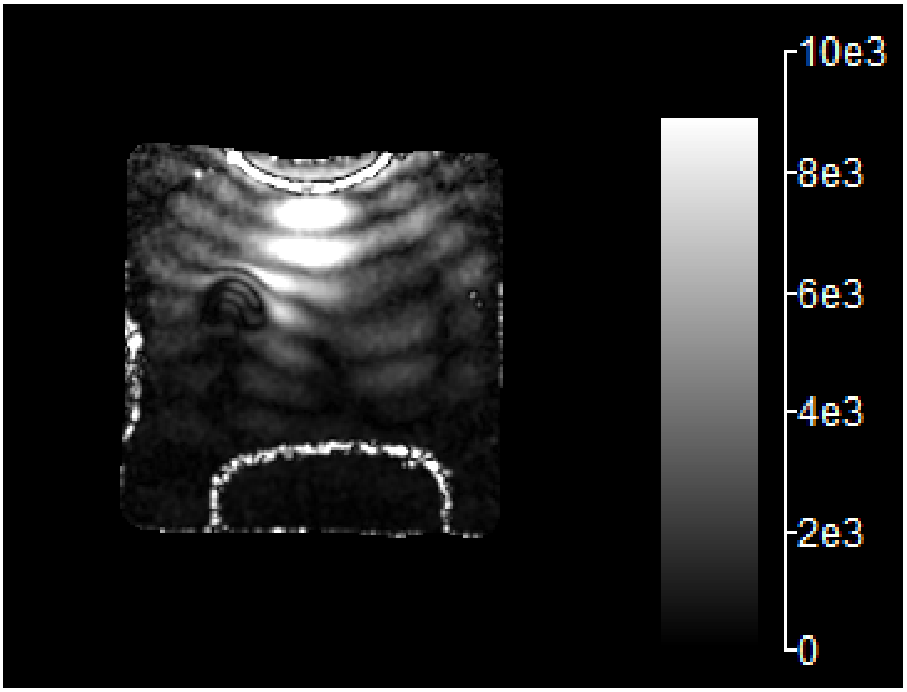

Figure 5.4: Amplitude displacement map at 250 Hz. Vertical scale bar is in μm (micron).

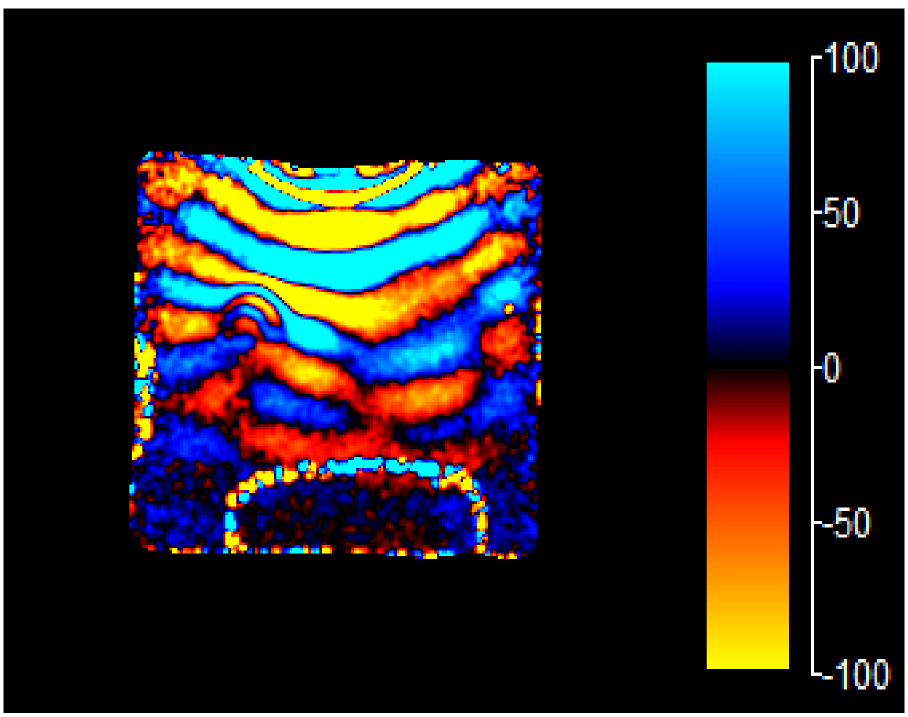

Figure 5.5: Interpolated Wave propagation at 250 Hz. Vertical scale bar is in μm (micron).

The local frequency estimation is shown in figure 5.6. This image similarly indicates that the frequency of vibration is higher in the softer gel. In figure 5.7, the map of the elasticity is given in KPa. Note that the softer gel (left) has a lower elasticity, compared to the harder gel (right) as expected.

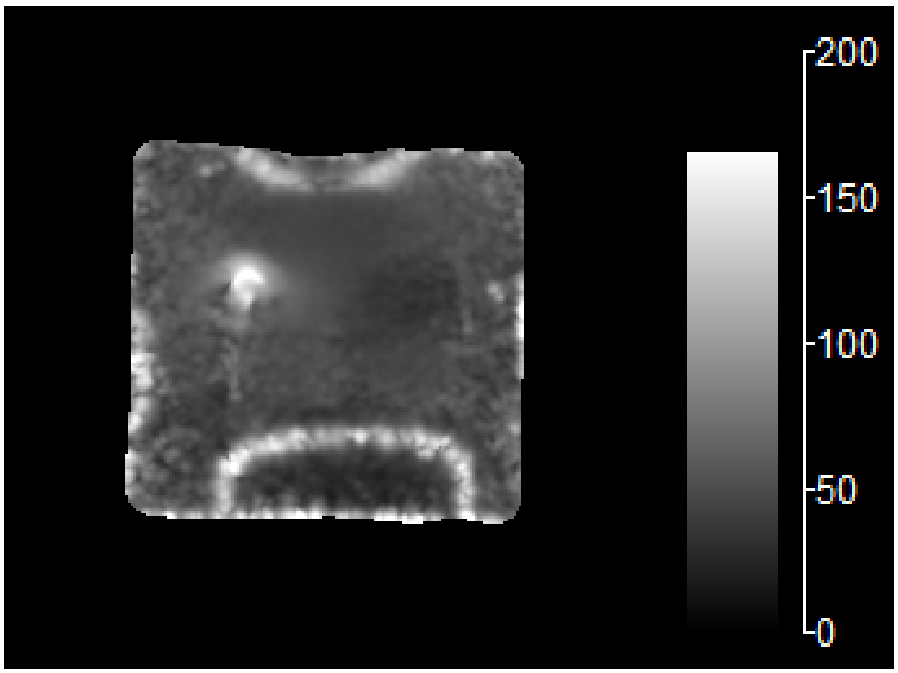

Figure 5.6: Local frequency estimation at 250 Hz. Vertical scale bar is in Waves/FOV.

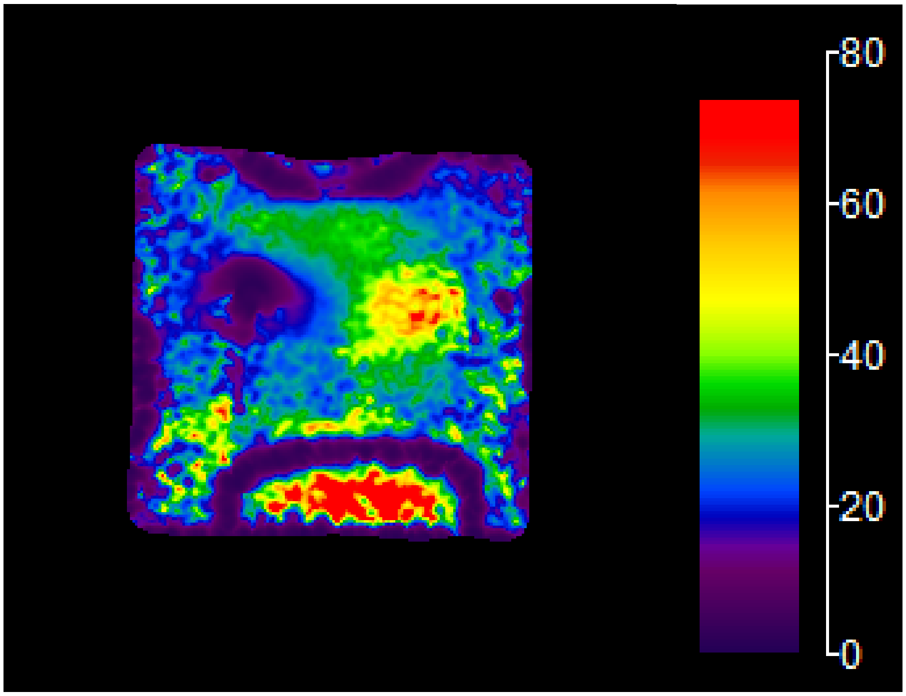

Figure 5.7: Elasticity map at 250 Hz. Vertical scale bar is in kilopascals (KPa).

The second data set acquired at 125Hz, is also reconstructed and results are similarly shown in figure 5.8-5.11. At 125 Hz many more artifacts are observed and the propagating waves are distorted, however the waves do have a larger wavelength because of the lower frequency.

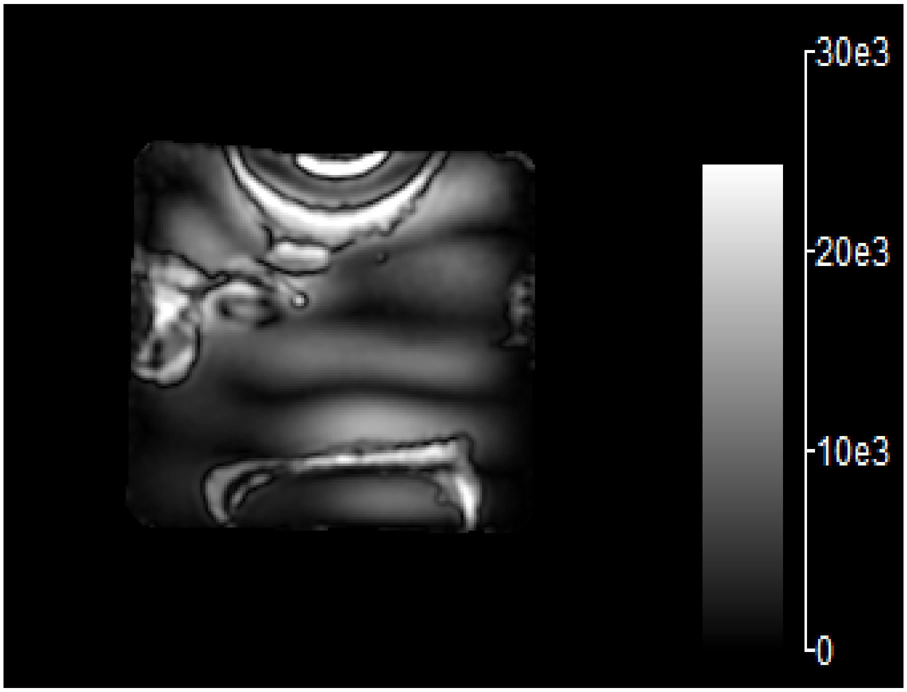

Figure 5.8: Amplitude displacement map at 125 Hz. Vertical scale bar is in μm (micron).

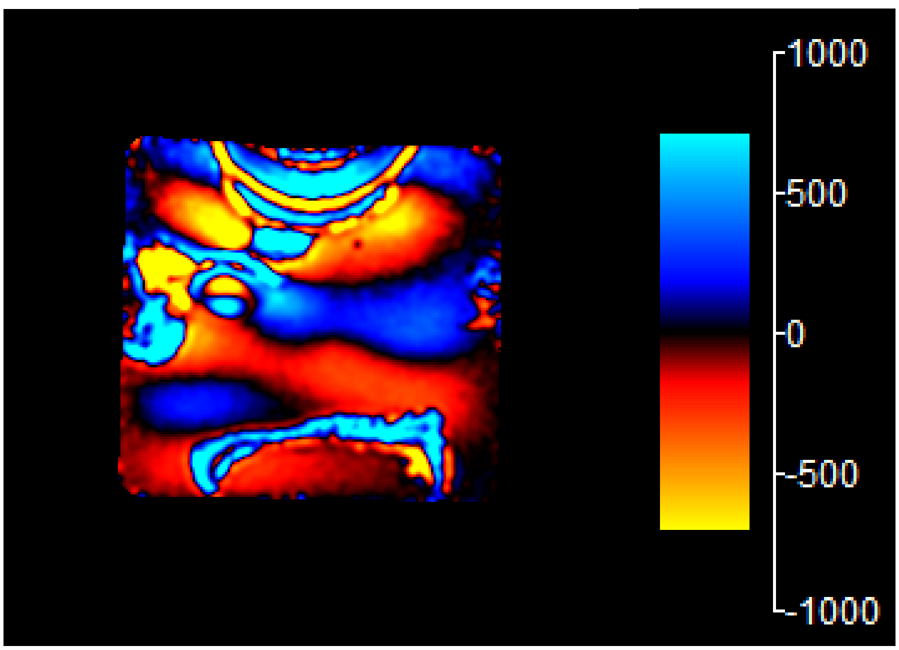

Figure 5.9: Interpolated Wave propagation at 125 Hz. Vertical scale bar is in μm (micron).

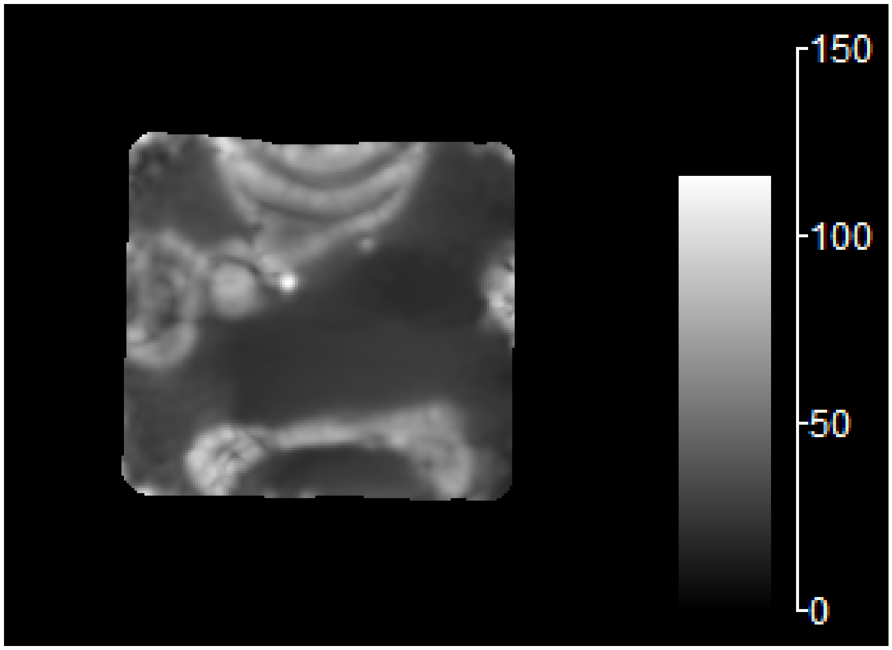

Figure 5.10: Local frequency estimation at 125 Hz. Vertical scale bar is in Waves/FOV.

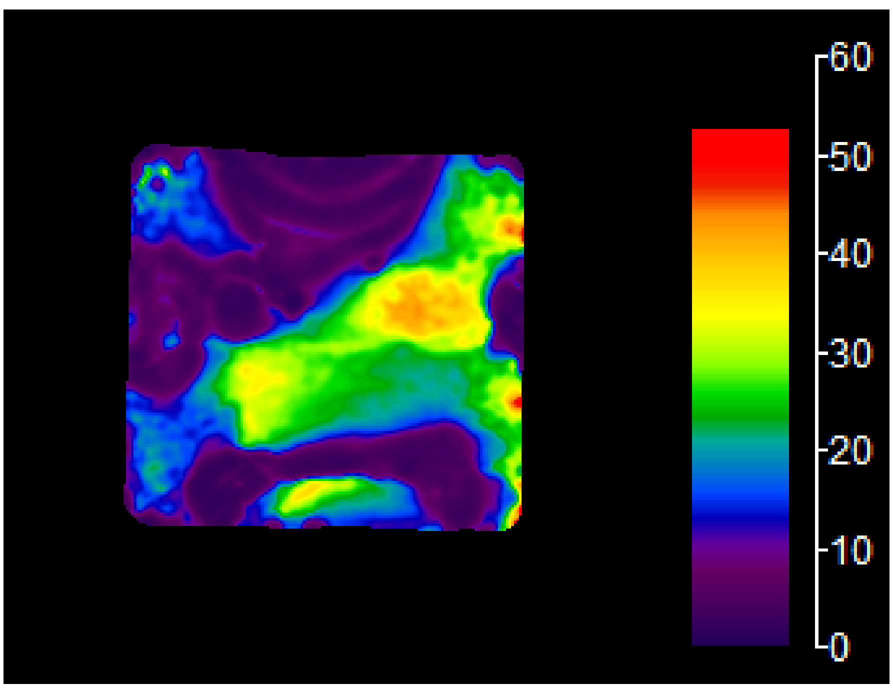

Figure 5.11: Elasticity map at 125 Hz. Vertical scale bar is in kilopascals (KPa).

5.3 Elasticity measurement:

In case of 250Hz, mean elasticity value measured in 1% gel cylinder is 10 kPa and standard deviation (SD) is 6 kPa and the location of 1% gel cylinder is shown by a circle in the elasticity map in figure 5.13. Mean elasticity value measured in 3% gel is 49 kPa and SD is 9 kPa and their location is shown by a circle in the elasticity map in figure 5.14. Value measured in the background which is 2% gel is 28 kPa and SD is 6 kPa. The phantom boundary seems to be less elastic because of air and water on the sides. There is an artifact at the bottom marked with a yellow arrow. This region may indicate trapped water or a less elastic area with a higher elastic area underneath. It could be the result of actuator head pushing the phantom at this point or the result of some problem with gel phantom construction. Also the travelling waves seem to be damped at the bottom part of the phantom as shown in figure 5.5.

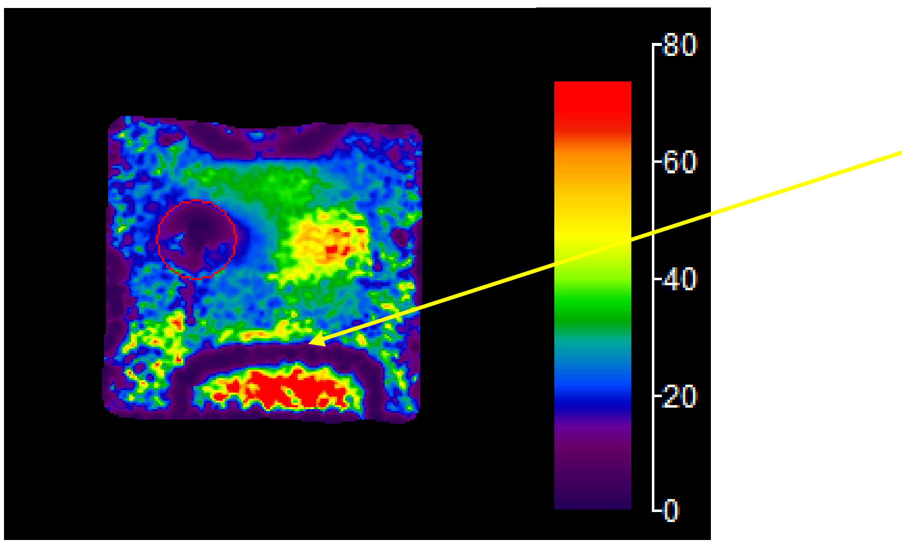

Figure 5.12: Elasticity map at 250 Hz showing the location of 1% gel cylinder. Vertical scale bar is in kilopascals (KPa).

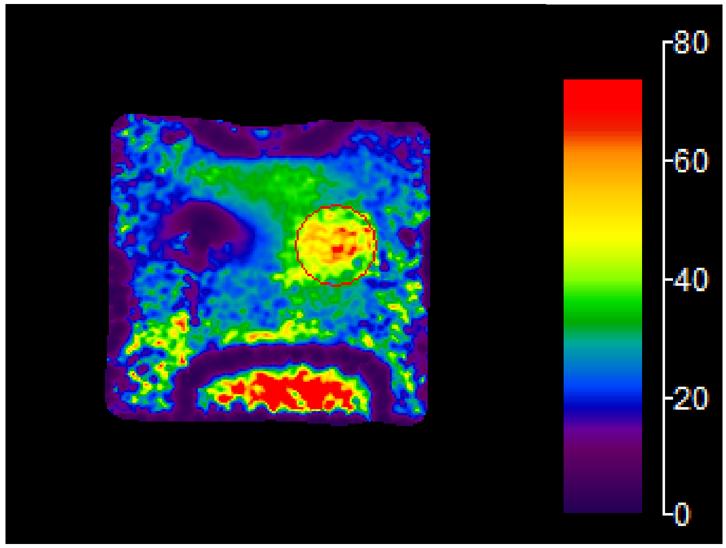

Figure 5.13: Elasticity map at 250 Hz showing the location of 3% gel. Vertical scale bar is in kilopascals (KPa).

In case of 125Hz, the elastogram is more distorted than at 250Hz as shown in figure 5.12. However the elasticity values are still very similar to those measured at 250Hz. At 125Hz, the mean elasticity measured within 1% gel cylinder is 5 kPa and SD is 2 kPa as shown in figure 5.14, and mean elasticity value measured at 3% gel cylinder is 37 kPa and SD 3kPa as shown in figure 5.15. Background which is 2% gel is distorted however mean value measured is 25 kPa and SD is 2 kPa.

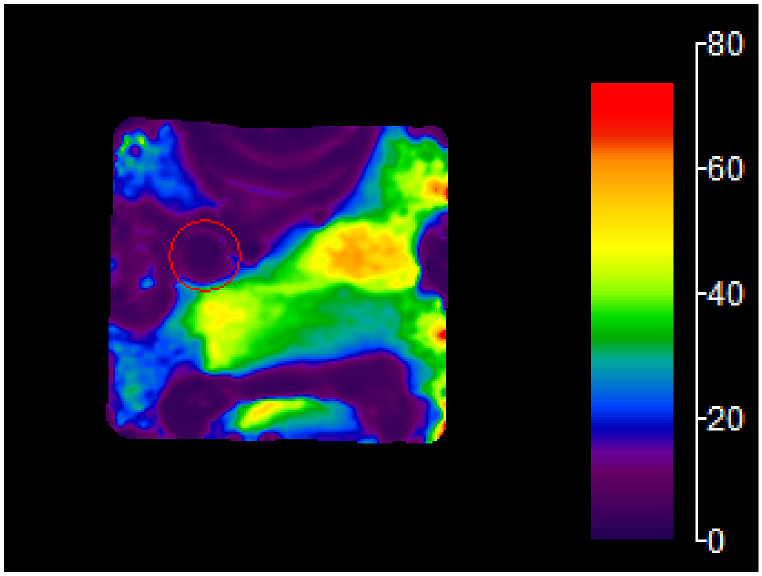

Figure 5.14: Elasticity map at 125 Hz showing the location of 1% gel. Vertical scale bar is in kilopascals (KPa).

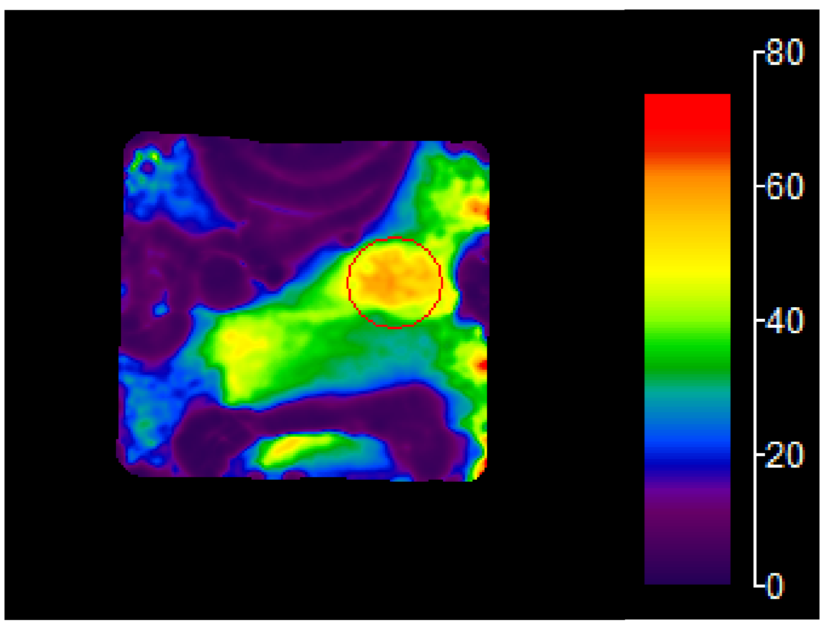

Figure 5.15: Elasticity map at 125 Hz showing the location of 3% gel. Vertical scale bar is in kilopascals (KPa).

Ehman and his group presented a paper in 2003 [107] where MRE is performed on a phantom with a similar type of material at 400 Hz. The stiffness value of the 1% gel was 6KPa, the 2% gel was 22KPa and the 3% gel was 80KPa as mentioned in their paper. The stiffness map of their phantom is reproduced in figure 5.14 showing the values obtained with MRE.

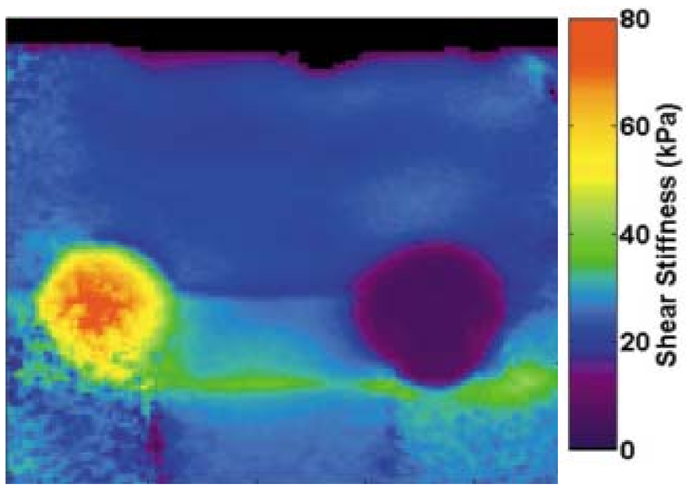

Figure 5.16: Elasticity map of the phantom used by Ehman Group. Phantom has 1% gel cylinder is on right side and 3% gel cylinder is on left with 2% gel in background. Source:[107].

The Ehman study shows that our results are very close to their actual and MRE values measured. However results can be further improved by upgrading different components of the setup, sequence and reconstruction which will be discussed in detail in the next chapter.

MRE reconstruction always suffers from outliers and interfering noise. These are caused by the mechanical actuators or noise caused by interference in MRI which cannot be suppressed in phase difference images. Filters available in reconstruction software are not efficient to suppress these sources of noise and artifacts. Different mathematical techniques were presented in the literature to suppress these noise and artifacts, for example the Level set diffusion for MRE Image Enhancement presented by Nan Li [108].

Also the assumption of local homogeneity in reconstruction creates inaccurate results near region boundaries and places a limit on resolution. In the above analysis four phase difference images were acquired at different phase offsets which were not enough to capture the complete wave period. Increasing the number of phase difference images to eight phase offsets would improve the results.

Chapter 6

Conclusion Challenges and Future Plans

Work presented in the thesis details the method and implementation of MR Elastography, including the design of actuator and developing the gradient echo sequence for MR Elastography.

6.1 Conclusion:

An introduction was given to MRI in chapter 2, and chapter 3 provided a more detailed description of the MRE process. Chapters 4 and 5 explain the actual design, implementation and data collection. Two frequencies 125Hz and 250Hz were used for these experiments. The phantom was constructed from agar gel with cylinders of different concentrations. In case of 250Hz, mean elasticity value measured in 1% gel cylinder is 10 kPa and standard deviation (SD) is 6 kPa. Mean elasticity value measured in 3% gel is 49 kPa and SD is 9 kPa. Mean value measured in the background which is 2% gel is 28 kPa and SD is 6 kPa. The results obtained are comparable to the values calculated in literature [106]. Elasticity map at 250 Hz has less artefacts compare to 125 Hz.

The actuator was made from Plexiglas with a light weight coil design. An electromagnetic coil is used to produce motion because of cost and simplicity. This coil however had a tendency to produce artefacts in the image, but these artefacts are not pronounced within our results. They will however be problematic when more complex geometries will be imaged such as complex phantoms or the human body. Sequence is very stable and no sequence related noise and artefacts has been observed.

6.2 Challenges:

There is an inherent limit to the spatial resolution of the technique. The spatial resolution of MRE can be improved by increasing the frequency, however the high frequency waves will be attenuated more rapidly compared to lower frequency waves. Thus there exists a trade off between spatial resolution and distance from the vibration source [109]. Also the sample size needs to accommodate half a shear wave in the MRE image in order to measure the stiffness. For example sample size of 10 mm needs a wavelength of 20 mm to be properly detected in elastogram. At one fixed frequency, wavelength in stiffer materials is larger compare to soft materials so for that purpose we need higher frequencies to make wavelength smaller in order to detect smaller sample sizes. For that purpose better actuators are needed to induce the high frequency motion with minimal time delay [110].

In this form of gel phantom, air and water exists between the layers of gel which is evident from the magnitude images. Because of this gap, there exist layers that are in poor contact and waves seem to be damped and distorted in the area under this gap.

6.3 Future Work:

Future work should continue in a number of different areas to improve the results. The actuator design can be improved. First, the size of the actuator should be changed for different clinical applications or application specific actuators should be designed. The weight of the coil needs to be reduced to work with higher frequencies. The pivot point needs a different design to minimize the effects of friction. Finally, the actuator head could be made vertically adjustable for better contact with the vibrating area. Also other types of actuators mentioned in section 3.3 can be used especially the one where the long rod is attached with speaker .

The existing MRE sequence should also be reprogrammed to acquire data at eight different phase offsets to capture the motion at eight different time intervals compare to four in one motion cycle, gives more precise picture of wave propagation. Also the image calculation part of the sequence needs modification to accommodate the eight phase difference images generated with one acquisition. Other sequences, such as the simple spin echo would make a valuable comparison to the modified gradient echo, and should be reprogrammed for MRE. This comparison helps us to see if the phase unwrapping artefacts will be reduced in SE because of the 180 degree refocusing pulse.

The phantom construction needs to be improved to avoid gaps and include more complex geometries. Other materials used in our laboratory for various imaging applications such as polyvinyl alcohol cryogel should also be assessed. One interesting application of MRE is to measure the elastic properties of a complex tissue mimicking phantom. The elastic properties of the constituents of a phantom can be measured independently with techniques such as an Instron tester, or through surrogate measures such as indentation. However once the phantom is constructed, it is not possible to non-destructively test the components of the molded phantom. Through MRE measurements however we can compare the elastic properties of PVA gel constituents measured independently in the laboratory to MR elastography measurements of the components built into the completed phantom non-destructively.

For this project, the freely available MRE/Wave software was used. In order to pursue MRE for our own research applications, we would need to invest in the development of our own reconstruction software, that allows us to tailor the software for our own needs and applications.

Bibliography

1. Watkinson JC, Johnston D, Jones N, Coady M, Laws D, Allen S, Hibbert J. *The reliability of palpation in the assessment of tumours*. Clin Otolaryngol Allied Sci. 1990 Oct;15(5):405-9.

2. http://ww2.cancer.org/downloads/STT/CPED2002PWSecured.pdf (Page 25).

3. Barton MB, Harris R, Fletcher SW. *The rational clinical examination. Does this patient have breast cancer? The screening clinical breast examination: should it be done? How?* JAMA. 1999 Oct 6;282(13):1270-80.

4. Sarvazyan A. *Mechanical imaging: a new technology for medical diagnostics*. Int J Med Inform. 1998 Apr;49(2):195-216.

5. Fung, Y. C. (Yuan-cheng), *Biomechanics : mechanical properties of living tissues*. 2nd ed. Published: New York : Springer-Verlag, 1993.

6. Iatridis JC, Kumar S, Foster RJ, Weidenbaum M, Mow VC. *Shear mechanical properties of human lumbar annulus fibrosus*. J Orthop Res. 1999 Sep;17(5):732-7.

7. Thesis : *Magnetic Resonance Elastography at 3 Tesla: Implementation, Validation and Application to a degenerative Disc Model* by Timothy Christian Dunn. 1995.

8. Meng Yin, PhD, Jun Chen, PhD, Kevin J. Glaser, PhD, Jayant A. Talwalkar, MD, and Richard L. Ehman, MD. *Abdominal Magnetic Resonance Elastography.* Top Magn Reson Imaging. 2009 Apr; 20(2):79-87.

9. Talwalkar JA, Yin M, Venkatesh S, Rossman PJ, Grimm RC, Manduca A, Romano A, Kamath PS, Ehman RL. *Feasibility of in vivo MR Elastographic splenic stiffness measurements in the assessment of portal hypertension*. AJR Am J Roentgenol. 2009 Jul; 193(1):122-7.

10. Patrick Asbach, Dieter Klatt, Uwe Hamhaber, Jurgen Braun, Rajan Somasundaram, Bernd Hamm, and Ingolf Sack. *Assessment of Liver Viscoelasticity Using Multifrequency MR Elastography*. Magn Reson Med. 2008 Aug; 60(2):373-9.

11. Huwart L, Sempoux C, Vicaut E, Salameh N, Annet L, Danse E, Peeters F, ter Beek LC, Rahier J, Sinkus R, Horsmans Y, Van Beers BE. *Magnetic resonance elastography for the noninvasive staging of liver fibrosis*. Gastroenterology. 2008 Jul; 135(1):32-40. Epub 2008 Apr 4.

12. Scott A. Kruse, Gregory H. Rose, Kevin J. Glaser, Armando Manduca, Joel P. Felmlee, Clifford R. Jack Jr., and Richard L. Ehman. *Magnetic resonance elastography of the brain.* Neuroimage. 2008 Jan 1; 39(1):231-7. Epub 2007 Aug 29.

13. Ingolf Sack, Bernd Beierbach, Uwe Hamhaber, Dieter Klatt and Jurgen Braun. *Non-invasive measurement of brain viscoelasticity using magnetic resonance elastography*. NMR Biomed. 2008 Mar; 21(3):265-71.

14. Ingolf Sack,Bernd Beierbach, Jens Wuerfel, Dieter Klatt, Uwe Hamhaber, Sebastian Papazoglou, Peter Martus, Jürgen Braun.*The impact of aging and gender on brain viscoelasticity.* Neuroimage. 2009 Jul 1; 46(3):652-7. Epub 2009 Mar 10.

15. McKnight AL, Kugel JL, Rossman PJ, Manduca A, Hartmann LC, Ehman RL. *MR Elastography of breast cancer: preliminary results*. AJR Am J Roentgenol. 2002 Jun; 178(6):1411-7.

16. Tanja Xydeas, MD, Katja Siegmann, MD, Ralph Sinkus, PhD, Ute Krainick-Strobel, MD, Stephan Miller, MD, and C. D. Claussen, MD. *Magnetic Resonance Elastography of the Breast Correlation of Signal Intensity Data with Viscoelastic Properties*. Invest Radiol. 2005 Jul; 40(7):412-20.

17. Siegmann KC, Xydeas T, Sinkus R, Kraemer B, Vogel U, Claussen CD. *Diagnostic value of MR Elastography in addition to contrast-enhanced MR imaging of the breast-initial clinical results*. Eur Radiol. 2010 Feb; 20(2):318-25. Epub 2009 Sep 1.

18. Thomas Elgeti, MD, Jens Rump, MS, Uwe Hamhaber, PhD, Sebastian Papazoglou, MS,Bernd Hamm, MD, Ju¨rgen Braun, PhD, and Ingolf Sack, PhD. *Cardiac Magnetic Resonance Elastography Initial Results*. Invest Radiol. 2008 Nov; 43(11):762-72.

19. Orlando Lopez, BS, Kimberly K. Amrami, MD, Armando Manduca, PhD, Phillip J. Rossman, MS, and Richard L. Ehman, MD. *Developments in Dynamic MR Elastography for In Vitro Biomechanical Assessment of Hyaline Cartilage under High-Frequency Cyclical Shear.* J Magn Reson Imaging. 2007 Feb; 25(2):310-20.

20. B.C.Goss, K.P.McGee, E.C. Ehman, A. Manduca, and R.L. *Ehman. Magnetic Resonance Elastography of the Lung: Technical Feasibility*. Magn Reson Med. 2006 Nov; 56(5):1060-6.

21. Stacie I. Ringleb, PhD, Sabine F. Bensamoun, PhD, Qingshan Chen, MS, Armando Manduca, PhD, Kai-Nan an, PhD, and Richard L. Ehman, MD. *Applications of Magnetic Resonance Elastography to Healthy and Pathologic Skeletal Muscle*. J Magn Reson Imaging. 2007 Feb; 25(2):301-9.

22. Qingshan Chen, Jeffrey Basford, Kai-Nan An. *Ability of magnetic resonance elastography to assess taut bands*. Clin Biomech (Bristol, Avon). 2008 Jun; 23(5):623-9. Epub 2008 Feb 21.

23. Kemper J, Sinkus R, Lorenzen J, Nolte-Ernsting C, Stork A, Adam G. *MR Elastography of the prostate: initial in-vivo application*. Rofo. 2004 Aug; 176(8):1094-9.

24. Mark M. Bahn, MD, PhD, Michael D. Brennan, MD, Rebecca S. Bahn, MD, Diana S. Dean, MD, Jennifer L. Kugel, MS, and Richard L. Ehman, MD. *Development and Application of Magnetic Resonance Elastography of the Normal and Pathological Thyroid Gland in Vivo*. J Magn Reson Imaging. 2009 Nov; 30(5):1151-4.

25. John B. Weaver, Marvin Doyley, Yvonne Cheung, Francis Kennedy Ernest L. Madsen, Elijah E.W. Van Houten, and Keith Paulsen. *Imaging the shear modulus of the heel fat pads*. Clin Biomech (Bristol, Avon). 2005 Mar; 20(3):312-9.

26. Krouskop TA, Dougherty DR, Vinson FS, "*A pulsed Doppler ultrasonic system for making noninvasive measurements of the mechanical properties of soft tissue*," J Rehabil Res Dev, Vol 24(2):1-8, 1987.

27. L. Gao, K. Parker, S. Alam, D. Rubens, and R. Lerner, "*Theory and Application of Sonoelasticity Imaging*," International journal of Imaging Systems and Technology, vol. 8, pp. 104-109, 1997.

28. A. R. Skovoroda, S. Y. Emelianov, and M. O'Donnell, Fellow, "*Tissue Elasticity Reconstruction Based on Ultrasonic Displacement and Strain Images*," IEEE Transactions on Ultrasonics, Ferroelectrics, and Frequency Control. Vol. 42, no. 4, pp. 747-765. July 1995.

29. Parker KJ, Fu D, Graceswki SM, Yeung F, Levinson SF, "*Vibration sonoelastography and the detectability of lesions*," Ultrasound Med Biol, 1998 Nov;24(9):1437-47.

30. Moran PR, "A *flow velocity zeugmatographic interlace for NMR imaging in humans*," Magn Reson Imaging. 1982; 1(4):197-203.

31. Moran PR, Moran RA, Karstaedt N. *Verification and evaluation of internal flow and motion. True magnetic resonance imaging by the phase gradient modulation method*. Radiology. 1985 Feb; 154(2):433-41.

32. Dijk P Van. *Direct cardiac NMR imaging of heart wall and blood flow velocity*. J Comput Assist Tomogr. 1984 Jun; 8(3):429-36.

33. Lewa CJ, de Certaines JD. *MR imaging of viscoelastic properties*. J Magn Reson Imaging. 1995 Mar-Apr; 5(2):242-4.

34. Lewa CJ, De Certaines JD. *Viscoelastic property detection by elastic displacement NMR measurements*. J Magn Reson Imaging. 1996 Jul-Aug; 6(4):652-6.

35. Muthupillai R, Lomas DJ, Rossman PJ, Greenleaf JF, Manduca A, Ehman RL. *Magnetic resonance elastography by direct visualization of propagating acoustic strain waves*. Science. 1995 Sep 29; 269(5232):1854-7.

36. J. B. Fowlkes, S. Y. Emelianov, J. G. Pipe, A. R. Skovoroda, P. L. Carson, R. S. Adler, and A. P. Sarvazyan. *Magnetic-resonance imaging techniques for detection of elasticity variation Med*. Phys. 22 1771 (1995).

37. Plewes DB, Betty I, Urchuk SN, Soutar I. *Visualizing tissue compliance with MR imaging. J Magn Reson Imaging*. 1995 Nov-Dec; 5(6):733-8.

38. Muthupillai R, Rossman PJ, Lomas DJ, Greenleaf JF, Riederer SJ, Ehman RL. *Magnetic resonance imaging of transverse acoustic strain waves*. Magn Reson Med. 1996 Aug; 36(2):266-74.

39. Samani A, Bishop J, Luginbuhl C, Plewes DB,"*Measuring the elastic modulus of ex vivo small tissue samples*," Phys Med Biol, 21; 48(14):2183-98, 2003.

40. Manduca, A. Muthupillai, R. Rossman, P.J. Greenleaf, J.F. Ehman, R.L. *Local wavelength estimation for magnetic resonance elastography*. Image Processing, Vol.3, pp. 527-530., 1996.

41. Kruse SA, Smith JA, Lawrence AJ, Dresner MA, Manduca A, Greenleaf JF, Ehman RL. *Tissue characterization using magnetic resonance elastography: preliminary results*. Phys Med Biol. 2000 Jun;45(6):1579-90.

42. Manduca A, Oliphant TE, Dresner MA, Mahowald JL, Kruse SA, Amromin E, Felmlee JP, Greenleaf JF, Ehman RL. *Magnetic resonance elastography: non-invasive mapping of tissue elasticity*. Med Image Anal. 2001 Dec;5(4):237-54.

43. Jennifer Oudry, PhD, Jun Chen, PhD, Kevin J. Glaser, PhD, Véronique Miette, PhD, Laurent Sandrin, PhD, Richard L. Ehman, MD. *Cross-validation of magnetic resonance elastography and ultrasound-based transient elastography: A preliminary phantom study*. JOURNAL OF MAGNETIC RESONANCE IMAGING 30:1145–1150 (2009).

44. Dutt V, Kinnick RR, Muthupillai R, Oliphant TE, Ehman RL, Greenleaf JF. *Acoustic shear-wave imaging using echo ultrasound compared to magnetic resonance elastography*. Ultrasound Med Biol. 2000 Mar; 26(3):397-403.

45. Lerner RM, Huang SR, Parker KJ. *"Sonoelasticity" images derived from ultrasound signals in mechanically vibrated tissues*. Ultrasound Med Biol. 1990; 16(3):231-9.

46. Knutsson, H. Westin, C.-F. Granlund, G. *Local multiscale frequency and bandwidth estimation*. Image Processing, Vol.1, pp. 36-40., 1994.

47. Oliphant, T.E. Mahowald, J.L. Ehman, R.L. Greenleaf, J.F. *Complex-valued quantitative stiffness estimation using dynamic displacement measurements and local inversion of conservation of momentum*. 10.1109/ULTSYM.1999.849310.

48. Oliphant TE, Manduca A, Ehman RL, Greenleaf JF. *Complex-valued stiffness reconstruction for magnetic resonance elastography by algebraic inversion of the differential equation*. Magn Reson Med. 2001 Feb; 45(2):299-310.

49. Van Houten EE, Paulsen KD, Miga MI, Kennedy FE, Weaver JB. *An overlapping subzone technique for MR-based elastic property reconstruction*. Magn Reson Med. 1999 Oct; 42 (4):779-86.

50. Van Houten EE, Miga MI, Weaver JB, Kennedy FE, Paulsen KD. *Three-dimensional subzone-based reconstruction algorithm for MR Elastography*. Magn Reson Med. 2001 May; 45(5):827-37.

51. Reconstruction software http://mayoresearch.mayo.edu/ehman_lab/mrw-wave.cfm.

52. Manduca A, Lake DS, Kruse SA, Ehman RL. *Spatio-temporal directional filtering for improved inversion of MR elastography images*. Med Image Anal. 2003 Dec;7(4):465-73.

53. Dr R Ehman Website http://mayoresearch.mayo.edu/ehman_lab/mre.cfm

54. Dr I sack Website http://www.elastography.de/seiten/research.htm.

55. Takenori Oida, Akira Amano and Tetsuya Matsuda. *Magnetic Resonance Elastography: in vivo Measurements of Elasticity for Human Tissue*. Proceedings of the 12th International Conference on Informatics Research for Development of Knowledge Society Infrastructure (ICKS'04) 0-7695-2150-9/04, 2004 IEEE.

56. Dunn T, Majumdar S. *Comparison of Motion Encoding Waveforms for Magnetic Resonance Elastography at 3T*. Conf Proc IEEE Eng Med Biol Soc. 2005;7:7405-8.

57. Dominik Weishaupt, Victor D. Kochli, and Borut Marincek. *How does MRI work? An introduction to the Physics and Function of Magnetic Resonance Imaging.* Berlin; New York: Springer, 2003.

58. Mark A. Brown, PH.D, Richard C. SEMELKA, M.D. *MRI Basic Principles and Applications*. Hoboken N.J.: Wiley-Liss, 2003.

59. Dwight G. Nishimura. *Principles of Magnetic Resonance Imaging*. 1996

60. Donald G. Mitchell, M.D. and Mark S. Cohen, Ph.D. *MRI Principles*. Saunders 2004.

61. Wilson LS, Robinson DE, Dadd MJ. *Elastography-the movement begins*. Phys Med Biol. 2000 Jun;45(6):1409-21.

62. Sarvazyan AP, Rudenko OV, Swanson SD, Fowlkes JB, Emelianov SY. *Shear wave elasticity imaging: a new ultrasonic technology of medical diagnostics*. Ultrasound Med Biol. 1998 Nov;24(9):1419-35.

63. Gao L.; Parker K.J.; Lerner R.M.; Levinson S.F. *Imaging of the elastic properties of tissue-a review*. Ultrasound in Medicine and Biology, Volume 22, Number 8, 1996 , pp. 959-977(19).

64. Muthupillai R., D.J. Lomas, P.J. Rossman, J.F. Greenleaf, A. Manduca, S.J. Riederer and R. L. Ehman. *Low Frequency Acoustic shear wave imaging in Tissue-like media using Magnetic Resonance*. 0-7803-2940-6/95,1995 IEEE.

65. Burlew MM, Madsen EL, Zagzebski JA, Banjavic RA, Sum SW. *A new ultrasound tissue-equivalent material*. Radiology. 1980 Feb;134(2):517-20.

66. Tse ZT, Janssen H, Hamed A, Ristic M, Young I, Lamperth M. *Magnetic resonance elastography hardware design: a survey.* Proc Inst Mech Eng H. 2009 May; 223(4):497-514.

67. Talwalkar, J. A., Yin, M., Fidler, J. L., Sanderson, S.O., Kamath, P. S., and Ehman, R. L. *Magnetic resonance imaging of hepatic fibrosis: emerging clinical applications*. Hepatology, 2008, 47, 332–342.

68. Lewa, C. J., Roth, M., Nicol, L., Franconi, J. M., and de Certaines, J. D. *A new fast and unsynchronized method for MRI of viscoelastic properties of soft tissues*. J. Magn. Resonance Imaging, 2000, 12, 784–789.

69. Bishop, J., Samani, A., Sciarretta, J., and Plewes,D. B. *Two-dimensional MR elastography with linear inversion reconstruction: methodology and noise analysis*. Physics Medicine Biology, 2000, 45,2081–2091.

70. Plewes, D. B., Bishop, J., Samani, A., and Sciarretta, J. *Visualization and quantification of breast cancer biomechanical properties with magnetic resonance elastography*. Physics Medicine Biology, 2000, 45, 1591–1610.

71. Braun, J., Braun, K., and Sack, I. *Electromagnetic actuator for generating variably oriented shear waves in MR elastography*. Magn. Resonance Medicine, 2003, 50, 220–222.

72. L. Q. Yao, J. G. Zhang, L. Lu and M. O. Laib. *Nonlinear static characteristics of piezoelectric bending actuators under strong applied electric field*. doi:10.1016/j.sna.2004.04.037.

73. Doyley, M. M., Weaver, J. B., Van Houten, E. W.,Kennedy, F. E., and Paulsen, K. D. *Thresholds for detecting and characterizing focal lesions using steady-state MR elastography*. Med. Physics, 2003,30, 495–504.

74. Uffmann, K. *Design of an MR-compatible piezoelectric actuator for MR elastography*. Concepts in Magn. Resonance, 2002, 15, 239–254.

75. Chan, Q. C., Li, G., Ehman, R. L., Grimm, R. C., Li, R., and Yang, E. S. *Needle shear wave driver for magnetic resonance elastography*. Magn. Resonance Medicine, 2006, 55, 1175–1179.

76. Piezo systems. http://www.piezo.com/prodexm8dqm.html

77. Souchon R, Salomir R, Beuf O, Milot L, Grenier D, Lyonnet D, Chapelon JY, Rouvière O. *Transient MR elastography (t-MRE) using ultrasound radiation force: theory, safety, and initial experiments in vitro*. Inserm, U556, Lyon, France. Remi.Souchon@inserm.fr

78. Zheng Y, Chan QC, Yang ES. *Magnetic resonance elastography with twin drivers for high homogeneity and sensitivity*. Conf Proc IEEE Eng Med Biol Soc. 2006; 1:1916-9.

79. Yogesh K. Mariappan, Rossman PJ, Glaser KJ, Manduca A, Ehman RL. *Magnetic resonance elastography with a phased-array acoustic driver system*. Magn Reson Med. 2009 Mar; 61(3):678-85.

80. Yin M, Rouvière O, Glaser KJ, Ehman RL. Diff*raction-biased shear wave fields generated with longitudinal magnetic resonance elastography drivers*. Magn Reson Imag. 26(6):770-80, Jul. 2008.

81. *Handbook of MRI pulse sequences*, M. A. Bernstein, K. F. King and X. J. Zhou. Elsevier Academic Press, 2004, ISBN: 0-12-092861-2.

82. Hamhaber U, Grieshaber FA, Nagel JH, Klose U. *Comparison of quantitative shear wave MR-elastography with mechanical compression tests*. Magn Reson Med. 2003 Jan;49(1):71-7.

83. Maderwald S, Uffmann K, Galbán CJ, de Greiff A, Ladd ME. *Accelerating MR elastography: a multiecho phase-contrast gradient-echo sequence*. J Magn Reson Imaging. 2006 May;23(5):774-80.

84. Weaver JB, Van Houten EE, Miga MI, Kennedy FE, Paulsen KD. *Magnetic resonance elastography using 3D gradient echo measurements of steady-state motion*. Med Phys. 2001 Aug;28(8):1620-8.

85. Antonio Baldi. *Two-Dimensional Phase Unwrapping by Quad-Tree Decomposition*. Applied Optics, Vol. 40, Issue 8, pp. 1187-1194 (2001).

86. Kai Man Hung and T. Yamada. *Phase unwrapping by regions using least-squares approach*. Opt. Eng. / Volume 37 / Issue 11. Opt. Eng., Vol. 37, 2965 (1998); doi:10.1117/1.601884.

87. Miguel Arevallilo Herráez, David R. Burton, Michael J. Lalor, and Munther A. Gdeisat. *Fast two-dimensional phase-unwrapping algorithm based on sorting by reliability following a noncontinuous path*. Applied Optics, Vol. 41, Issue 35, pp. 7437-7444 (2002).

88. N. H. Ching, D. Rosenfeld, and M. Braun, *"Two-dimensional phase unwrapping using a minimum spanning tree algorithm,"* IEEE Trans. Image Process. 1, 355–365 ~1992!.

89. J. M. Huntley, *"Noise immune phase unwrapping algorithm,"* Appl. Opt. 28, 3268–3270 ~1989.

90. Kazuyoshi Itoh. *Analysis of the phase unwrapping algorithm*. Applied Optics, Vol. 21, Issue 14, pp. 2470-2470 (1982).

91. D.C Ghiglia and M.D. Pritt, *Two-Dimensional Phase Unwrapping: Theory, Algorithms, and Software*. New York: John Wiley & Sons, 1998.

92. Thomas J. Flynn. *Phase Unwrapping Using Discontinuity Optimization*. Sandia National Laboratories. P.O. Box 5800, Mail Stop 1207 Albuquerque, NM 87185-1207, USA.

93. Adel S. Saada, Ing., E.C.P., Ph.D. *Elasticity: Theory and Applications.*

94. Kallel F, Bertrand M. *Tissue elasticity reconstruction using linear perturbation method*. IEEE Trans Med Imaging. 1996;15(3):299-313.

95. Auld, B. A. (Bertram Alexander).*Acoustic fields and waves in solids* .Published: New York: Wiley, [1973].

96. A. M. MANIATTY and E. PARK. *FINITE ELEMENT APPROACH TO INVERSE PROBLEMS IN DYNAMIC ELASTOGRAPHY.* Proceedings of the 5th International Conference on Inverse Problems in Engineering: Theory and Practice, Cambridge, UK, 11-15th, July 2005

97. *MR-Elastography* Ralph Sinkus, PhD (http://afni.nimh.nih.gov/sscc/staff/rwcox/ISMRM_2006/Syllabus%202006%20-%203340/files/A_12.pdf).

98. Catheline S, Gennisson JL, Delon G, Fink M, Sinkus R, Abouelkaram S, Culioli J. *Measuring of viscoelastic properties of homogeneous soft solid using transient elastography: an inverse problem approach.* Laboratoire Ondes et Acoustique, ESPCI, Université Paris VII, U.M.R. C.N.R.S. 7587, 10 rue Vauquelin, 75231 Paris 05, France. stefan.catheline@espci.fr

99. Stefan Catheline, Franc¸ois Wu, and Mathias Fink. *A solution to diffraction biases in sonoelasticity: The acoustic impulse technique.* Laboratoire Ondes et Acoustique, E.S.P.C.I., Universite´ Paris VII, U.M.R. 7587 C.N.R.S 1503,10 rue Vauquelin 75231 Paris cedex 05, France

100. Romano AJ, Shirron JJ, Bucaro JA. *On the noninvasive determination of material parameters from a knowledge of elastic displacements theory and numerical simulation*. IEEE Trans Ultrason Ferroelectr Freq Control. 1998;45(3):751-9.

101. Manduca, A., Muthupillai, R., Rossman, P.J., Greenleaf, J.F. and Ehman, R.L., 1996. *Image processing for magnetic resonance elastography*. SPIE Med Img 2710, 616-623.

102. http://www.medical.siemens.com/webapp/wcs/stores/servlet/ProductDisplay~q_catalogId~e_1~a_catTree~e_100010,1007660,12754,14330~a_langId~e_1~a_productId~e_181442~a_storeId~e_10001~a_view~e_38.htm

103. http://www.belden.com/techdatas/metric/8079.pdf

104. http://hyperphysics.phy-astr.gsu.edu/hbase/magnetic/solenoid.html

105. http://hyperphysics.phyastr.gsu.edu/hbase/magnetic/magmom.html

106. http://www.emdchemicals.com/food-analytics/agar-agar-purified/EMD_CHEM-1.01614/p_SFWb.s1L73kAAAEWGcofVhTm

107. Glaser KJ, Felmlee JP, Manduca A, Ehman RL . *Shear stiffness estimation using intravoxel phase dispersion in magnetic resonance elastography.*. Department of Radiology, Mayo Foundation, Rochester, Minnesota 55905, USA. Magn Reson Med. 2003 Dec;50(6):1256-65

108. Bing Nan Li, Chee Kong Chui, Sim Heng Ong, Stephen Chang and Etsuko Kobayashi. *Level Set Diffusion for MRE Image Enhancement.* Medical Imaging and Augmented Reality Lecture Notes in Computer Science, 2010, Volume 6326/2010, 305-313, DOI: 10.1007/978-3-642-15699-1_32 .

109. Mariappan YK, Glaser KJ, Ehman RL. *Magnetic resonance elastography: a review*. Department of Radiology, Mayo Clinic, 200 First Street SW, Rochester, MN 55905, USA. mariappan.yogesh@mayo.edu.

110. Othman SF, Curtis ET, Plautz SA, Pannier AK, Butler SD, Xu H. *MR elastography monitoring of tissue-engineered constructs*. Department of Biological Systems Engineering, University of Nebraska-Lincoln, Lincoln, NE, USA. sothman2@unl.edu.